UNIVERSITAT DE BARCELONA

Seismic Attenuation Analysis using Lg waves and Ambient Noise Recordings: Application to the Iberian Peninsula and Morocco

Raquel Noriega Salmón

CSIC ICTJA
INSTITUTE OF EARTH SCIENCES JAUME ALMERA (ICTJA)

UNIVERSITAT DE BARCELONA

Seismic Attenuation Analysis using Lg waves and Ambient Noise Recordings: Application to the Iberian Peninsula and Morocco

A thesis submitted in conformity with the requirements for the degree of Doctor of Earth Sciences

Department of Geodynamics and Geophysics
University of Barcelona

presented by

Raquel Noriega Salmón

July 2016

Seismic Attenuation Analysis using Lg waves and Ambient Noise Recordings: Application to the Iberian Peninsula and Morocco

A dissertation submitted to

Doctorate Program in Earth Sciences

University of Barcelona

for the degree of

Doctor of Earth Sciences

presented by

Raquel Noriega Salmón

Supervisors

Dr. María José Jurado Rodríguez
Institute of Earth Sciences Jaume Almera
Spanish National Research Council (CSIC)

Dr. Antonio Villaseñor Hidalgo
Institute of Earth Sciences Jaume Almera
Spanish National Research Council (CSIC)

Tutor

Dr. Jaume Pous Fàbregas
Department of Geodynamics and Geophysics (UB)

CONTENTS

ACKNOWLEDGEMENTS

Me gustaría que estas líneas sirvieran para expresar mi más profundo y sincero agradecimiento a todas aquellas personas que de algún modo me han ayudado durante el desarrollo de este trabajo de investigación.

En primer lugar, agradezco al Dr. Antonio Villaseñor haberme brindado la oportunidad de realizar esta tesis doctoral, por las sugerencias, las correcciones y la supervisión llevada a cabo en la elaboración de esta memoria.

Un especial reconocimiento merece la Dr. Arantza Ugalde, por su valiosa orientación, su seguimiento y la continua supervisión del trabajo, sin la que no hubiera sido posible la realización de esta Tesis. Por su experiencia y su paciencia, por haber confiado en mi persona, por su incondicional apoyo tanto en los momentos de felicidad como en las peores crisis, por sus buenos consejos y su alto nivel de exigencia. Gracias por haber sido mi amiga y mi guía durante todos estos años.

I would like to thank Dr. Morgan Moschetti who advised me during internships and introduced me to the *ambient noise world*. Without his advice and insights I would have never been able to complete my research. I wish to express my sincere gratitude to Dr. Harley Benz from NEIC for hosting me to Golden, USA. And I would also like to extend my acknowledgements to the USGS Geological Hazard Seismic Center Staff.

Thanks to Dr. Robert Herrmann for the valuable discussions that helped me understand my research area better.

A mi buena compañera la Dr. Beatriz Gaite por su apoyo, su paciencia y su respuesta siempre positiva a resolver todas mis dudas. A Clara y Pilar por escuchar mis quejas y lamentos, por aguantar mis risas y por tolerar estoicamente mi mala costumbre de pensar en voz alta. A María Jesús le tengo que agradecer haber sido mi amiga en este largo proceso, su optimismo, su buen humor, su alegría, y las extrañas maravillosas cosas que sólo te puede pasar cuando compartes largas horas de carretera con ella.

Quizá hubiera sobrevivido a esta Tesis sin nuestros *catarsis coffees* pero no hubiera sido ni la mitad de divertida. A ti, Ana, por ser capaz de ir más allá, por tomarte la molestia de conocerme, escucharme y captar mi esencia.

I am also grateful my many friends that helped me adjust to a new country. I greatly value their friendship and support. I have to give a special mention for Sarah who always encouraged

me to keep going and Ezgi, Paul, Matt, Tingting, Mauriccio, Luca, Tyler and his funny roof parties, Giuseppe, Alex…. Y a mi twin, Irene, que me ha hecho creer en la existencia de las almas gemelas.

No puedo olvidarme de mi *Yellow Team*, ellos me han enseñado a disfrutar de cada momento, a ser feliz con lo que tengo mientras consigo lo que quiero. Ejemplo de superación y coraje, de compañerismo y amistad verdadera, siempre dispuestos a tender la mano, el pie y el cuerpo entero si fuera necesario. Porque me habéis hecho volver a creer en las personas y por mucho más vosotros sois mi familia aquí en Barcelona.

Mi agradecimiento más especial está dirigido a mi familia, a mis padres por inculcarme una buena escala de valores, y enseñarme que todo en la vida se alcanza con trabajo, humildad y constancia; a mi hermana por entenderme, escucharme y por considerarme lo suficientemente buena para cuidar su mayor tesoro; a mi sobrina por volverme loca a preguntas, por sentarse a mi lado a dibujar sismogramas y por todos sus abrazos espontáneos; a mi hada madrina por sus enseñanzas, consejos y cariño; a mi Tía y a mi prima Marta por ser ejemplo de lucha; y allá donde esté a mi Amparito que siempre me dijo que sólo los patitos feos se convierten en bellos cisnes.

Este trabajo de investigación se ha podido realizar gracias a la beca de investigación que me fue concedida dentro del programa de Formación de Personal Investigador (BES-2011-044291) asociada al proyecto MICINN (CGL2010-21568) de la Dr. María José Jurado del Instituto de Ciencias de Tierra Jaume Almera. Así mismo la elaboración de esta Tesis no hubiera podido ser posible sin la financiación del programa Consolider-Ingenio 2010 TOPO-IBERIA (CSD2006-00041), y el proyecto REPSOL CO-DOS.

ABSTRACT

In this thesis I have carried out a comprehensive study of the attenuation properties of the Earth´s crust of the Iberia-Morocco region (IMR). I have investigated the crustal attenuation by means of the quality factor *Q*, which is inversely proportional to attenuation, using both earthquakes and noise-derived measurements. In order to fulfill the thesis objectives a large dataset including earthquake waveforms and seismic noise records has been used.

Three different traditional earthquake methods have been implemented to estimate *Q* in the IMR: the two-station (TS) method, the coda normalization (CN) method and the spectral amplitude decay (SAD) method. For the estimation of *Q*, these approaches measure the spectral amplitude of the *Lg* wave (direct and coda) of regional events. Among all the methods evaluated, the TS method allows imaging the spatial variation of the *Lg* wave attenuation in the Iberian Peninsula whereas the coda normalization and the spectral amplitude decay methods only estimate average attenuation values as well as its frequency dependence.

For the Iberian Peninsula, high *Lg Q* values are observed in the stable Iberian Massif in western Iberia, while lower values are mainly found in the Pyrenean Range and in eastern and southern Iberia.

For Morocco, the coda normalization and the spectral amplitude decay methods produce similar results, indicating that the *Lg Q* models are robust to differences in the methodologies. The frequency-dependent *Q* estimates represent an average attenuation across a broad region of different structural domains and correlate well with areas of moderate seismicity.

Additionally, I have studied the *Lg* propagation efficiency across the IMR. Results reflect an inefficient or even blocked propagation across the Gulf of Cádiz and for most paths crossing the western Alboran basin. The continental crust of the Iberian Peninsula and Morocco shows efficient *Lg* propagation.

In this thesis I have also investigated the potential of using ambient noise measurements to retrieve information about the anelastic structure of the Earth´s crust. Since noise preprocessing techniques modify the amplitude of the recovered empirical Green function of the medium, additional tests have to be done in order to verify the reliability of the attenuation results obtained. In this regard, I have carefully examined the influence of the distribution of noise sources and receivers on *Q* estimates. Azimuthally and spatially averaged *Q* values derived from noise recordings were further compared with earthquake attenuation measurements. Results reveal that the average *Q* estimates are in concordance with previous long-period

surface-wave measurements from earthquakes in the central part of the Iberian Peninsula. Accurate *Q* estimates are also found in the Moroccan region.

I would like to emphasize that this thesis presents new contributions and improvements to the knowledge of the attenuation structure of the IMR. The first regional map that images the lateral variation of the *Lg Q* has been estimated for the Iberian Peninsula improving the spatial resolution of earlier studies. The frequency dependence of *Lg Q* has been also calculated for the first time in Morocco. Furthermore, this work is the first attempt to recover attenuation information from ambient seismic noise measurements in the study area. This novel technique allows us to investigate the attenuation structure of the Earth without the occurrence of earthquakes. Exploiting ambient seismic wavefields for attenuation studies will be a powerful tool to extract information about the anelastic structure and the geodynamics in areas of very low seismicity in the near future.

It should be also noticed that recovering crustal attenuation values is important for many reasons. Attenuation estimates can be used to better quantify the hazard associated with earthquake ground shaking. Attenuation is also a valuable property in exploration seismology. For example, the presence of fluids can significantly attenuate the amplitude of the seismic waves.

1. INTRODUCTION

Seismic waves can have natural causes such as earthquakes and volcanic eruptions or artificial human activities. The deeper layers of the Earth´s interior must be inferred from indirect methods because few kilometers in depth can be drilled and explored by artificial sources. In this regard, earthquakes provide valuable data for understanding the Earth´s properties and structure and its geodynamic evolution. Moreover, Seismology is used in exploration of natural resources, in the detection of nuclear explosion and in assessing and reducing earthquake hazards.

Information about crustal and upper mantle structure has been extensively obtained using controlled-source experiments such as reflection and wide-angle surveys, in addition to seismic waves generated by local, regional and teleseismic earthquakes. Active source surveys have knowledge of the source location and its origin time and control the source distribution but they are more expensive than those that use earthquakes. However, one of the main limitations associated with earthquake methods is the uneven geographical distribution of events and their irregular occurrence. The inhomogeneous distribution of local seismic sources defaults to teleseismic observations the investigation of aseismic areas. Therefore, new observational methods based on other seismic sources are needed in order to improve the earthquake resolution and to enhance the image of the near surface. In order to move beyond limitations of traditional methods based on earthquakes, recent developments in Seismology have acquired information about Earth elastic and anelastic properties from seismic ambient noise.

This thesis aims to study the attenuation structure of the crust from the analysis of earthquakes and ambient noise recordings.

1.1. Seismic Attenuation

Seismic waves lose energy as they propagate through the heterogeneous Earth structure. Seismic amplitudes are reduced with distance due to three factors: the geometrical spreading of the wavefront, the presence of inhomogeneities that refract, reflect or scatter the seismic energy and the intrinsic anelasticity associated with internal friction. The first two processes conserve the energy of the propagating wavefield and are described by elastic wave theory, whereas anelasticity involves energy loss due to non-elastic processes and is usually quantified by the parameter Q. The quality factor Q is a dimensionless parameter defined as the fraction of energy lost during a wave cycle

$$Q = 2\pi \frac{E}{\Delta E} \tag{1.1}$$

where E is the peak energy and ΔE represents the energy lost [*Aki and Richards*, 2002, page 162]. The attenuation of seismic waves is inversely related to Q. This means that regions with high Q are less attenuating than regions where Q is low. Therefore, it is common to talk about the inverse of the quality factor, Q^{-1}. Quality factor includes both intrinsic and scattering effects [*Wu*, 1985]. Measurements of intrinsic attenuation are often difficult to isolate from scattering attenuation contributions.

Seismic energy is spread over an increasing area as the wavefront propagates from the source. This effect is described by the geometrical spreading. The geometrical spreading is described In terms of the factor $r^{-\gamma}$, where r is the epicentral distance and γ the geometric spreading coefficient [*Aki and Richards*, 2002, page 217].

Attenuation has been observed to be mostly frequency-independent in the frequency range from about 0.001 to 0.1 Hz [*Stein and Wysession*, 2003]. At higher frequencies numerous studies have reported the frequency dependence of Q. The frequency dependence of Q is commonly modeled in the form of a power law [*Mitchell*, 1981]:

$$Q(f) = Q_0 \left(f / f_0 \right)^{\eta} \tag{1.2}$$

where f_o is the reference frequency (usually 1 Hz), Q_0 is Q at the reference frequency, and η is the frequency dependence exponent, which is assumed constant within the frequency band of interest.

Attenuation is sensitive to the varying tectonic environments, being lower in stable regions than in seismic, volcanic and tectonically active areas. Several factors have been suggested to explain these differences between active and stable regions: the presence of fractures that scatter seismic energy [*Aki*, 1980b]; variations in crustal thickness [*Kennett*, 1986]; and differences in the temperature of the crust [*Frankel et al.*, 1990]. The greater attenuation of the active areas is related to scattering losses and seems to be more important at high frequencies than at low frequencies [*Mitchell et al*., 1997]. Attenuation also varies in depth, reaching the highest values near the surface of the crust and the lowest at about 20-25 km [*Lay and Wallace*, 1995].

Regional variations in crustal Q are mainly studied by means of surface waves and regional phases such as *Lg* waves [*Mitchell and Romanowicz*, 1999]. The spatial attenuation of the surface waves is related to the quality factor by the expression [*Aki and Richards*, 2002, page 352]

$$Q = \pi f / \alpha U \tag{1.3}$$

where f is the wave frequency, α is the attenuation coefficient and U is the surface wave group velocity.

Numerous methods have been proposed to estimate crustal values of Q, such as the coda normalization method [*Aki*, 1980b; *Frankel et al.*, 1990], the spectral amplitude decay method [*Campillo, et al.*, 1985], the two-station method [*Xie and Mitchell*, 1990] and the reverse two-station method [*Chun et al.*, 1987] among others.

As mentioned earlier, the crustal structure of the Earth has been extensively studied using seismic waves generated by local, regional and teleseismic earthquakes. The Earth acts as a filter that attenuates and scatters the high-frequency information from teleseismic earthquakes. Therefore, traditional methods based on distant earthquakes present limitations to infer the structure of the near surface because waveform data measurements at periods less than 20 s are needed to extract information about the crust. New observational methods based on seismic noise fields have been used to improve the estimation of Q at shorter periods.

The ambient noise field is the continuous, spatially and temporally incoherent seismic wavefield. The seismic noise covers a wide spectrum of frequency ranging from tens of Hz to about 10^{-3} Hz. High frequency seismic noise (~0.5-60 Hz) is produced by human activity, wind or rushing waters. The so-called microseismic band (0.02-0.4 Hz) is mainly caused by the interaction of the oceans with the solid Earth. The spectrum of the microseismic band is

characterized by two peaks between 0.05-0.08 Hz (T=10-15 s) and 0.1-0.2 Hz (T=5-10 s) called primary and secondary microseism respectively (Figure 1.1). The primary microseism is generated in shallow waters through direct interaction of ocean waves with the seafloor in coastal regions [*Hasselmann*, 1969], while the secondary microseism is produced by the interaction of ocean waves traveling in opposite direction with similar frequencies [*Longuet-Higgins*, 1950]. Microseisms mainly consist of surface wave energy. The lowest frequency noise, called Earth's hum (~10^{-2}-10^{-3} Hz), corresponds to incessant excitation of the Earth's free oscillations by atmospheric perturbations and infragravity waves.

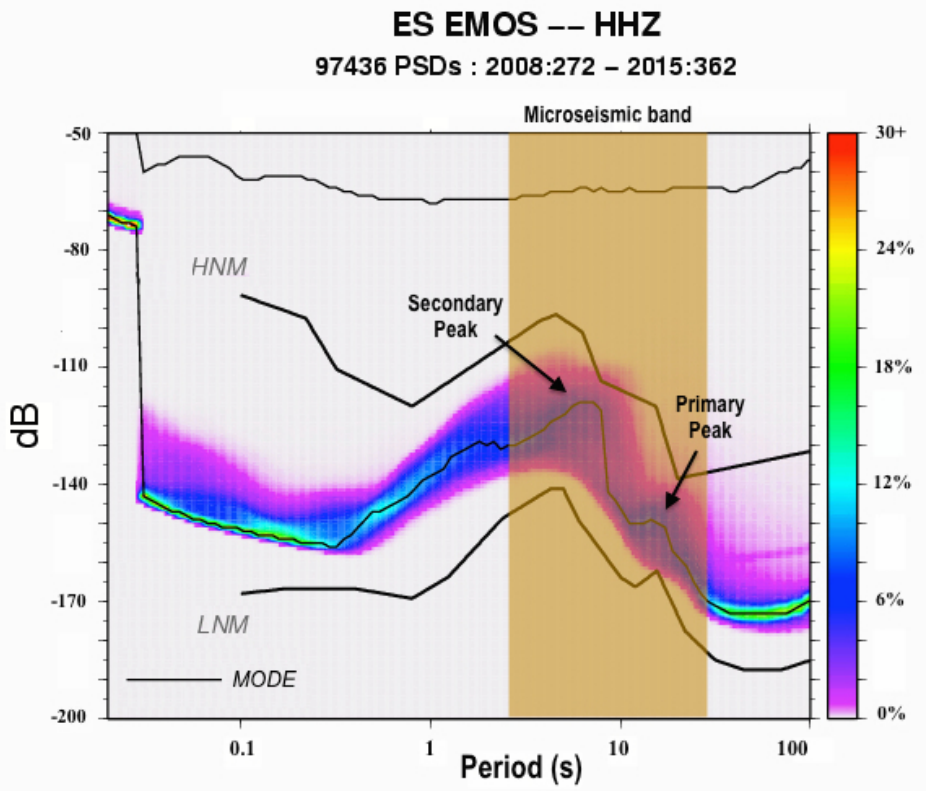

Figure 1.1: Envelope curves of acceleration noise power spectral density (PSD) in units of dB for the Iberian station EMOS (Teruel) during 2008-2015. The primary and secondary microseisms peaks are indicated. HNM and LNM indicate (black curves) the standard high and low noise model (*Peterson*, 1993), respectively. The most probable energy (mode) with respect to frequency is presented by a thin black line. Modified from *www.ign.es/ign/ layoutIn/sismoRuidoSismico.do*.

Passive seismic interferometry is a methodology that allows obtaining the empirical Green's function (EGF) of the medium by cross-correlating long time series of ambient noise recorded at two stations. *Aki* [1957] pioneered the use of cross-correlations of noise at different locations to retrieve dispersion of surface waves between stations. Using reciprocity theorem, *Claerbout* [1968] showed that the autocorrelation of the 1-D transmission response of a seismic noise

source would provide the reflection response. Later, he made an analogous conjecture extended to 3-D by cross-correlation of transmission responses recorded at two stations. *Lobkis and Weaver* [2001] demonstrated Claerbout´s conjecture using diffuse acoustic fields in laboratory experiments, and *Shapiro and Campillo* [2004] obtained successful empirical results. During the last decade, ambient noise studies have greatly advanced in imaging the shallow Earth structure [*Shapiro et al.*, 2005; *Yao et al.*, 2006; *Huang et al.*, 2010; *Lin et al.*, 2013].

Ambient noise studies have mainly focused on measuring group and phase velocity dispersion curves from the EGFs in order to estimate the Earth's velocity structure [e.g. *Shapiro et al.*, 2005; *Yao et al.*, 2006; *Villaseñor et al.*, 2007; *Lin et al.*, 2008; *Bensen et al.*, 2009]. More recently, several theoretical and observational studies have addressed the possibility of constraining seismic attenuation from the amplitude of the EGFs derived from ambient noise. The *Larose et al.*, [2007] experimental results and *Cupillard and Capdeville* [2010] theoretical simulations succeed in recovering amplitude decays from correlated noise records without pre-processing. *Cupillard and Capdeville* [2010] went a step further and proved that if noise sources were uniformly distributed, the EGF decay did not depend on the processing applied to the noise records. Subsequent analytic studies [e.g. *Tsai*, 2011; *Weaver*, 2011] also highlighted the importance of the source distribution in retrieving reliable attenuation information from noise measurements. However, it has been observed that noise sources are not uniformly distributed over the Earth's surface and vary spatially and temporally according to seasonal effects [e.g. *Stehly et. al*., 2006].

Prieto et al. [2009] proposed an approach to estimating 1-D depth profiles of surface wave attenuation using stacked cross-correlations of ambient noise. *Lawrence and Prieto* [2011] extended Prieto´s 2-D methodology and obtained attenuation maps at periods of 8-24 s for the western US. *Weemstra et al.* [2013] adapted Prieto´s approach to reservoir scales (~10-100 km) and estimated the frequency-dependent attenuation for Scholte waves. An alternative method was explored by *Lin et al.* [2011] who estimated amplitude decay rates in the time domain. They determined spatially averaged attenuation values from azimuthally averaged EGF amplitudes over large regions. *Zang and Yang* [2013] used the correlation of the coda of noise correlation method to determinate average attenuation values across the western US.

1.2. Thesis Overview

The research carried out in this thesis consists of studying attenuation properties of the crust of the IMR by combining regional earthquake measurements and ambient noise continuous recordings. The main objectives of this work can be summarized as follow:

i. Analyzing *Lg* and *Lg* coda spectral amplitudes from shallow regional earthquakes to investigate lateral variations and frequency-dependent characteristics of crustal seismic attenuation of the IMR.
ii. Investigating the relationship between *Lg* attenuation and main structural features of the study region.
iii. Obtaining the attenuation coefficients of fundamental-mode Rayleigh waves for the IMR from the amplitudes of cross-correlated noise recordings.
iv. Studying how Rayleigh wave EGF amplitudes are affected by the directionality of the seismic noise.
v. Comparing spatially and azimuthally averaged ambient noise attenuation results with time domain earthquake amplitude decay measurements.

These objectives have been addressed by means of two published papers [*Noriega et al.*, 2015a, 2015b] and third one that is about to be submitted. The two published articles utilized data of regional earthquakes and more precisely *Lg* waves (direct and coda) spectral amplitudes to investigate through different approaches the crustal attenuation of the IMR. In addition to earlier traditional approaches, ambient noise techniques have been also implemented in this work to retrieve the attenuation structure of the Iberia-Morocco crust.

The main theoretical aspects of the different methodologies used here will be reviewed in Chapter 2. Methods applied in this thesis have been chosen according to available data. It will be also explained in Chapter 2 how *Lg* wave and noise recordings have to be analyzed in every method to estimate *Q*. To obtain reliable attenuation results from amplitude measurements source and site effects must be estimated or cancelled [*Campillo*, 1987]. In this regard, the TS method allows removing the effect of the source radiation pattern by measuring amplitudes at two stations aligned with a common source. The CN method cancels source and site effects by dividing the amplitude of the direct waves by the amplitude of its coda whereas the SAD method simultaneously resolves source, site and attenuation terms.

Chapter 3 will present main results of this study. In this Chapter, we will estimate Rayleigh and *Lg* wave attenuation for the IMR. Inefficient propagation of *Lg* waves that travel across

oceanic crust forced us to resolve the *Lg* wave attenuation structure of the Iberian Peninsula and Morocco separately. Then, a regional map that images the spatial variation of *Lg Q* is presented for the Iberian Peninsula while averaged attenuation characteristics of the crust are inferred for Morocco. Finally, we will show spatially and azimuthally averaged Rayleigh *Q* values estimated from ambient noise for the IMR.

Chapter 4 provides a discussion about the attenuation results obtained. *Lg Q* estimates will be related to seismicity and main geological characteristics of the region. In this section, we will also examine the effect of the noise directionality on EGF amplitudes in order to investigate the reliability of the estimated EGF decay rates. Additionally, we will analyze the behavior of azimuthally and spatially averaged EGF amplitude decays at different frequencies and locations.

Final conclusions and main contributions of this thesis will be summarized in Chapter 5. Future research lines will also be proposed.

As has been described above, different methods and seismic data types have been analyzed in this thesis. Table 1.1 summarizes the main characteristics of each method.

Method	**Seismic Source**	**Seismic Wave**	**Domain**	***Q (f)***	**2D**	**Region**	**Advantages**	**Disadvantages**
TS	Eq.	*Lg*	F.D.	no	yes	IP	Spatial variation	Site effects ignored
CN	Eq.	*Lg* & *Lg* coda	F.D.	yes	no	M	Source & Site cancelled	Average values
SAD	Eq.	*Lg*	F.D.	yes	no	M	Source & Site resolved	Average values
TAD	Noise	Rayleigh	T.D.	no	no	IMR	No Eq. required Better resolution	Average values

Table 1.1: Main characteristics of the methods carried out in this thesis. TS, Two Station; CN, coda normalization; SAD, spectral amplitude decay; TAD, temporal amplitude decay; Eq., earthquake; F.D., Frequency Domain; T.D., Time Domain; IP, Iberia Peninsula; M, Morocco, IMR, Iberia-Morocco region.

1.3. Contributions of this Thesis

This thesis provides new information about crustal attenuation characteristics of the IMR. The main contributions of this study are:

i. The first 2D model of *Lg Q* for the entire Iberian Peninsula, which provides unprecedented detail of the attenuation properties of this region.
ii. The first *Lg Q* frequency dependent estimate for Morocco.
iii. The extension of the coda normalization method using *Lg* waves to distances up to 400 km.
iv. The first attempt to measure *Q* using ambient seismic noise in the IMR.
v. First comparison between noise and earthquake attenuation estimates in the IMR.

The *Lg Q* model obtained for the Iberia Peninsula has improved substantially the spatial resolution of previous *Lg* attenuation works. For instance, *Pujades et al.* [1990] used only 427 seismograms recorded at 13 stations distributed over the Iberian Peninsula to construct the coda *Q* map.

Moreover, the ambient noise study allowed us to investigate the near surface attenuation structure of the region. However, estimating reliable *Q* from ambient noise data to image lateral variations needs further investigation. Seismic noise attenuation is an advantageous technique in regions of low seismicity since attenuation results from EGF amplitudes can be extracted without occurrence of seismic events. The study region hass low-to-moderate seismicity mainly concentrated around the southern deformation zone that includes the Betic-Rif range, the Alboran basin, and the Gulf Cádiz, where some moderate-to-strong (M_w 6-7) earthquakes have occurred. Seismically active areas also include the Pyrenees, the northwestern Iberian Peninsula and the Middle Atlas and the Central High Atlas of Morocco. To point out this seismicity distribution, the shallow earthquakes (h < 30 km) of the last 30 years with magnitudes greater than 4 for the IMR and northern Africa have been plotted in Figure 1.2. The epicenter distribution observed in Figure 1.2 determines the path coverage of both regional phases and surface waves across the IMR. Hence, ambient noise methodology could help improving the knowledge of the attenuation structures of the IMR.

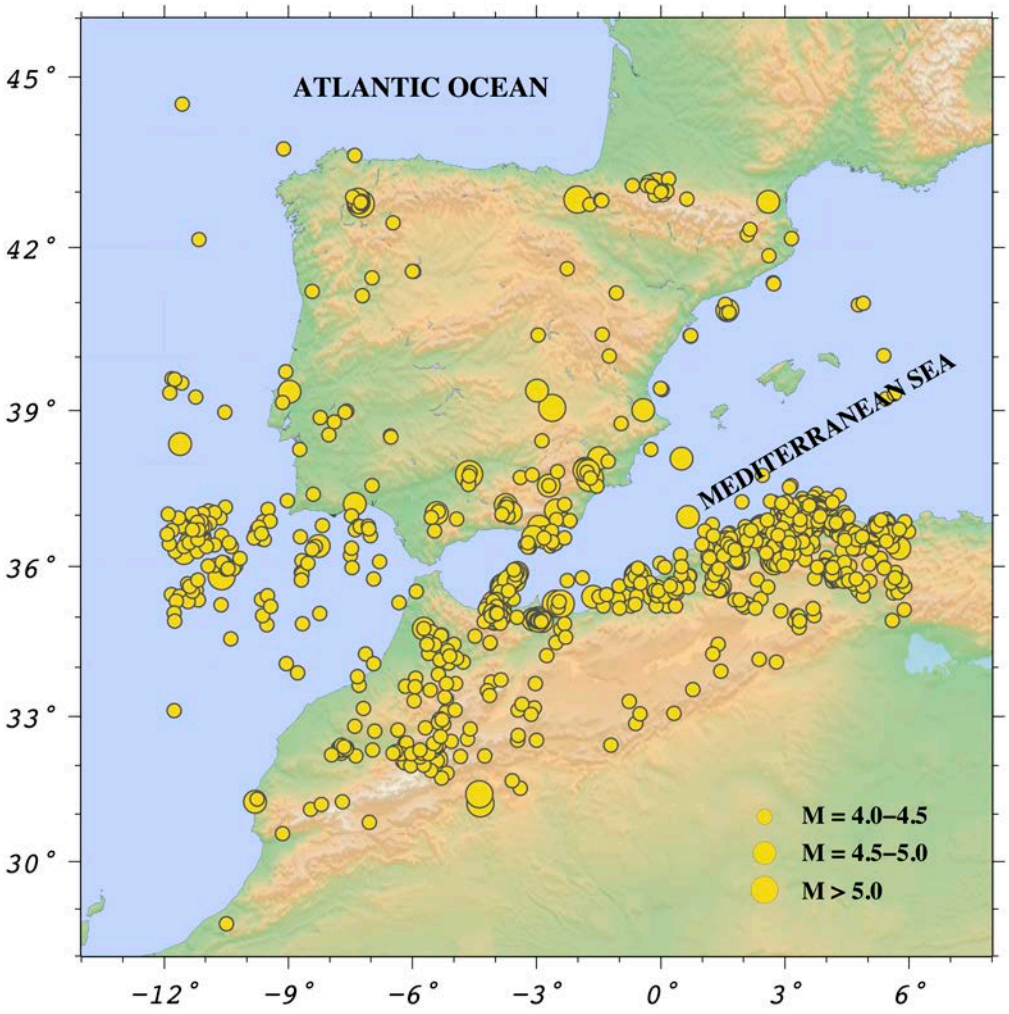

Figure 1.2: Epicenters of shallow earthquakes (h<30 km) with magnitudes greater than 4 that have occurred from 1 January 1985 to 31 December 2015 in the Iberia Peninsula and northwestern Africa. Data from the IGN (Instituto Geográfico Nacional) earthquake catalog (http://www.ign.es, last accessed: March, 2016)

Attenuation results obtained in this work may be useful for many applications. For instance, a detailed knowledge of the attenuation effects is a fundamental requirement to better quantify hazards associated with earthquake ground shaking [e.g. *Sonley and Atkinson*, 2006]. To better predict ground motion, Q has to be included in more realistic Earth models. Earthquake engineering could also consider our attenuation studies to develop the attenuation laws required to calculate ground motion parameters.

Site terms resolved in Morocco could also help to better quantify earthquake shaking. The assessment of seismic hazard has become progressively more important as a result of the threat posed to densely populated areas or critical infrastructures such as nuclear power plants. Moreover, future Q models inferred from noise measurements will improve estimates of previous traditional attenuation models.

1.4. Data

This work has been developed within the framework of the project *Topo-Iberia* inspired by the USA Earthscope program. This project established a high-density temporal network of broadband seismic stations (*IberArray*) that covered the entire Iberian Peninsula and surrounding areas in three successive deployments. The *IberArray* network together with datasets from coeval experiments, such as *PICASSO*, and the existing permanent networks provided an unprecedented simultaneous, dense coverage that allowed new contributions to seismological research in the IMR. The seismic database analyzed in this thesis was collected from a large number of broadband seismic stations operated by different institutions that are listed in Table 1.2 and shown in Figure 1.3.

Network Name	**Code**	**Network Type**
Topo-Iberia (IberArray), Spain	IB	Temporary
PICASSO, USA	XB	Temporary
University of Bristol, UK	ZI	Temporary
University of Münster, Germany	3D	Temporary
Pyrope, France	X7	Temporary
Instituto Geográfico Nacional (IGN), Spain	ES	Permanent
Institut Cartogràfic i Geològic de Catalunya (ICGC), Spain	CA	Permanent
Instituto Andaluz de Geofísica (IAG), Spain	IG	Permanent
Real Instituto y Observatorio de la Armada and Universidad Complutense de Madrid (ROA-UCM), Spain	WM	Permanent
RéNaSS and INSU/CNRS, France	FR	Permanent
Insituto Portugês do Mar e da Atmosfera (IPMA), Portugal	PM	Permanent
Instituto Dom Luiz (IDL), Portugal	LX	Permanent
GeoForschungs Zentrum (GFZ), Germany	GE	Permanent
Instituto Nazionale di Geofisica e Vulcanologia (INGV), Italy	MN	Permanent
Global Seismographic Network (GSN)	IU	Permanent

Table 1.2: Permanent and temporary portable networks operated by different institutions used in this thesis.

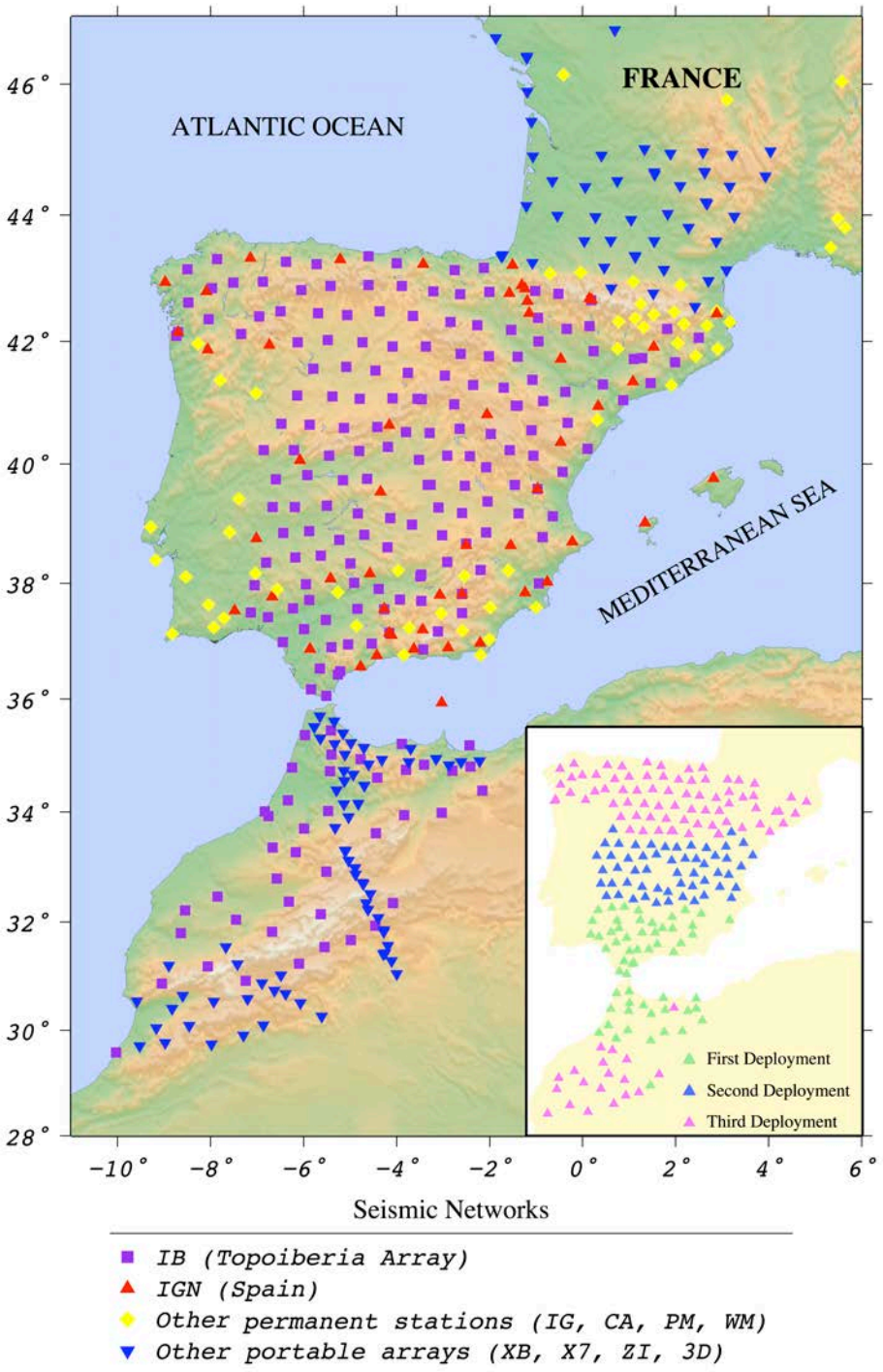

Figure 1.3: Locations of the broadband seismic stations used in this thesis. The inserted map indicates the three successive deployments of the IberArray

As a result of these improvements in seismic data quality and geographical coverage we were able to investigate and improve our knowledge of the attenuation structure of the IMR.

For the earthquake attenuation studies, using the IGN earthquake catalog we selected 59 events (h < 30 km) with magnitudes 3.1≤ m_{bLg} ≤5.4 for the Iberian Peninsula and 71 crustal earthquakes with magnitudes $m_b \geq 4$ for northern Morocco and Algeria. All used events occurred between January 2008 and December 2013. More than 9800 *Lg* waveforms were collected for the Iberia study and, resulting in 2480 interstation paths, while 1274 well-recorded *Lg* waveforms were used for Morocco.

For the noise attenuation studies, we analyzed two years of continuous ambient noise data recorded between January 2011 and December 2012.

Epicenters of the events utilized in this thesis are shown in Figure 1.4.

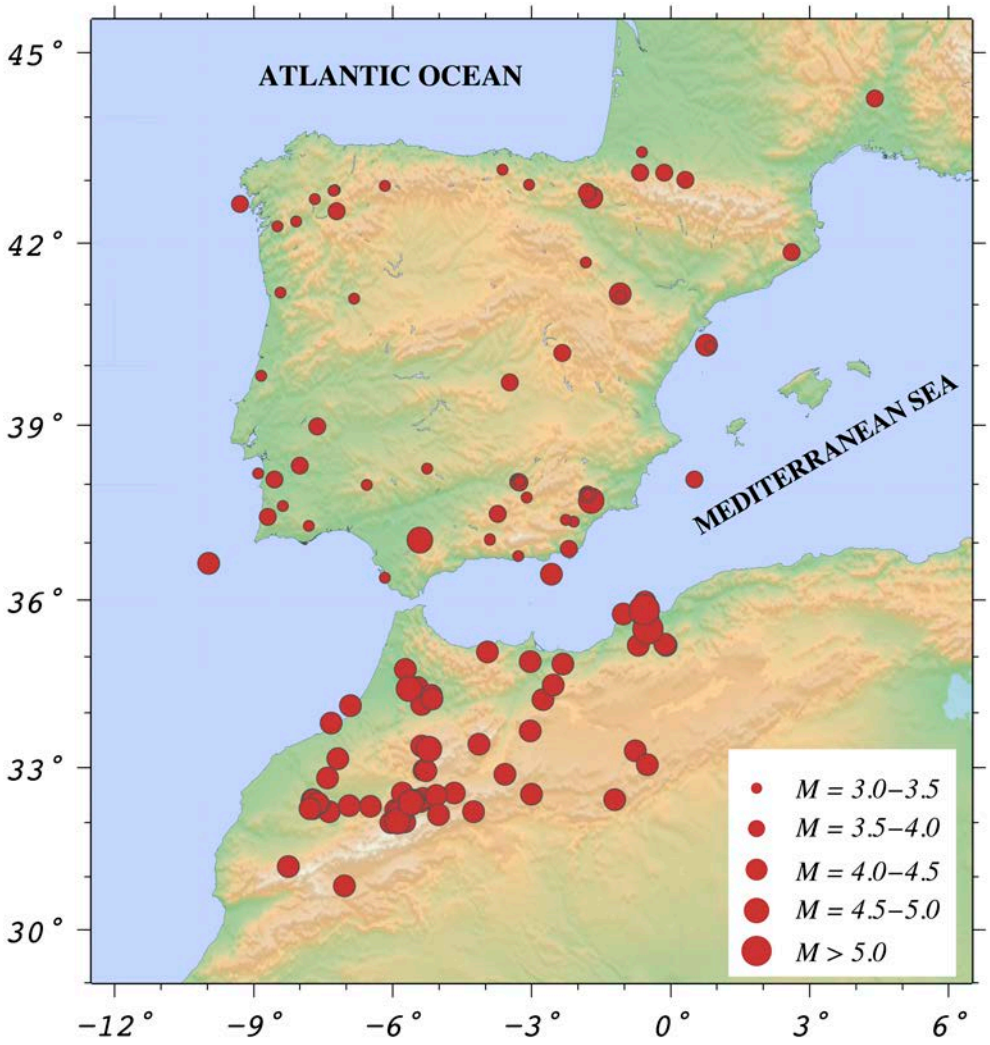

Figure 1.4: Shallow (*h* < 30 km) earthquake epicenters used in this thesis to infer *Lg* attenuation properties in the Iberia-Morocco region. Earthquake locations have been collected from the IGN Earthquake Catalog. Events are plotted according to magnitude.

2. METHODS AND DATA PROCESSING

In this Chapter, I will detail the methods used to study the attenuation structure of the Iberia-Morocco crust. The Chapter is divided into traditional methods, which involved earthquakes measurements, and ambient noise procedures. The best method to apply for a particular area will depend on several factors, such as the station coverage, the occurrence of earthquakes, or the suitability of the earthquake spatial distribution.

In this Chapter, I also describe the data processing associated with each implemented method.

2.1. Methods of Measuring Attenuation from Earthquakes

2.1.1. Two Station Method

The two-station method [*Xie and Mitchell*, 1990a] consists of taking the ratio of *Lg*-amplitude spectra for two different stations aligned with a common source. Denoting the two stations as *i* and *j*, the spectral ratio corrected for geometrical spreading is defined as:

$$R(f) = (\Delta_i^{1/2} / \Delta_j^{1/2})[A_i(f) / A_j(f)] \tag{2.1}$$

where Δ_i and Δ_j are the epicentral distances and $A_i(f)$ and $A_j(f)$ are *Lg*-amplitude spectra from the same event at frequency *f*. The square root of their epicentral distances cancels the geometrical spreading effect [e.g. *Xie et al*., 2004]. This method removes the source effect by taking the ratio of *Lg* spectra from the same event. The *Lg*-amplitude spectra, *A(f)*, at frequency *f* and epicentral distance Δ can be modeled as [*Xie et al*., 2004]:

$$A(f) = S(f)\Delta^{-1/2} \exp^{-\frac{\pi f \Delta}{Q(f)\beta}} X(f) \tag{2.2}$$

where *S(f)* is the source spectra, $\Delta^{-1/2}$ is the geometrical spreading term, *Q(f)* is the *Lg* quality factor, β is the *Lg* group velocity, typically 3.5 km/s, and *X(f)* accounts for a nonisotropic source-radiation pattern, focusing and defocusing, and site responses. The interstation *Q(f)* can be estimated using the TS method when *X(f)* is similar for the two stations and the event is recorded by two stations along the same great circle path. Assuming *Lg Q* frequency dependence model as Equation 1.2 and combining Equation 2.1 and Equation 2.2, the following relationship can be obtained:

$$\ln\left[\frac{\beta}{\pi\Delta_{ij}}\ln(R(f))\right] = (1-\eta)\ln f - \ln Q_0 \tag{2.3}$$

in which Δ_{ij} is the interstation distance. *Lg* Q_0 and η can then be estimated by means of a linear regression through Equation 2.3.

Because a geometry in which the TS pairs and the source are aligned perfectly is usually not possible, a difference between the azimuths from the source to the two stations $\delta\theta_{max}$ is allowed in practical analysis. According to *Der et al.* [1984] and *Xie et al*. [2004], a maximum allowable value of $\delta\theta_{max}$ is ±15°.

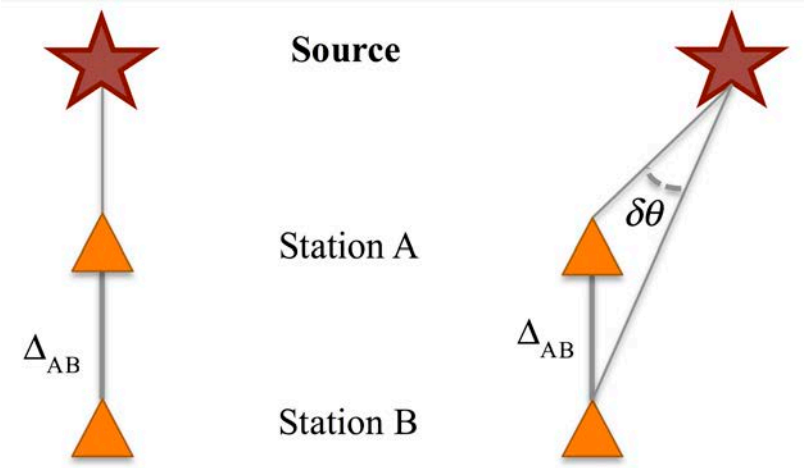

Figure 2.1: Left scenario shows an ideal recording geometry in which the event and the TS pairs are aligned perfectly whereas right scenario displays a more realistic geometry where azimuths from the source to the two stations vary by an amount of $\delta\theta$ allowing the application of the TS method.

As mentioned earlier, *Lg* Q_0 estimations may be also affected by modeling errors not accounted for in the TS method. Following *Xie et al*. [2004], the total error may be quantified by a factor of 1 ± δx. For small δx values, the relative error in *Lg* Q_0 estimations is related to the interstation distance Δ_{ij} by:

$$\frac{\delta Q_0}{Q_0} = \frac{\beta}{\pi}\left(\frac{Q_0}{\Delta_{ij}}\right)\delta x \approx 1.1\left(\frac{Q_0}{\Delta_{ij}}\right)\delta x \qquad (2.4)$$

Therefore, large interstation distances Δ_{ij} are required to keep the error in *Lg* Q_0 estimates low [*Xie et al*., 2004].

2.1.2. Coda Normalization Method

The coda normalization method (CN) derives from the single-station method proposed by Aki [1980b] to calculate shear wave *Q* within the crust. This technique estimates crustal *Q* values dividing the spectral amplitude of the direct shear waves by the amplitude of its coda. *Frankel et al.*, [1990] extended Aki's work to *Lg* waves, measuring the spectral amplitude recorded at different stations instead of studying several earthquakes recorded at different distances for a single station. The CN method is based on the idea that at some lapse time, the seismic energy is uniformly distributed in some volume surrounding the source. Although the origin of the approach is empirical [*Aki*, 1980b], the reliability of the results obtained in different studies confirms its validity [*Sato*, 1998].

The *Lg* spectral amplitude $A_{Lg}(r,f)$ observed at a given hypocentral distance r and frequency f can be modeled as

$$A_{Lg}(r,f) = R_{\theta,\phi} S(f) I(f) G(f) r^{-\gamma} e^{-\pi f r/Q(f)\beta} \tag{2.5}$$

where $R_{\theta,\phi}$ is the radiation pattern, $S(f)$ is the source spectra, $I(f)$ is the instrument response, $G(f)$ is the site amplification, γ is the geometrical spreading factor, $Q(f)$ is the *Lg* quality factor and β is the average *Lg* group velocity.

The *Lg* coda spectral amplitude $A_{Lg}^{C}(f,t_c)$ at a given lapse time t_c after the earthquake origin time can be written as

$$A_{Lg}^{c}(f,t_c) = S(f) I(f) G(f) C(f,t_c) \tag{2.6}$$

where $C(f,t_c)$ represents the coda envelope shape that describes how the coda spectral amplitude decays with time. It has been observed that the coda envelopes have a common shape that is independent of the source-receiver distance when a t_c greater than about twice the *Lg* wave travel time is selected [*Aki*, 1969; *Aki and Chouet*, 1975; *Frankel et al.*, 1990]. Therefore, the amplitude of the envelope varies only with source and recording site amplification factors. An example of coda envelope shapes for Moroccan stations recording the same earthquake at different hypocentral distances and azimuths is shown in Figure 2.2. Since the site amplification for the coda and direct waves is the same [*Tsujiura*, 1978], the ratio between the direct *Lg*-wave amplitude and its coda removes the site amplification factor as well as the instrument response and the source excitation. However, the CN method does not remove the effect of the radiation pattern, but it can be smoothed by choosing many events in a wide range of azimuths [*Frankel et al.*, 1990].

Dividing Equation 2.5 by Equation 2.6 and taking natural logarithms yields:

$$\ln\left(\frac{A_{Lg} r^{\gamma}}{A_{Lg}^{C}(f,t_c)}\right) = -\frac{\pi f}{Q\beta} r + \ln\left(\frac{R_{\theta,\phi}}{C(f,t_c)}\right) = -\frac{\pi f}{Q\beta} r + c(f) \tag{2.7}$$

Equation 2.7 describes a line whose slope is related to Q^{-1}. Therefore, Q is estimated from Equation 2.7 by means of a linear regression.

Figure 2.2 illustrates smoothed envelopes at a central frequency of 3 Hz for four different stations. Figure 2.2 shows that for lapse times greater than about 125 s the coda envelope shapes of the earthquake recorded at different stations are similar.

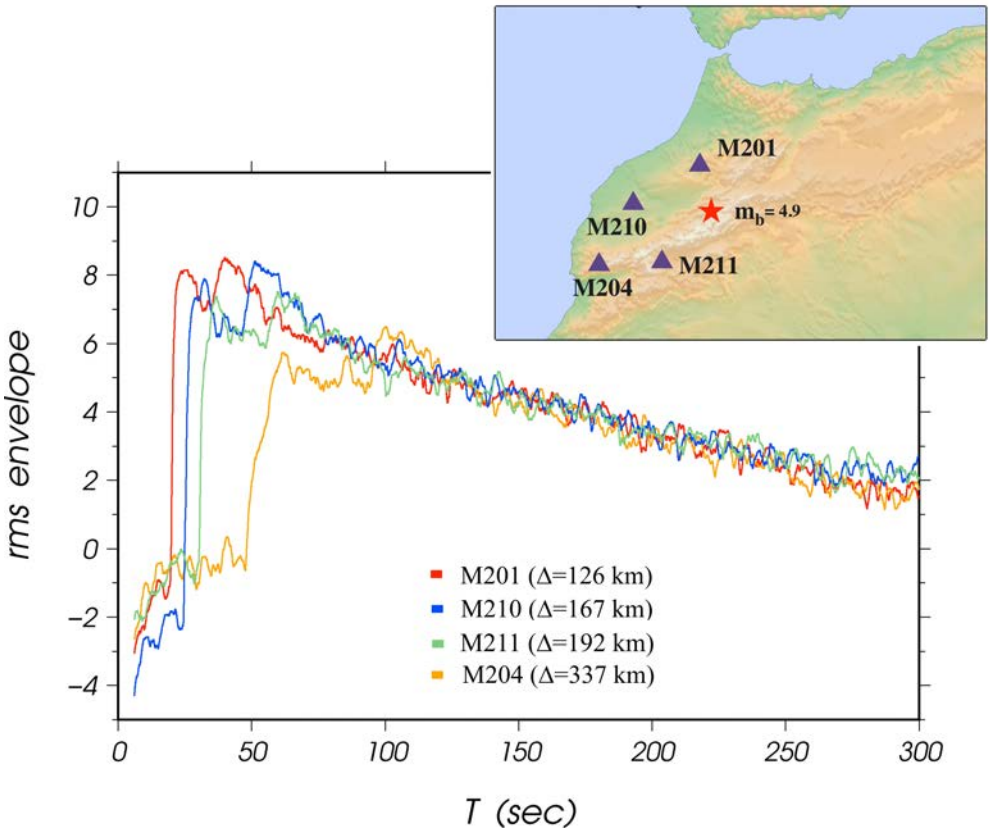

Figure 2.2: Examples of root-mean-square (rms) envelopes of seismograms at central frequency *f*=3 Hz. of an earthquake in Morocco versus lapse time after the event origin time for different stations recording the same event.

2.1.3. Spectral Amplitude Decay Method

The spectral amplitude decay method [Campillo et al., 1985; McNamara et al., 1996] allows quantifying the attenuation of the crust using the *Lg* spectral amplitudes of earthquakes occurred within a region.

According to Equation 2.5, the instrument-corrected *Lg* amplitude A_{ij} at frequency f for the jth earthquake recorded at the ith station can be written as

$$\ln A_{ij}(f) + \gamma \ln r_{ij} = \ln G_i(f) + \ln S_j(f) - \frac{\pi f r_{ij}}{Q(f)\beta}, \; i = 1,...,n; \; j = 1,...,m \qquad (2.8)$$

where r_{ij} is the epicentral distance, $S_j(f)$ is the source spectra, $G_i(f)$ is the site amplification, γ is the geometrical spreading factor, $Q(f)$ is the *Lg* quality factor and β is the average *Lg* group velocity. The source radiation pattern is assumed to be averaged out over multiple events and paths [*McNamara et al.*, 1996; *Benz et al.*, 1997]. When the left-hand side of Equation 2.8 is

plotted versus distance r_{ij}, the right-hand side describes a line where the receiver (G_i) and source (S_j) terms control the intercept and the Q^{-1} term controls the slope. Therefore, a system of linear equations based on Equation 2.8 can be obtained by measuring the instrument-corrected *Lg* amplitude at a single frequency for many source-receiver pairs. The system of equations can be expressed as

$$\mathbf{y} = \mathbf{A}\mathbf{x} \tag{2.9}$$

where **y** is a vector composed of the left-hand side terms of Equation 2.8, **A** is the coefficient matrix made up of the right-hand side parameters of Equation 2.8, and **x** is the column vector of unknowns: $G_i(f)(i=1,...,n)$, $S_j(f)(j=1,...,m)$ and Q. **A** is mostly composed of ones and zeros, with the last column corresponding to the last term of 2.8 ($-\pi f r_{ij}/\beta$) (see Equation 2.11). Equation 2.9 represents a typical linear inversion problem and can be solved using a singular value decomposition (SVD) inversion technique [*Menke*, 1980] to simultaneously invert for: the n receiver terms, which account for site amplification; the m source factors; and a regionally averaged Q for each center frequency. Then, Equation 2.9 has $m \times n + 1$ unknowns for a $n \times m$ number of equations so that an additional constraint is required. The inversion is constrained by requiring that the sum of all stations terms equals zero [*Ottemöller et al.*, 2002] that implies to consider the following additional equation in 2.9,

$$\sum_{i=1}^{n} \ln G_i(f) = 0 \tag{2.10}$$

Taking into account the additional constraint Equation 2.10, the matrices of Equation 2.9 can be written as follows:

$$\begin{bmatrix} 1 & 0 & \dots & 0 & 1 & 0 & 0 & \dots & 0 & 0 & -\left(\frac{\pi f r_{11}}{\beta}\right) \\ 1 & 0 & \dots & 0 & 0 & 1 & 0 & \dots & 0 & 0 & -\left(\frac{\pi f r_{12}}{\beta}\right) \\ \vdots & \vdots & \vdots & \vdots & \vdots & \vdots & \vdots & \vdots & \vdots & \vdots & \vdots \\ 1 & 0 & \dots & 0 & 0 & 1 & 0 & \dots & 0 & 0 & -\left(\frac{\pi f r_{i(j-1)}}{\beta}\right) \\ 0 & 0 & \dots & 1 & 0 & 0 & 0 & \dots & 0 & 1 & -\left(\frac{\pi f r_{ij}}{\beta}\right) \\ 0 & 0 & \dots & 0 & 1 & 1 & 1 & \dots & 1 & 1 & 0 \end{bmatrix}_{(mn+1)\times(m+n+1)} \times \begin{bmatrix} \ln S_1(f) \\ \vdots \\ \ln S_j(f) \\ \ln G_1(f) \\ \vdots \\ \ln G_i(f) \\ Q_{ij}^{-1} \end{bmatrix}_{(m+n+1)\times 1} =$$

$$\begin{bmatrix} \ln A_{11}(f) & + & \gamma \ln r_{11} \\ \ln A_{12}(f) & + & \gamma \ln r_{12} \\ & \vdots & \\ \ln A_{i(j-1)}(f) & + & \gamma \ln r_{i(j-1)} \\ \ln A_{ij}(f) & + & \gamma \ln r_{ij} \\ & 0 & \end{bmatrix}_{(mn+1)\times 1} \tag{2.11}$$

From Equation 2.11 each data observed at one station from one event can be used to construct the rows for matrices and **A** and **y**. The inversion is resolved for individual frequencies independently in order to determinate the unknown variables $G_i(f)$, $S_j(f)$, and Q for each frequency.

2.2. Earthquake Data Processing

Lg waves are often the most prominent seismic phases observed over continental paths at regional distances. They are usually accompanied by long durations of coda. They were identified by *Press and Ewing* [1952], and can be modeled either as a superposition of higher-mode surface waves or as multiple reflected crustal-guided *S* waves [*Kennett*, 1986]. *Lg* phases are generally observed in a group velocity window between 3.6 and 2.8 km/s in a relatively wide frequency band of 0.2-10 Hz [*Pasyanos et al.*, 2009; *Singh et al.*, 2012]. *Lg* amplitude is strongly affected by changes in crustal thickness, discontinuities within the crust, and variations of the crustal properties along its path [e.g. *Kennett*, 1986; *Mitchell*, 1995], hence they have been used in a variety of studies to investigate the crustal structure [*Mitchell and Romanowicz*, 1999]. Examples of *Lg* waves followed by its coda wavetrain are shown in Figure 2.3 for the M_w 5.1 May 11, 2011 Lorca Earthquake.

I will detail how *Lg* spectra were computed from the vertical component of the seismograms. In this thesis, I only analyzed vertical-component *Lg* recordings to avoid complications with fundamental-mode Love-wave energy on the transverse components [*Fan and Lay*, 2003]. Instrument responses were deconvolved for each seismogram to yield ground displacement. All waveforms used in this study were visually inspected.

Procedures for measuring *Lg* spectral amplitude have been performed differently according to each of the methods outlined earlier. Steps involved in each method of analysis are presented in next the paragraphs.

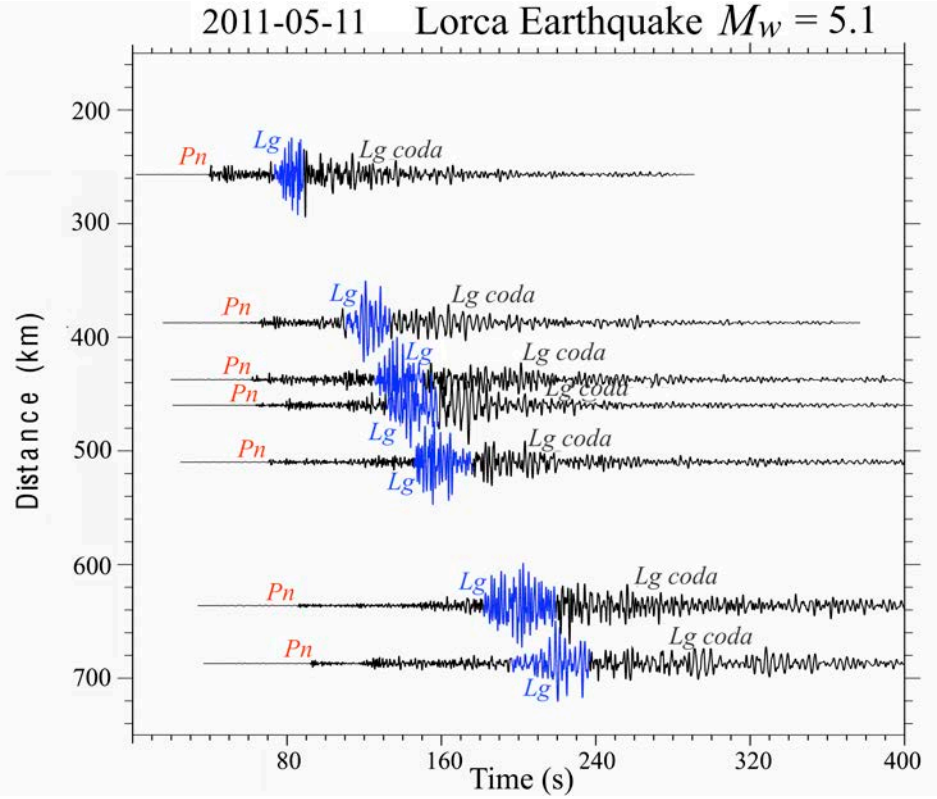

Figure 2.3: Examples of *Lg* and *Lg* coda waveforms filtered between 0.5-5 Hz of the Lorca Earthquake recorded at different stations. *Lg* phases are windowed from 3.5 to 2.9 km/s. *Pn* arrival is also marked.

2.2.1. Two Station Measurements

For the TS method we selected *Lg* waveforms with epicentral distances between 100 and 1000 km. The *Lg* spectral amplitudes were computed as follows. *Lg* phase is windowed using group velocities of 3.5-2.9 km/s for all the paths except those crossing the Pyrenean range, for which more accurate values of 3.4-2.8 km/s were recognized after visually inspection. Similarly, we selected a time window after the *Pn* onset, starting at 8.3 km/s and having the same length as the *Lg* window. Then, we applied the fast Fourier transform to the two windows and smoothed the amplitudes by means of a 50% overlapped, 15-point moving window in the frequency domain. As a threshold for assuring the existence of an *Lg* phase, we only kept for further analysis those *Lg* spectral amplitudes greater than four times the *Pn* window spectral amplitudes.

The process followed to compute *Lg* spectral amplitude is illustrated in Figure 2.4.

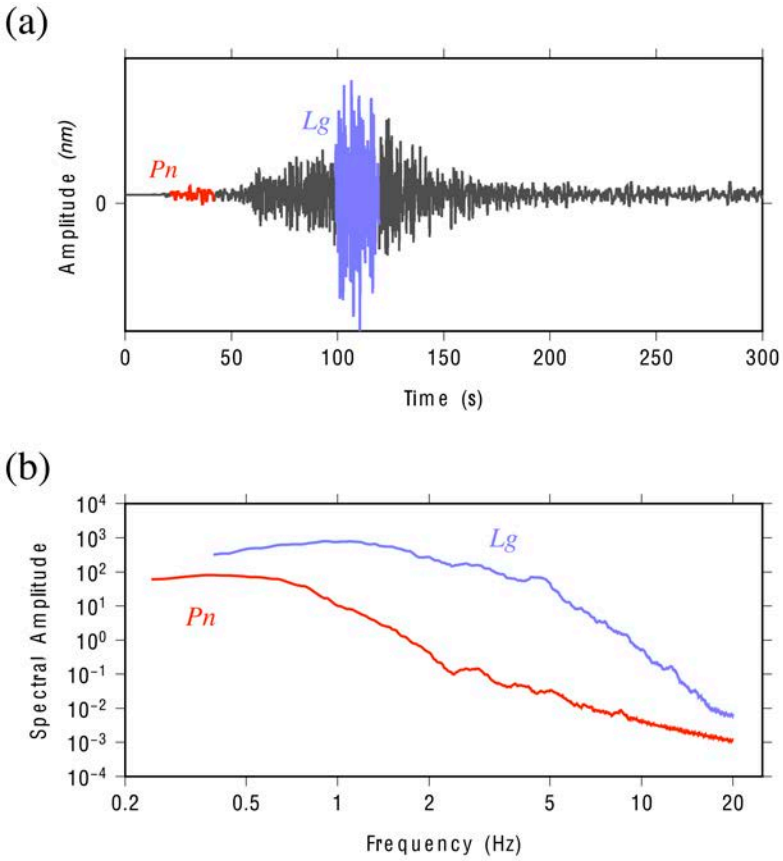

Figure 2.4: (a) An example of bandpass filtered (0.5-5 Hz) waveform of the vertical component of the displacement seismogram. Both *Lg* and *Pn* windows are enhanced in blue and red respectively. (b) Smoothed *Lg* and *Pn* spectra.

Once *Lg* spectral amplitudes were obtained, we calculate interstation *Lg* Q_0 values using Equation 2.3. The TS paths were chosen so that they were aligned with the common source using an angle of $\delta\theta_{max} = \pm 15°$ (explained in 2.2.1). Then, we calculated the ratios of *Lg* spectra and epicentral distances for every TS path using Equation 2.1 and estimated *Lg* Q_0 and η by means of a linear regression using Equation 2.3. Only estimates with correlation coefficients of the regression fit greater than 0.7 were used. A minimum interstation distance of 225 km is considered according to Eq.(2.4) if a modeling error δx of 0.2 km^{-1} is assumed. In addition to all the previous selection criteria, the remaining paths after the processing were manually reviewed to ensure the quality of the measurements.

Conditions imposed above yielded 2480 high quality interstation paths from the initial dataset of 9800 seismograms. The final TS paths are shown in Figure 2.5. The epicenters used are also plotted.

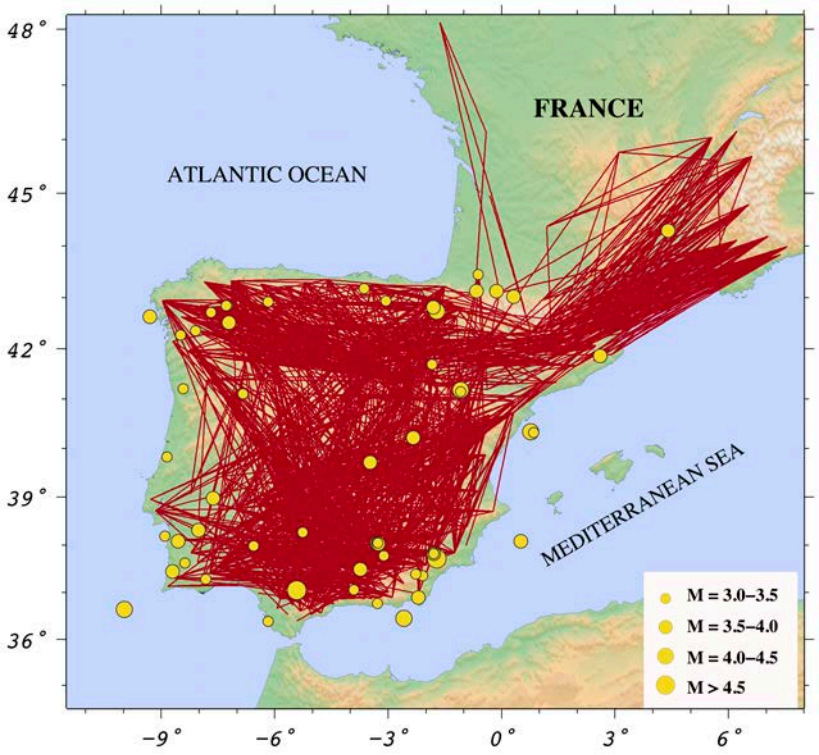

Figure 2.5: TS paths and epicenters of the earthquakes used to estimate *Lg* attenuation of the Iberian Peninsula.

2.2.2. Coda Normalization Measurements

Waveform data analyzed for the CN method involved earthquakes with hypocentral distances from 100 to 400 km. The *Lg* spectral amplitude $A_{Lg}(r, f)$ was measured every quarter octave between 0.9 and 7.3 Hz center frequencies as the root mean square (RMS) of the *Lg* window spectral amplitude. The *Lg* coda spectral amplitude $A^{c}_{Lg}(r, f)$ was determined from the RMS spectral amplitude of the coda for a reference time window centered at t_C. We used a 10 s long reference time window centered at 170 s past the origin time of the earthquake. Only data with amplitudes greater than twice the maximum RMS spectral amplitude of a noise sample of length 10 s prior to the *Pn* wave onset were considered for the calculations. In the estimations of signal-to-noise ratios, we added a factor $1/2 \log(T_s/T_n)$ to the logarithm of the noise to account for the different lengths of the signal (T_S) and noise (T_N) [*Taylor et al.*, 2002].

Figure 2.6 shows an example of spectral amplitudes of an earthquake with hypocentral distance of 237 km.

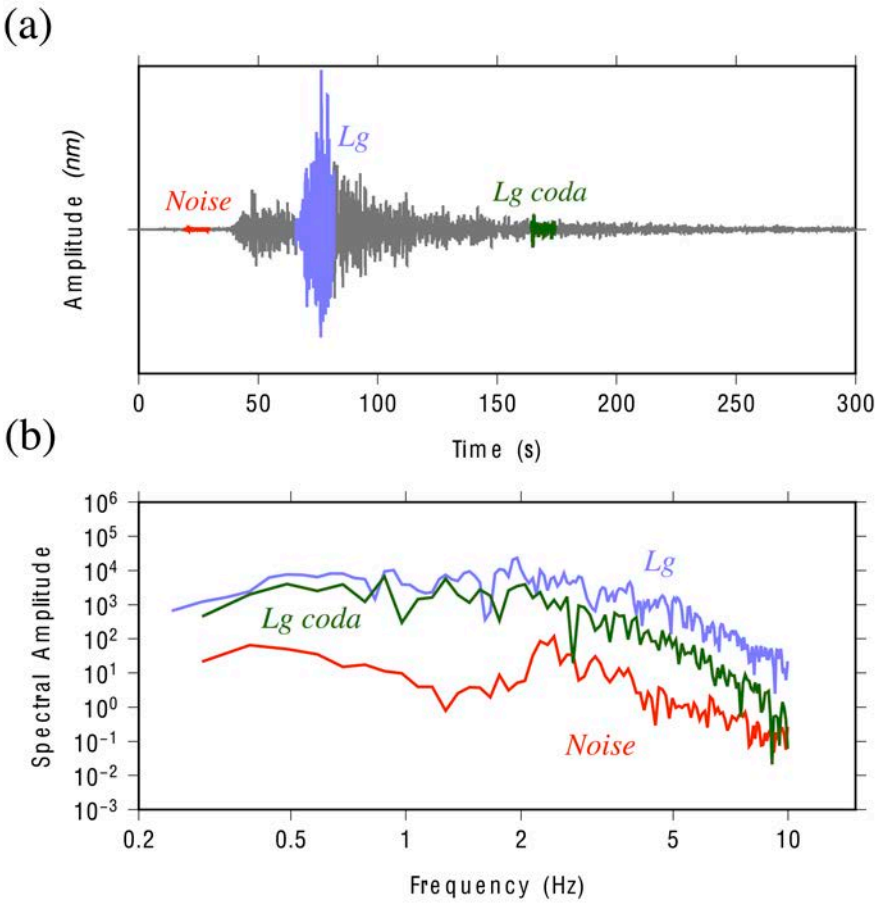

Figure 2.6: (a) Waveform of the vertical component of the displacement seismogram. *Lg*, *Lg* coda and noise windows are enhanced in blue, green and red respectively. (b) *Lg*, *Lg* coda and noise spectral amplitudes.

The lapse time t_C =170 s was estimated for an average *Lg*-wave velocity of β = 3.5 km/s that satisfies the condition $t_C > 2r/\beta$ for most of the data ($t_C > 1.5r/\beta$ for the most distant station). This value was chosen after some tests on the final results as a compromise between having enough data measurements and measuring the coda at long lapse times. Its validity was confirmed by analyzing some examples of recorded envelopes as a function of lapse time after the earthquake origin time. Figure 2.7 reflects an increase of the RMS of the coda envelopes with increasing magnitudes for a single station that records different events at different azimuths. Combining waveforms of several events recorded at different stations Equation 2.7 is resolved in each frequency band by means of a linear regression in which the slope is related to Q^{-1}.

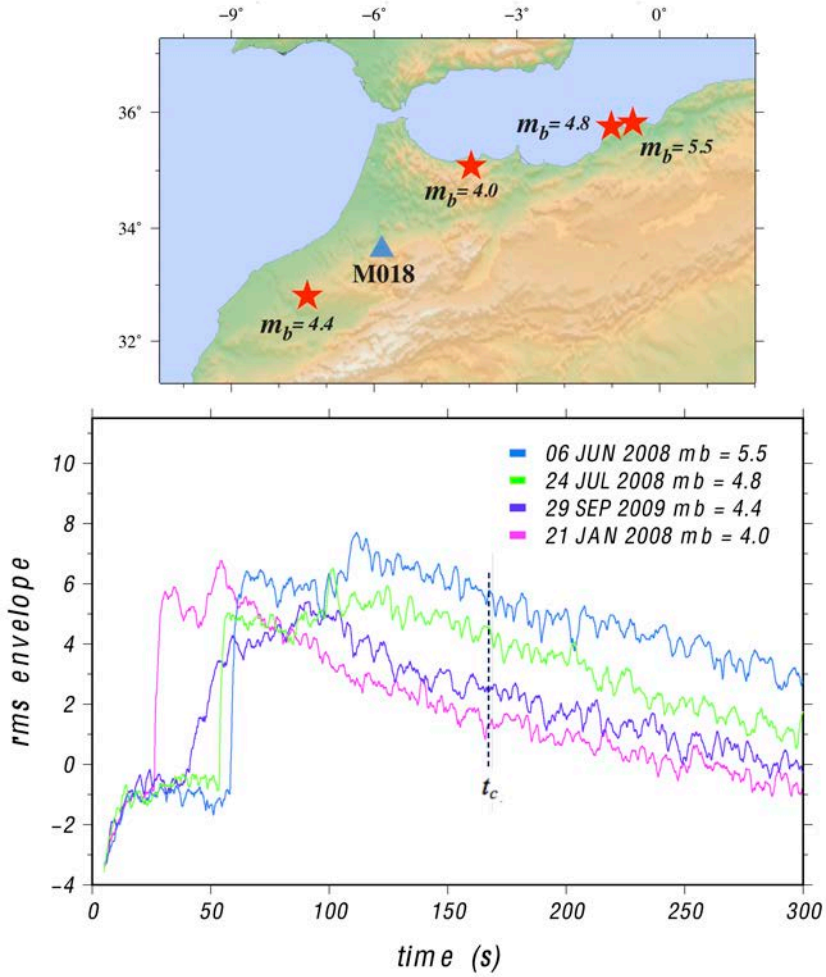

Figure 2.7: Examples of RMS envelopes of seismograms at central frequency f=3 Hz of different events recordings at the same station versus lapse time after the event origin time. The coda reference time t_c is indicated. Geographic location of the recording station and epicentres of the events are plotted in the upper panel.

2.2.3. Spectral Amplitude Decay Measurements

For the SAD method, the spectral amplitude of the *Lg* waveform A_{Lg} was measured following the procedure described above for the CN method. In order to estimate spectral amplitudes corrected for source and site terms, the system of equations (2.11) was solved using a SVD inversion technique for each frequency band independently. In this study we assumed a frequency-independent average *Lg*-wave velocity of β = 3.5 km/s and a constant geometric spreading coefficient of γ = 0.5.

Estimations of *Lg Q* from SAD methodology were carried out using both the complete data set (waveforms with hypocentral distances from 100 to 900 km) and data with hypocentral distances up to 400 km (to be comparable with the CN method). Spectral amplitudes measured from the original *Lg* waveforms were then used to resolved Equation 2.10.

Figure 2.8 shows an example of *Lg* arrivals filtered every quarter octave in the time domain between 1.0 and 8.0 Hz.

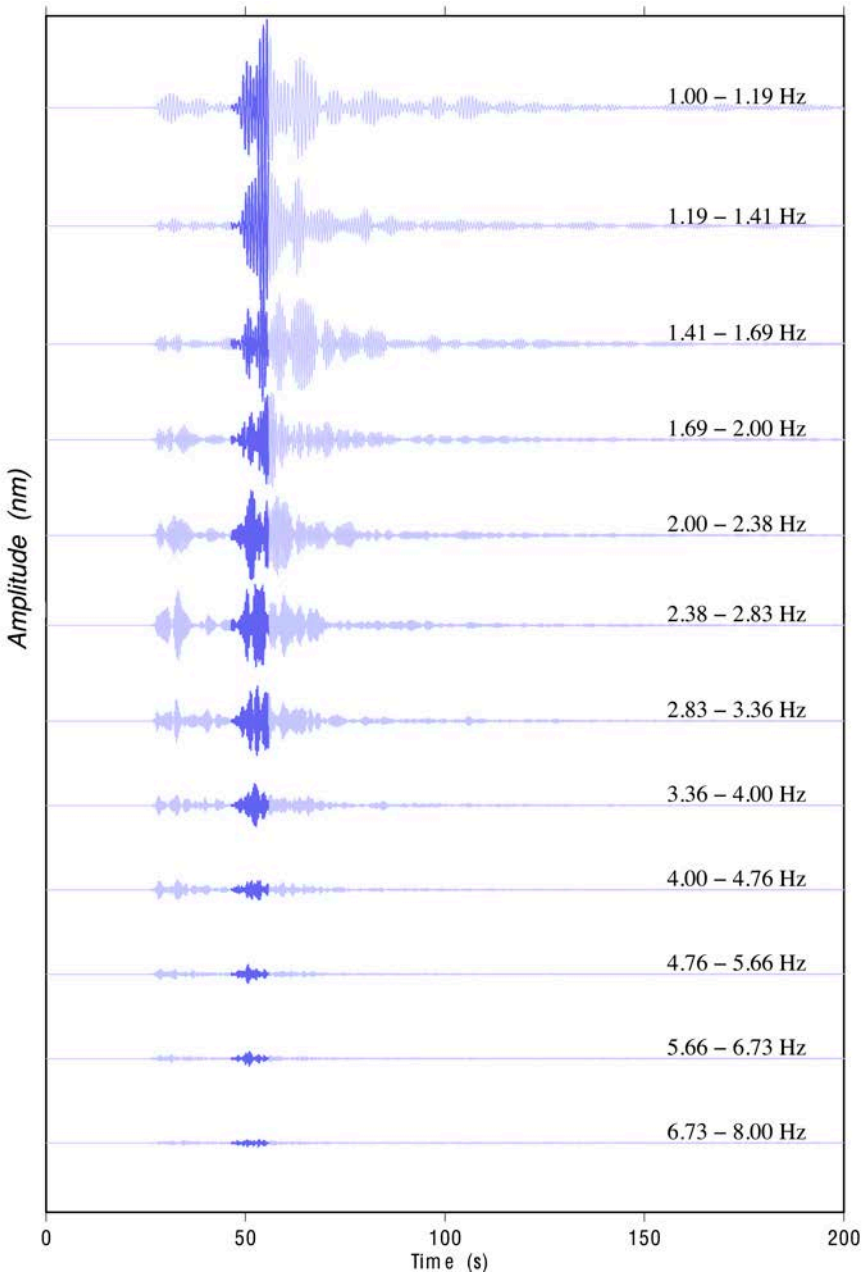

Figure 2.8*:* Example of *Lg* waveforms filtered every ¼ octave between 1 and 8 Hz from an earthquake located in Morocco and recorded at station M210 (Δ=167 km). *Lg* phases windowed between 3.0.0-3.6 km/s are highlighted. All traces are plotted on the same scale.

2.3. Method for Measuring Attenuation from Ambient Noise

Passive seismic interferometry (PSI) is based on the idea of retrieving the empirical Green´s functions between two receivers by cross-correlating long time series of ambient noise recorded at the two stations. The emerged EGF can be considered as a seismogram recorded at one receiver due to an impulsive force located at the other. Therefore, EGFs contain information about the medium between the two receivers. The cross-correlation between two observed fields at $\boldsymbol{r_A}$ and $\boldsymbol{r_B}$ generated by independent sources is proportional to the inter-receiver Green´s function [e.g. *Wapenaar*, 2004]:

$$\boldsymbol{G(r_B,r_A,t)+G(r_B,r_A,-t)} \propto \left\langle \boldsymbol{u(r_B,t)*u(r_A,-t)} \right\rangle \qquad (2.12)$$

where $\boldsymbol{G(r_B,r_A,t)}$ denotes the Green´s function between stations $\boldsymbol{r_B}$ and $\boldsymbol{r_A}$ and $\boldsymbol{u(r,t)}$ is the wavefield recorded at position $\boldsymbol{r}$ and time $\boldsymbol{t}$. To retrieve Green´s functions through Equation 2.12, energy flux in the ambient wavefield should be equipartitioned [*Lobkis and Weaver*, 2001] and sources surrounding the two stations should be uncorrelated [*Wapenaar and Fokema*, 2004]. Figure 2.9 shows two stations at positions $\boldsymbol{r_A}$ and $\boldsymbol{r_B}$ that are surrounded by random energy sources (blue arrows).

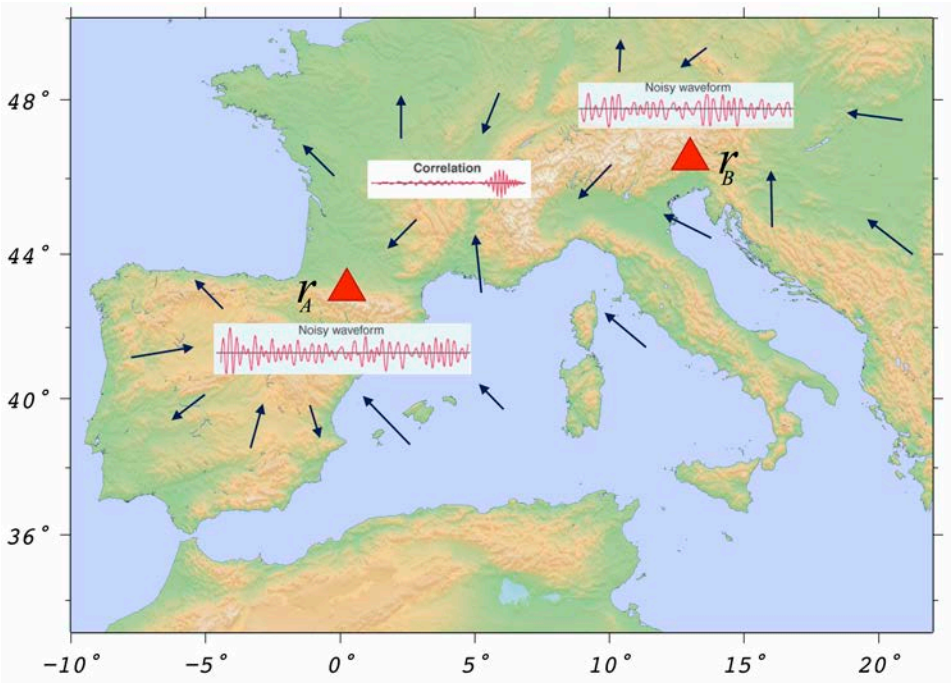

Figure 2.9: Schematic explanation of PSI. Random ambient noise wavefield (blue arrows) is recorded by two receivers. Empirical Green´s function is retrieved from the cross-correlation of the noise waveform detected at both stations.

As has been mentioned before, the surface waves fraction of the EGFs extracted from noise fields emerges more clearly because noise sources are mainly situated near the Earth's surface. Surface waves are prominent on seismograms at large epicentral distances because their energy rate decay only as $r^{-1/2}$. As a result, they can circle the globe many times after a large earthquake. Surface waves can be divided into two types: Love waves, which move transversely to the ray direction, and Rayleigh waves, which are a combination of longitudinal and vertical motions [e.g. *Stein and Wysession*, 2003]. Dispersion is an important feature of surface waves meaning that different periods travel at different velocities. Hence, surface wave arrivals are spread out in time. This thesis has focused on Rayleigh waves because we have only analyzed the vertical components of the noise records.

To retrieve Rayleigh wave EGFs from ambient noise recordings, we have applied the standard ambient noise preprocessing [*Bensen et al.*, 2007] that includes:

i. Removing the instrumental response, the mean and the data trend.
ii. Bandpass filtering between 1-150 s.
iii. Applying a temporal normalization by computing the running average of the absolute value of each seismogram in a fixed window length of 128 s.
iv. Applying spectral whitening.
v. Cross-correlating all vertical station pairs using 4-hours-long windows with 10 minutes window of overlap.
vi. Stacking about 2 years of cross-correlated waveforms to enhance SNR.

Once the time series have been processed, the entire dataset consists of 86,397 EGFs. We have followed the method described by *Lin et al.* [2011] to recover Rayleigh wave attenuation measurements from noise fields. Figure 2.10 presents examples of broadband vertical-component EGFs sorted by distance and filtered between 10-20 s period for different station-pairs which have GUD as a common station. The EGF asymmetry observed in Figure 2.10 between positive and negative correlation lags results from an inhomogeneous distribution of ambient noise sources [e.g. *Stehly et al.*, 2006]. Since correlated waveforms are strongly influenced by the noise source distribution, ambient noise attenuation studies require knowledge of this influence on EGF amplitudes. On the other hand, to investigate methods that allow locating noise sources is beyond the scope of this thesis.

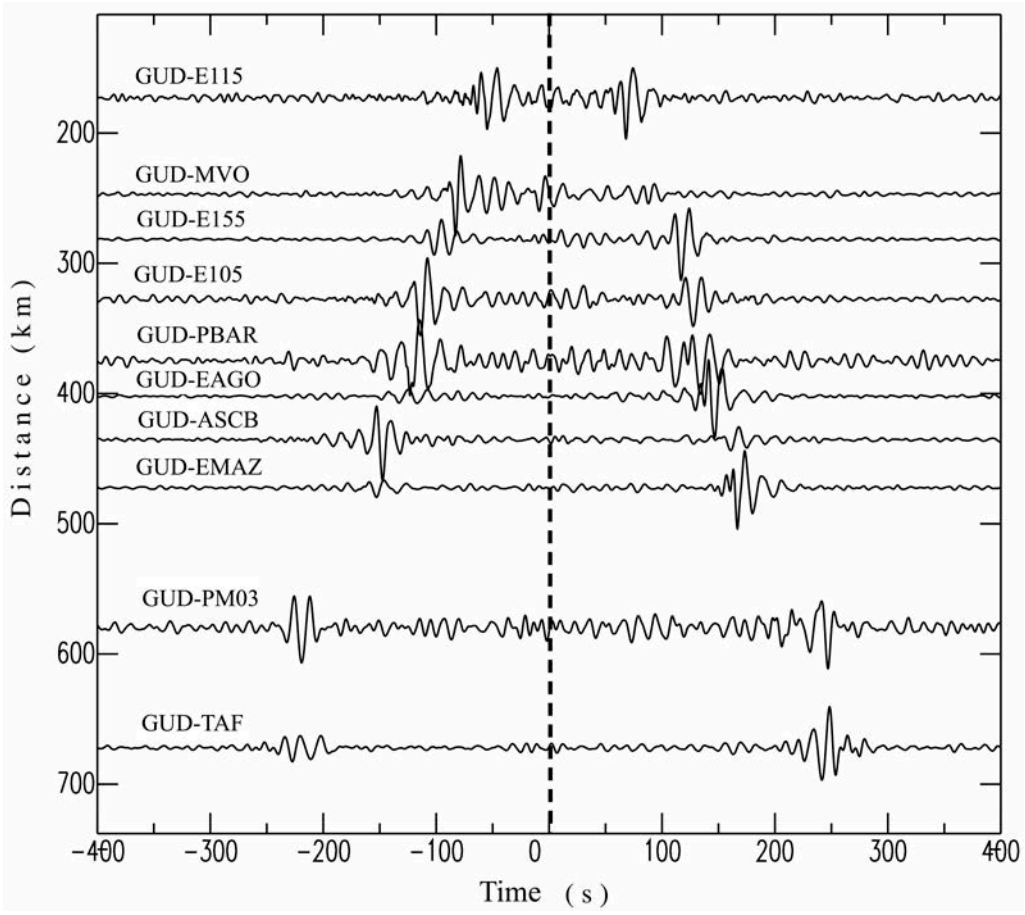

Figure 2.10: Vertical cross-correlations between different station-pairs having GUD as a center station bandpassed between 10-20 s period plotted as a function of interstation distance.

We averaged causal and acausal lag components to obtain symmetric EGFs. Because the time-series length (number of days that have been stacked) is different for each EGF, we first applied a normalization by dividing the symmetric EFG by the squared RMS amplitude of the trailing noise. The trailing noise was selected in a time window between 1500 and 2500 s which can be already considered incoherent noise. Rayleigh wave amplitudes of the corrected EGF were measured between 5 and 25 s periods performing frequency-time-analysis (FTAN) [*Levshin et al.,* 1992]. At each period, only those EGF amplitudes with interstation distances greater than three wavelengths and period-dependent SNR >10 [*Bensen et al*., 2007] were kept. Moreover, the dispersion curves of several center stations were visually inspected to assess the accuracy of the amplitude decays measured. Accepted Rayleigh wave amplitudes were corrected for the geometrical spreading by multiplying the amplitude by $r^{-1/2}$ where r is the interstation distance. Figure 2.11 shows the process carried out to perform the time-series length correction to final estimate the EGF amplitudes.

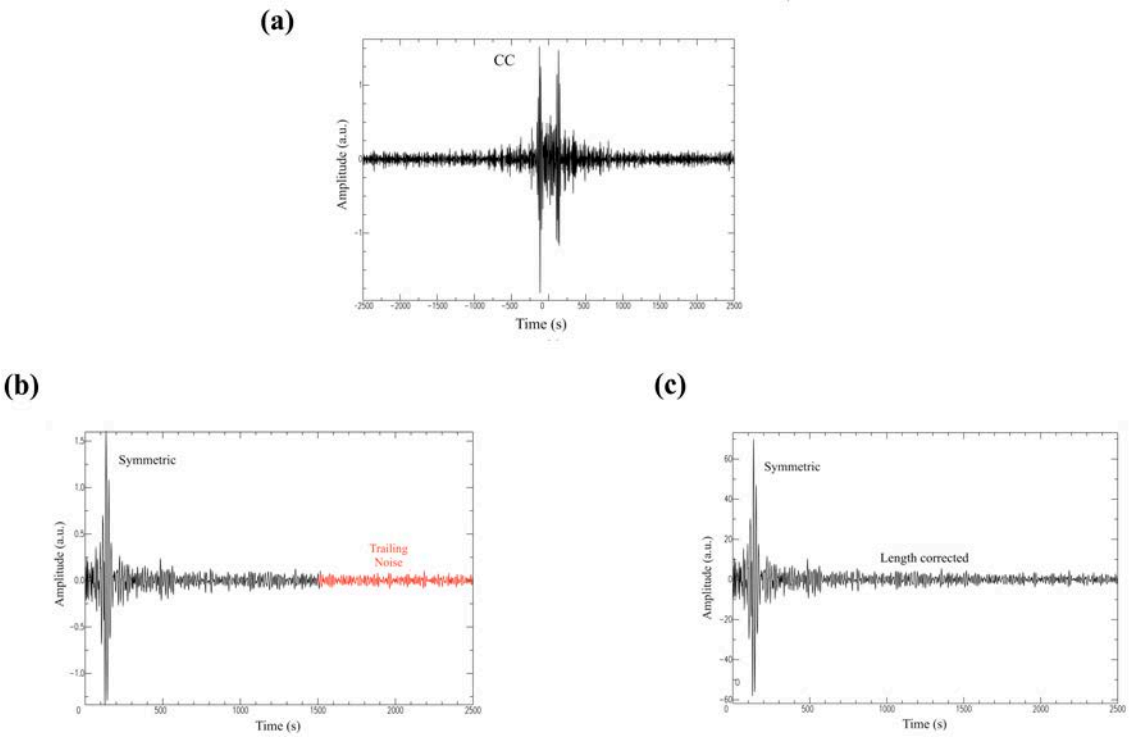

Figure 2.11: (a) Vertical cross-correlation (CC) filtered between 10-20 s. (b) The symmetric component of the CC also filtered between 10-20 s. The trailing noise used to perform the time-series length correction is colored in red. (c) The symmetric EGF corrected for time series length. a.u., arbitrary units.

Finally, amplitudes were also corrected for azimuthal variations to reduce the scattering caused by the strong azimuthal dependence of the incoming energy flux of the waves. In order to compute the azimuthal correction, we modeled the amplitude *A* of a wave that propagates in a homogeneous attenuative medium generated by an impulsive force as $A = r^{-1/2} e^{-\pi f r / \beta Q}$. Thus taking natural logarithms, amplitudes were plotted versus distance so that Q^{-1} could be estimated from the slope of the linear regression fitting. We introduced a new variable called amplitude factor (AF) as the ratio between the measured amplitude and the fit lines (Figure 2.12). Then, we applied the azimuthal correction by dividing amplitudes corrected for time-series length and geometrical spreading by their corresponding azimuthally averaged AF. The azimuthally averaged AF was calculated from the weighted average of all the AF within each 8º azimuthal window using a Gaussian weight with 2º half width. Figure 2.12 presents EGF amplitudes corrected for geometrical spreading and time-series length (left) as well as azimuth variations (right) versus interstation distance at 10 s period. We can observe a significant decrease of the scattering in the amplitude measurements when azimuthal corrections are performed.

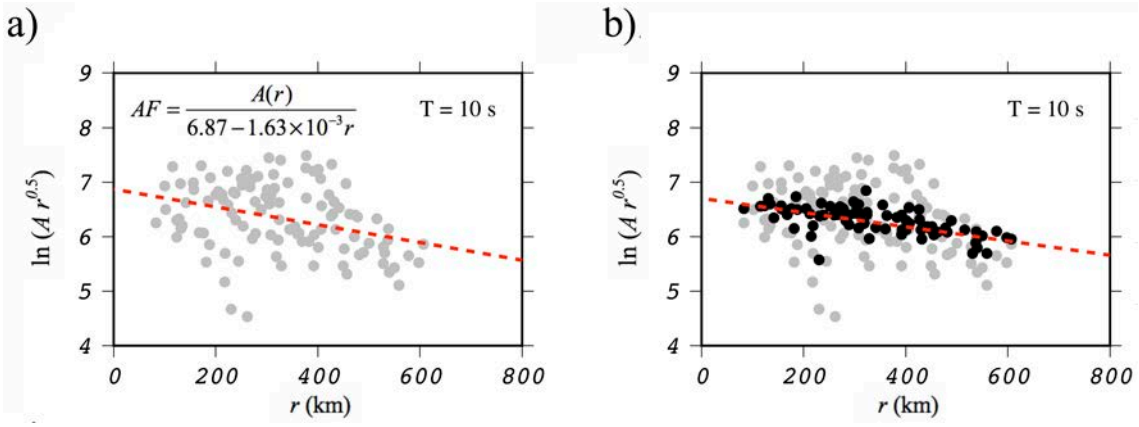

Figure 2.12: (a) Symmetric EGF amplitudes corrected for geometrical spreading and time-series length versus distance at 10 s period. AF estimated from the fit line is also indicated. (b) Symmetric EGF amplitudes corrected for geometrical spreading and time-series length (grey dots) as well as azimuthal variations (black dots) versus distance at 10 s period. Straight lines represent the best fit for distances up to 800 km.

3. RESULTS

Various approaches have been implemented in this thesis to determine the seismic attenuation in the IMR. For the estimation of *Q*, three methods were performed: the two-station method, the coda normalization method, and the spectral amplitude decay method. With the development of ambient noise, noise studies were also incorporated in this thesis to investigate the attenuation structure of the IMR.

Attenuation has been studied using amplitude measurements of surface waves (Rayleigh waves) and regional phases (*Lg* waves) in both frequency and time domain. From all the methods applied, only the TS method allows us to image the lateral variations of the *Lg Q* that can be correlated with regional structures. Conversely, averaged *Q* estimates over larger regions and frequency-dependent functions were given by CN and SAD approaches and noise derived methods. The TS method requires strict source–station configuration and dense event and station coverage that can only be found for the Iberian Peninsula in our study. Across Morocco, the low seismicity of some areas and the station distribution did not make it possible to implement the TS method.

This work is the first attempt at measuring Rayleigh wave attenuation from noise EGF amplitudes in the IMR. Focusing on the primary microseism (~10-20 s), we have examined the effect of the noise directionality on amplitudes and estimated amplitude decays. The behavior of azimuthally and spatially averaged Rayleigh *Q* values has also been analyzed at different frequencies throughout the IMR.

3.1. *Lg* Wave Attenuation Using Earthquake Data

As mentioned earlier, we have used the TS method for modeling *Lg* wave attenuation in the Iberian Peninsula. First, we calculated the interstation *Lg* quality factor associated with each TS path, and then performed an inversion to estimate the lateral variations of the attenuation parameters *Lg Q* and η.

To evaluate *Lg* attenuation from the TS methodology, we calculated interstation *Lg* Q_0 and η values using Equation 2.3 as in the examples of linear regression fit shown in Figure 3.1. For most stations a flattening of the spectra above 2 Hz can be noticed (Figure 3.1). As a consequence, linear regressions were fitted for the frequency band 0.5-2 Hz. The high cut-off frequency was chosen due to the significant loss of linearity observed above this value. *Fan and Lay* [2002, 2003] explained a similar observation in the Tibetan Plateau as being caused by high-frequency *Sn* coda appearing in the *Lg* window at large distances. Moreover, the influence of *Sn* coda in the *Lg* window at high frequencies when large distances are involved was also observed in the SAD method implemented in Morocco. Figure 3.2a shows that the *Lg* spectral amplitude decay changes for distances greater than 400 km at center frequencies of 5.2 Hz and 7.3 Hz. At lower frequencies (f_c=1.3 Hz) different decay rates are not observed. However, coda-normalized *Lg* spectral amplitudes (Figure 3.2b) did not show different decay rate at high frequencies due to shorter distances used.

Once interstation *Lg* Q_0 values were estimated, we resolved the lateral variation of Q_0. In order to image the spatial variations of the *Lg* wave attenuation, all the interstation *Lg* Q_0 values (Figure 2.6) were inverted using the simultaneous iterative reconstruction technique (SIRT) implemented in *Carcolé* [2006]. Main stages of the inversion processing are summarized as follows. The study region is divided into a regular grid of dimensions 0.25° × 0.25°. Then, the attenuation measured over the *i*th path can be expressed as the sum of the attenuation of the individual cells the path intersects. Moreover, one cell will be crossed by several paths that correspond to different values of *Lg* Q_0. Then, the observational equation can be expressed as:

$$\Delta_i Q_i^{-1} = \sum_{j=1}^{N} w_{ij} Q_j^{-1}, \quad i = 1,\ldots, M \tag{3.1}$$

where Δ_i and Q_i^{-1} are the distance and Q_0^{-1} along the *i*th path respectively and, w_{ij} is the length of the *i*th path into the *j*th cell and Q_j^{-1} is the Q_0^{-1} value inside the *j*th cell to be inverted for. *N* is the number of cells and *M* is the number of equations. Equation 3.1 is solved using SIRT which

is a sequential algorithm that converges toward a least-squares solution after rescaling the original equation to be solved. To use this method, it is necessary to make an arbitrary initial guess of the solution [e.g. *Wéber*, 2000]. In this work, we assigned the average *Q* value given by Mitchell et al. [2008] for the Iberian Peninsula. Finally, a root mean square error ε between the current and last solution at each iteration step of $\varepsilon \leq 10^{-5}$ is selected as threshold to stop the iterative method.

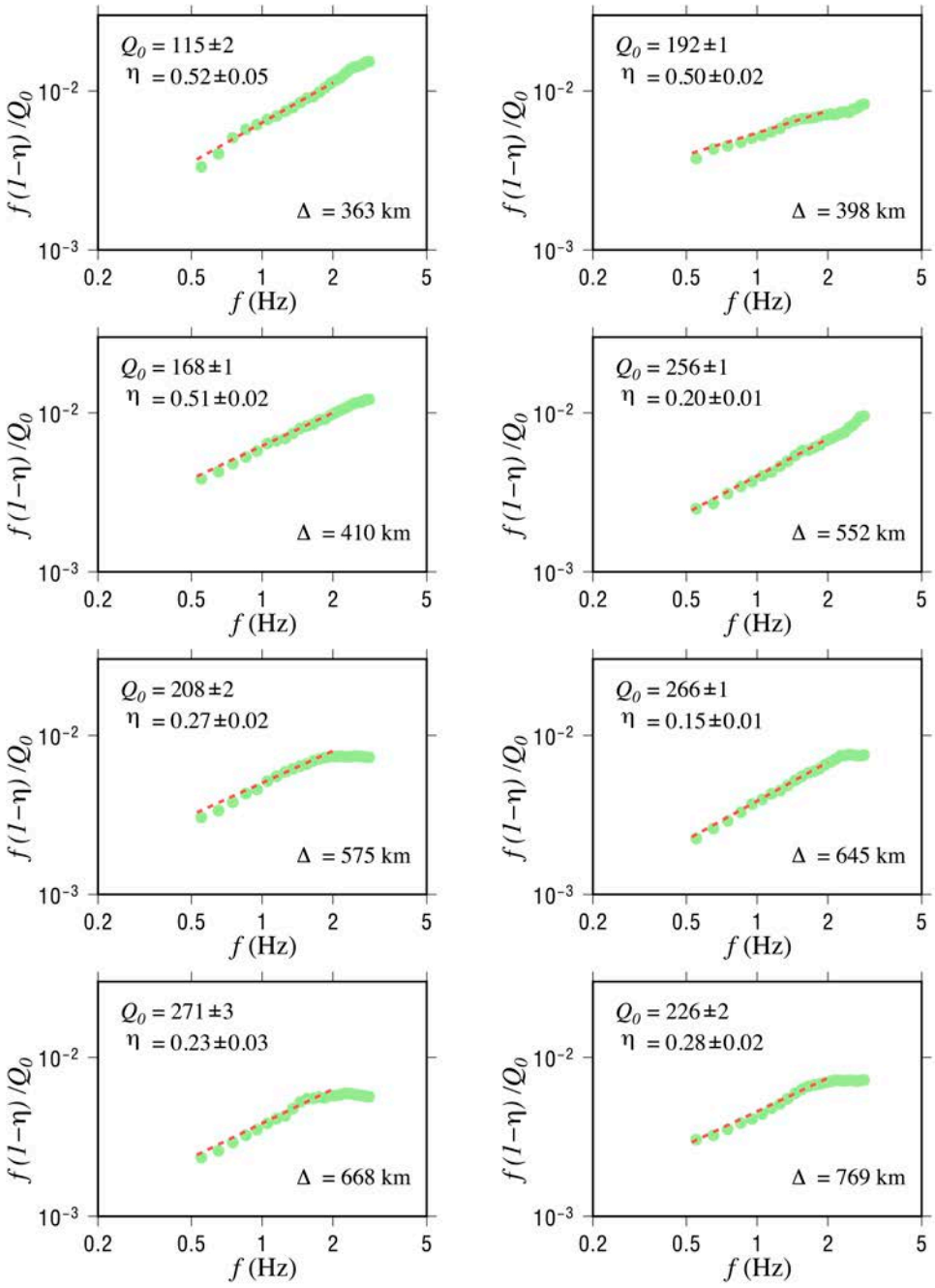

Figure 3.1: Examples of the linear regression fit for the frequency band 0.5-2 Hz performed to determine *Lg* Q_0 and η values and their standard errors.

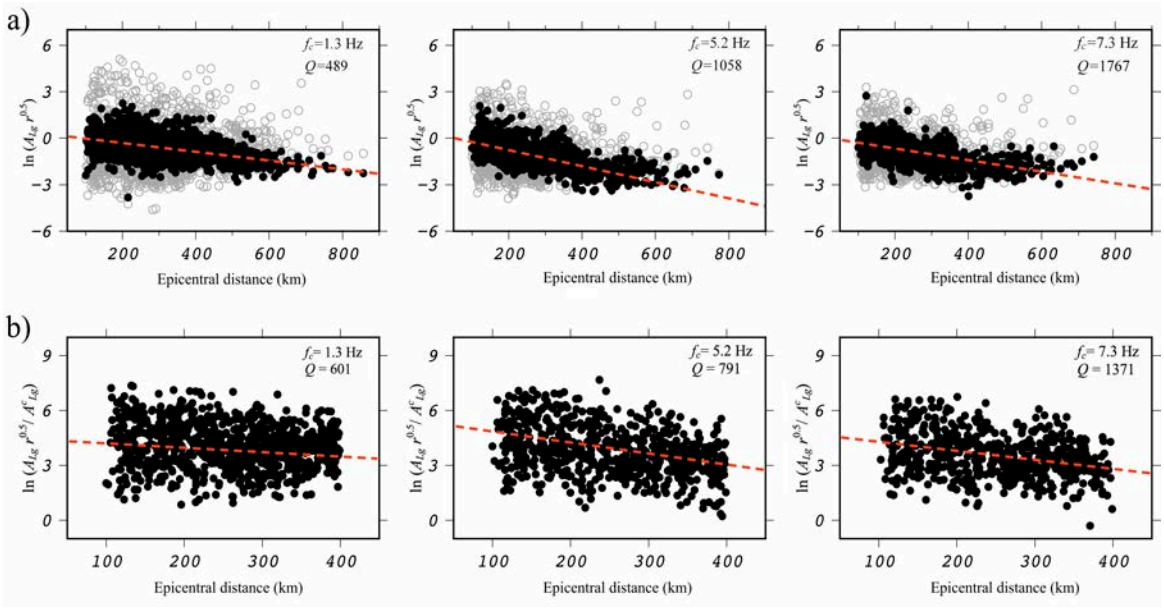

Figure 3.2: (a) Observed *Lg*-wave spectral amplitude corrected for geometrical spreading (grey circles) and corrected for source and site terms (black dots) against hypocentral distances. These corrected amplitudes have been calculated using the SAD method. (b) Coda-normalized *Lg* spectral amplitudes corrected for geometrical spreading versus hypocentral distances. They were estimated by the CN approach. Both (a) and (b) were measured at frequencies of 1.3, 5.2, and 7.3 Hz. Straight lines represent the best fit for the three of the analyzed center frequencies.

The reliability of the solution may be affected by poor sampling in some cells of the grid. To check how adequate the entire region is sampled, we calculated the number of times each cell is crossed by the TS paths or hit count. Figure 3.3 shows that the Iberian Peninsula is well sampled.

The resolution of the inversion algorithm was also tested before resolving the lateral variations of *Lg* Q_0. To do so, we used a synthetic distribution of the attenuation parameters, with the same event and station configuration used in this study. We constructed a checkerboard pattern with 2.5° × 2.5° alternating high-attenuation (Q_0 = 10) and low-attenuation (Q_0 = 1000) cells (Figure 3.4a). The synthetic model was then inverted using SIRT. Figure 3.4b shows that the attenuation structures are reasonably well resolved from the inversion.

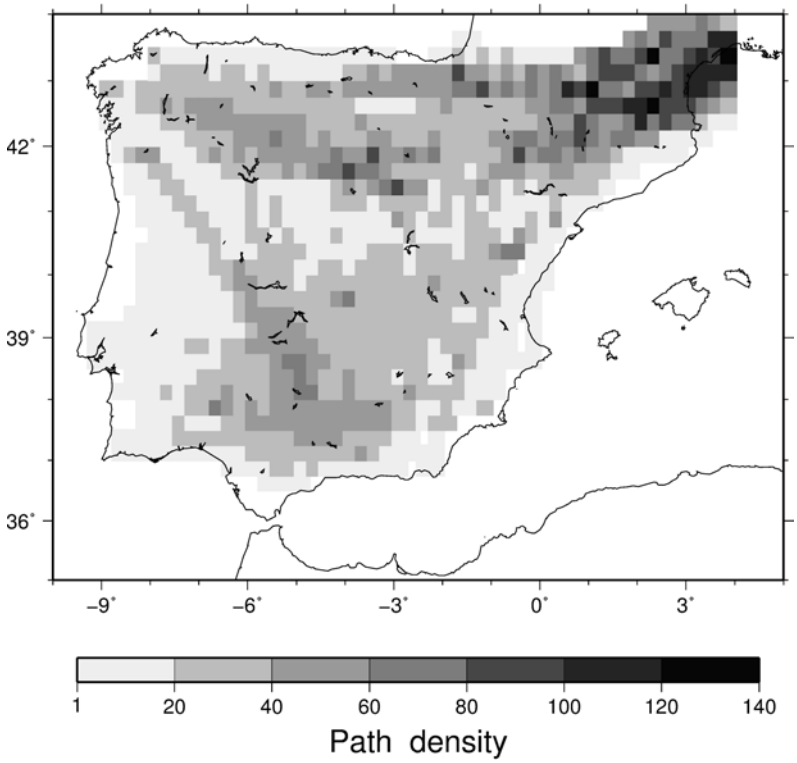

Figure 3.3: Hit counts for the Iberia Peninsula region. The darker areas are the more sampled zones.

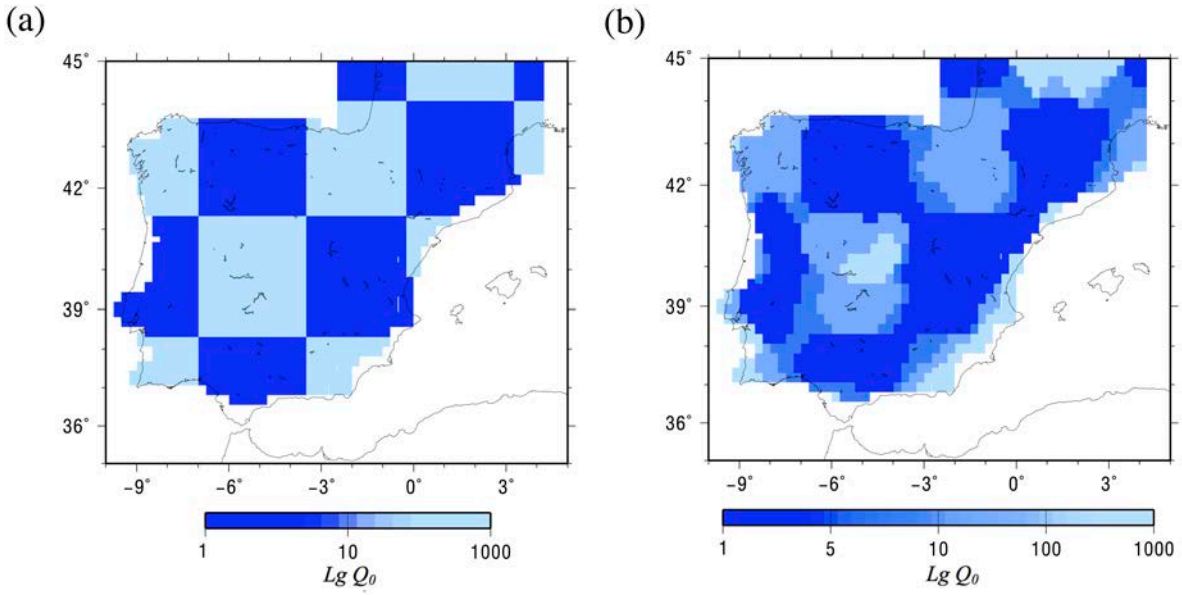

Figure 3.4: (a) Checkerboard synthetic test model and (b) obtained spatial variation of the synthetic attenuation model using the SIRT algorithm.

Once the resolution of the inversion method was determined, we performed the inversion for the actual interstation *Lg* Q_0 values. Figure 3.5 shows the lateral variations of *Lg* Q_0 in the Iberian Peninsula and Figure 3.6 its standard deviation. The standard deviation was estimated by resampling the original dataset using the delete-*j* jackknife technique [e.g. *Erickson et al.*, 2004]. We removed $\sqrt{n}$ randomly selected observations from the original *n* number of Q_0 measures to create 1000 jackknife datasets. Subsequently, each dataset was inverted to estimate 1000 new models, from which the mean and standard deviation of *Lg* Q_0 is calculated.

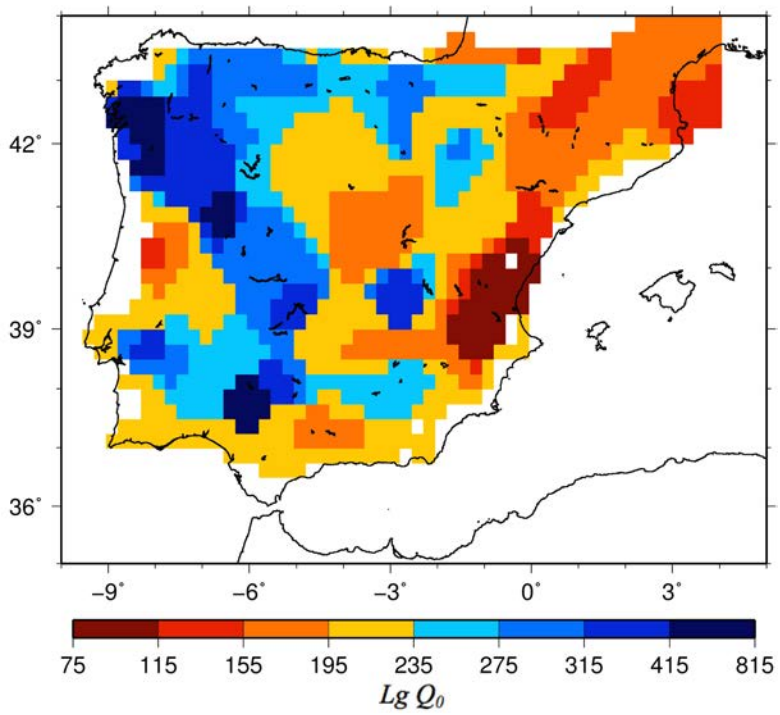

Figure 3.5: Lateral variations of *Lg* Q_0 in the Iberian Peninsula. Lower Q_0 values represent zones with higher attenuation.

We also attempted to image the lateral variation of the frequency dependence exponent η. According to *Xie et al.* (2004) a wide frequency range should be desirable to obtain stable measurements of η. Being aware of this limitation, we obtained the spatial variations of η using another procedure. For each cell of the grid, we mapped the maximum η value of all the trajectories that cross that cell. Only the cells crossed by more than 5 paths were kept. By using the maximum η value to map the spatial variations of the frequency dependence exponent, we are removing the effect of TS paths for which the η obtained is unrealistically low (e.g., *McNamara and Walter*, 2001] that could be caused by the limited frequency range used to compute η. The resulting map is plotted in Figure 3.7. In this study, we did not observe a

consistent pattern of η with high or low Q_0 measurements. Therefore, we did not obtain reliable η results.

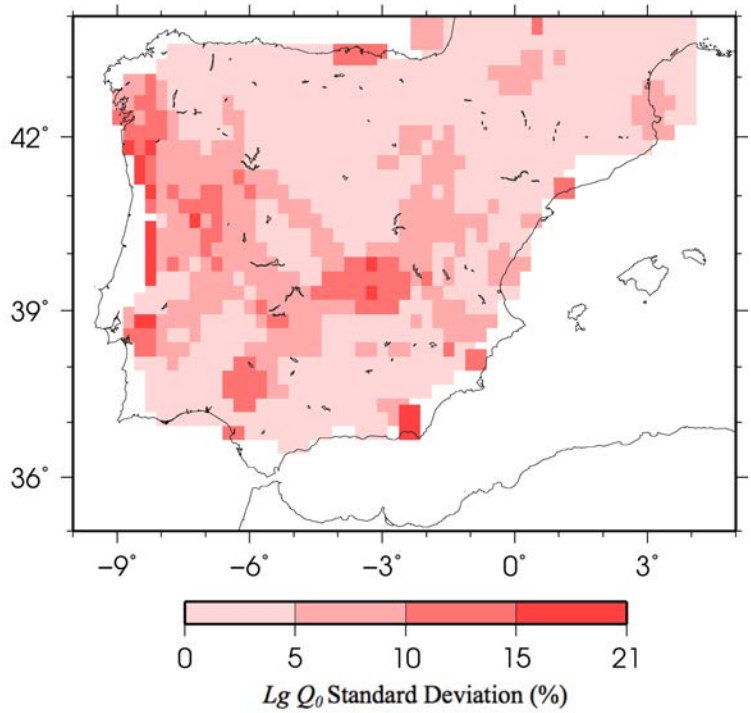

Figure 3.6: Standard deviation of $Lg\ Q_0$ estimated using a delete-*j* jackknife resampling technique in the Iberian Peninsula.

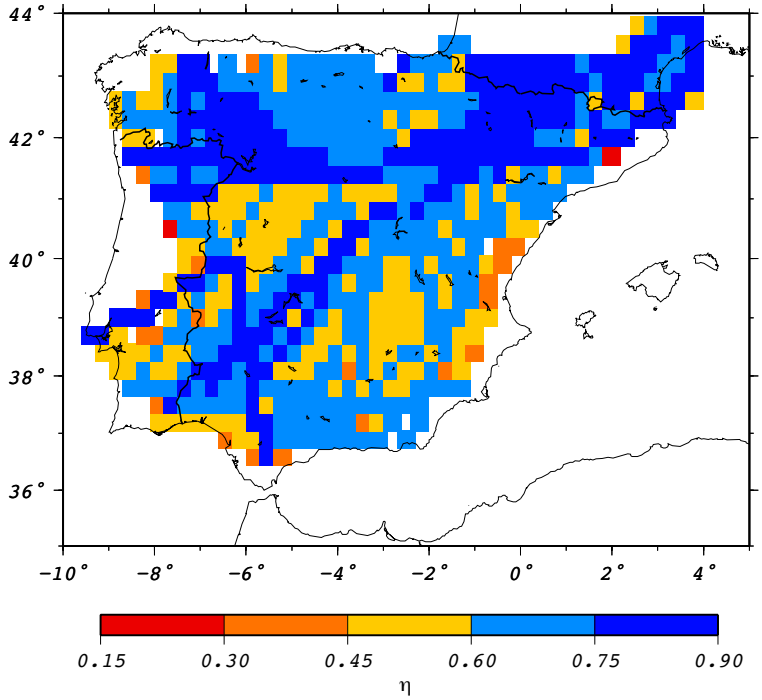

Figure 3.7. Lateral variation of maximum η values.

For the estimation of the frequency-dependent *Lg*-wave attenuation in Morocco, we first implemented the CN method using hypocentral distances $\Delta \leq 400$ km. Later, we computed the SAD method for data with $\Delta \leq 400$ km to be comparable with the CN method, and later using the complete data set ($\Delta \leq 900$ km). To estimate *Lg* attenuation by means of the CN approach, Equation 2.7 is resolved in each frequency band (every ¼ octave between 0.9 and 7.3 Hz center frequencies) by means of a linear regression combining waveforms of several events recorded at different stations. The slope of the linear regression is related to Q^{-1}. Figure 3.8 plots the left-hand side of Equation 2.7 against epicentral distances together with the best fit line for all the frequency bands analyzed.

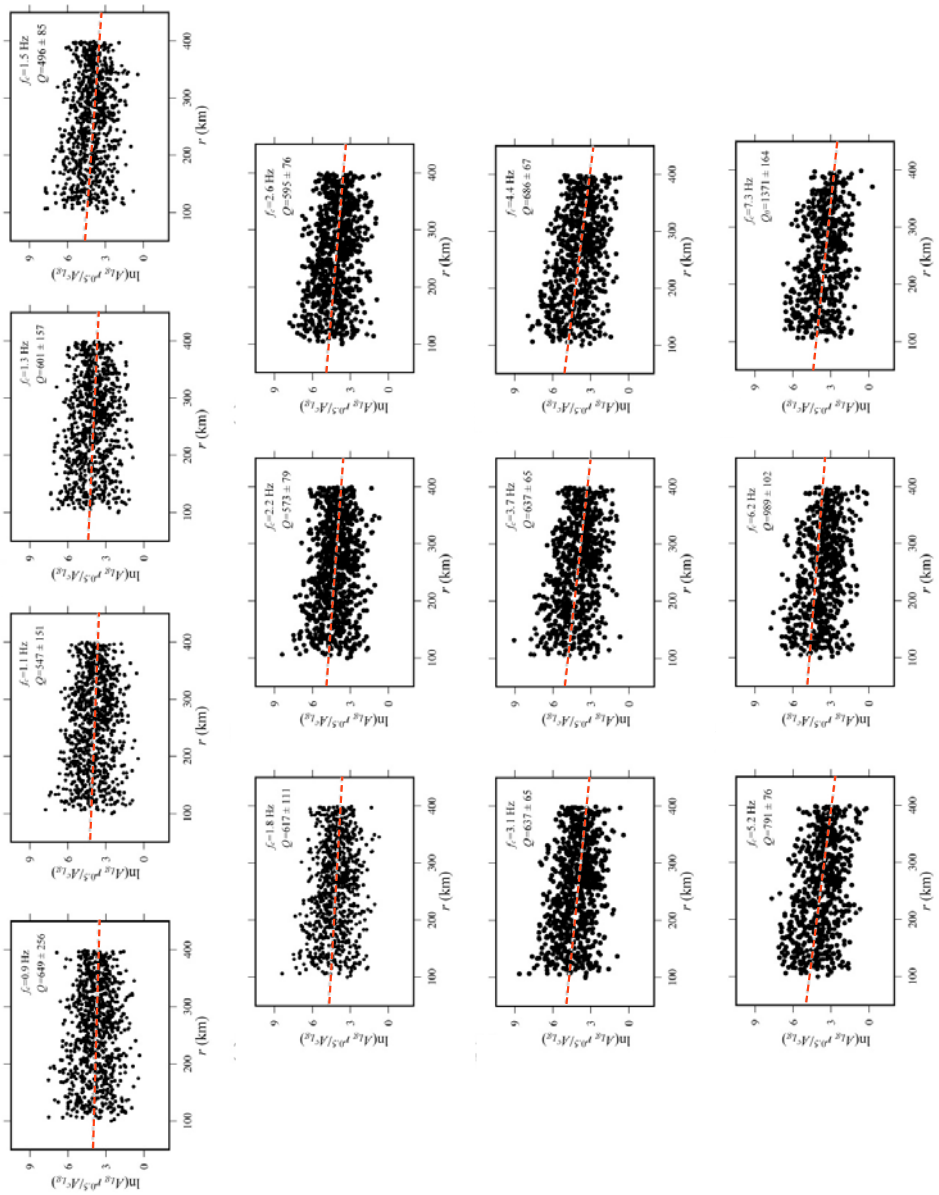

Figure 3.8: *Lg*-wave to coda amplitude ratio corrected for geometrical spreading versus hypocentral distance measured at every quarter octave between 0.9 and 7.3 Hz center frequencies.

Estimations of *Lg Q* from SAD method were carried out using both the complete data set ($\Delta \leq$ 900 km) and for distances up to 400 km. Spectral amplitudes measured from the original *Lg* waveforms were then, used to resolve Equation 2.10. Figure 3.9 shows original *Lg* spectral amplitudes corrected for geometrical spreading together with spectral amplitudes corrected by the source and receiver terms determined from the inversion at all frequency bands analyzed. The straight line represents the best fit for a distance range of 100–900 km. Also in this case, the standard deviation of *Q* was estimated by resampling the original dataset using the delete-j jackknife technique.

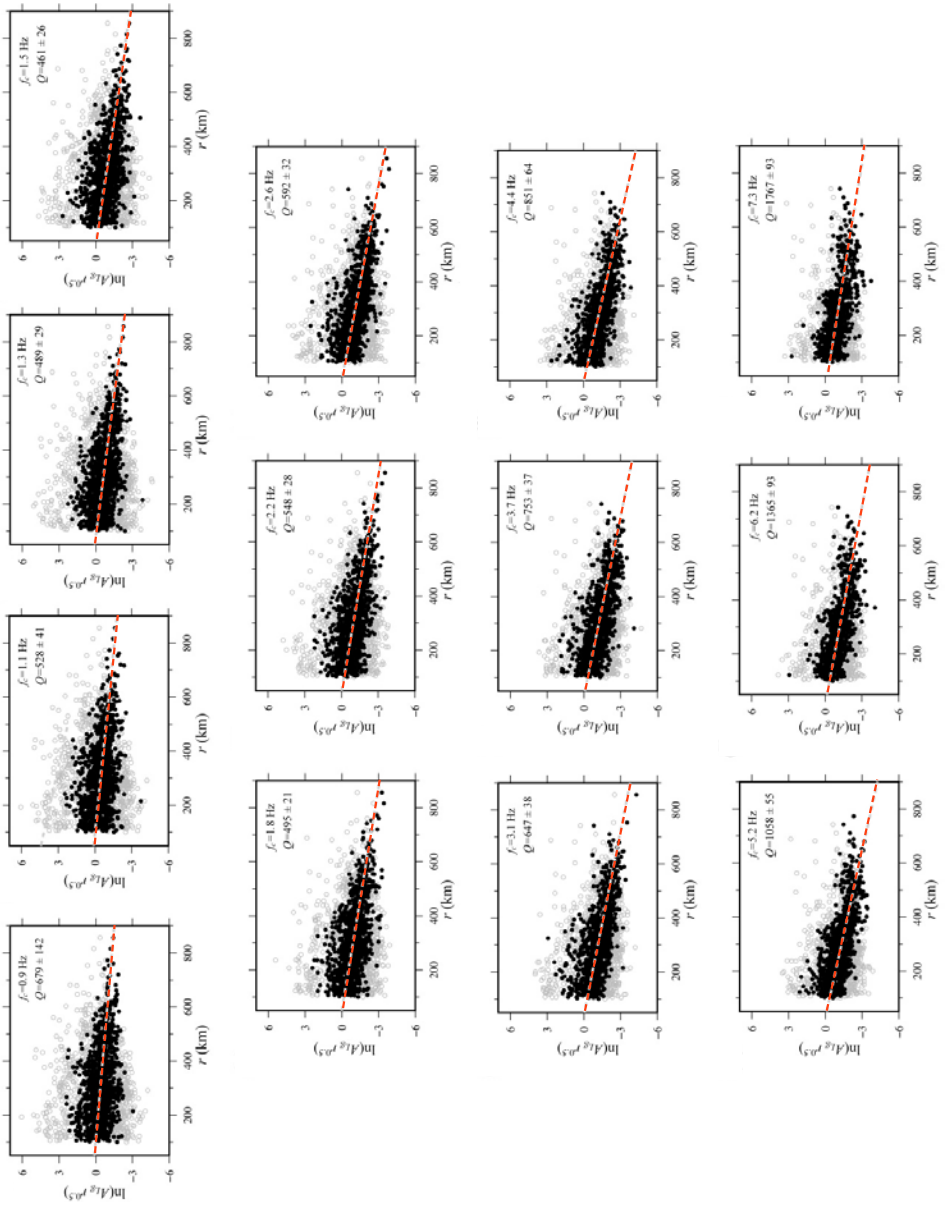

Figure 3.9: *Lg*-wave amplitude corrected for geometrical spreading (grey circles) and corrected from source and site terms (black dots) versus hypocentral distance measured at every quarter octave between 0.9 and 7.3 Hz center frequencies.

For the frequency band between 0.9 and 7.3 Hz center frequencies, average *Lg Q* estimates and their standard errors are plotted in Figure 3.10 and listed in Table 3.1.

	CN		SAD (400 km)		SAD	
f_c (Hz)	Q	σ	Q	σ	Q	σ
0.9	649	+422 -183	618	+122 -87	479	+174 -107
1.1	547	+20(-118	493	+59 -48	528	+34 -30
1.3	601	+213 -124	533	+53 -45	489	+43 -37
1.5	496	+103 -73	453	+78 -58	461	+35 -30
1.8	617	+136 -94	512	+41 -35	495	+24 -22
2.2	573	+92 -70	546	+28 -26	548	+26 -24
2.6	595	+87 -67	590	+30 -27	592	+53 -45
3.1	608	+76 -61	609	+30 -27	647	+43 -38
3.7	637	+72 -59	678	+26 -24	753	+55 -48
4.4	686	+74 -61	743	+24 -22	851	+47 -43
5.2	791	+84 -69	922	+36 -33	1058	+57 -51
6.2	989	+114 -93	1091	+61 -55	1365	+70 -64
7.3	1371	+186 -146	1455	+88 -78	1767	+97 -87

Table 3.1. Average *Lg Q* values and their standard errors estimated for Morocco at 13 centre frequencies between 0.9 and 7.5 Hz estimated using: (1) the CN method for hypocentral distances less than 400 km; and (2) the SAD method using the complete data set and for distances up to 400 km. The asymmetric error bounds on *Lg Q* are derived from back transforming the formal uncertainties in the Q^{-1} estimates.

Averaged *Q* values plotted against the frequency and the asymmetric error bounds are shown in Figure 3.10.

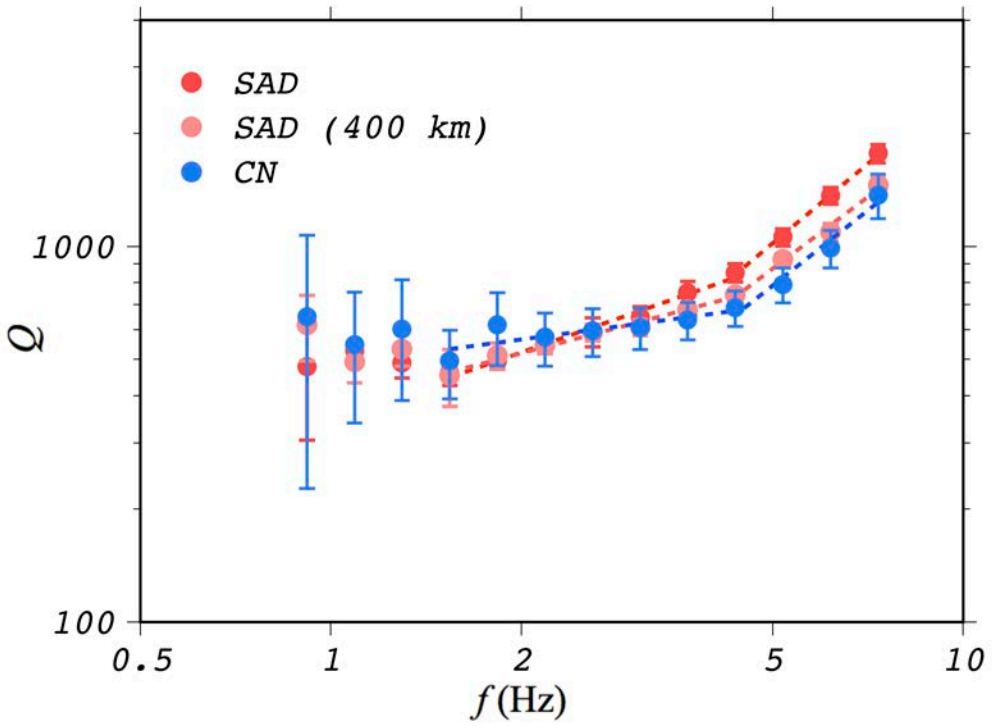

Figure 3.10: Average *Lg Q* values estimated in Morocco from coda-normalized *Lg* spectral amplitudes (blue dots) and amplitude spectral decay for the complete dataset (red dots) and up to 400 km (pink dots) together with asymmetric error bounds versus frequency. Straight lines are the linear regression fitting using Equation 1.2.

Figure 3.10 exhibits a distinct change in the frequency dependence above 4.5 Hz for both methods. *Lg Q* values were fitted to the frequency dependence function Equation 1.2. The functions obtained for the frequency bands 1.5 to 4.5 Hz were:

$$Q(f) = (529^{+23}_{-22})(f/1.5)^{0.23\pm0.06},\ 1.5 \le f \le 4.5 \text{ Hz},\ r \le 400 \text{ km (CN)}$$

$$Q(f) = (457^{+7}_{-7})(f/1.5)^{0.44\pm0.02},\ 1.5 \le f \le 4.5 \text{ Hz},\ r \le 400 \text{ km (SAD)}$$

$$Q(f) = (444^{+8}_{-8})(f/1.5)^{0.59\pm0.03},\ 1.5 \le f \le 4.5 \text{ Hz},\ r \le 900 \text{ km (SAD)}$$

Whereas those functions for the frequency band 4.5 to 7.5 Hz are:

$$Q(f) = (684^{+35}_{-33})(f/4.5)^{1.33\pm0.17},\ 4.5 \le f \le 7.3 \text{ Hz},\ r \le 400 \text{ km (CN)}$$

$$Q(f) = (765^{+22}_{-22})(f/4.5)^{1.26\pm0.10},\ 4.5 \le f \le 7.3 \text{ Hz},\ r \le 400 \text{ km (SAD)}$$

$$Q(f) = (879^{+2}_{-5})(f/4.5)^{1.41\pm0.03},\ 4.5 \le f \le 7.3 \text{ Hz},\ r \le 900 \text{ km (SAD)}$$

The asymmetric error bounds on Q_0 are derived from transforming back the uncertainties obtained for ln Q_0 through the linearization of Equation 1.2

3.1.1. *Lg* Wave Blockage in the IMR

We have also studied *Lg* propagation efficiency throughout the entire IMR. Previous works have established an efficient propagation of *Lg* over stable continental regions [e.g. *Mitchell et al.*, 1997; *McNamara and Walter*, 2001]. Therefore, a similar behavior would be expected for *Lg* in continental raypaths crossing the Iberian Peninsula and Morocco. Figure 3.11 shows examples of vertical-component waveforms bandpass filtered between 0.5 and 5 Hz for some paths across different tectonic regions. All these seismograms show strong *Lg* energy in a window defined by group velocities from 3.5 to 2.9 km/s. Figure 3.11a presents raypaths travelling across eastern Iberia related to more active areas. Paths crossing the central and western part of Iberia, which are characterized by more stable crust, are displayed in Figure 3.11b. Figure 3.11c shows raypaths crossing northern Morocco.

As was expected, we obtain that *Lg* propagation is efficient across the continental crust of the Iberian Peninsula and Morocco.

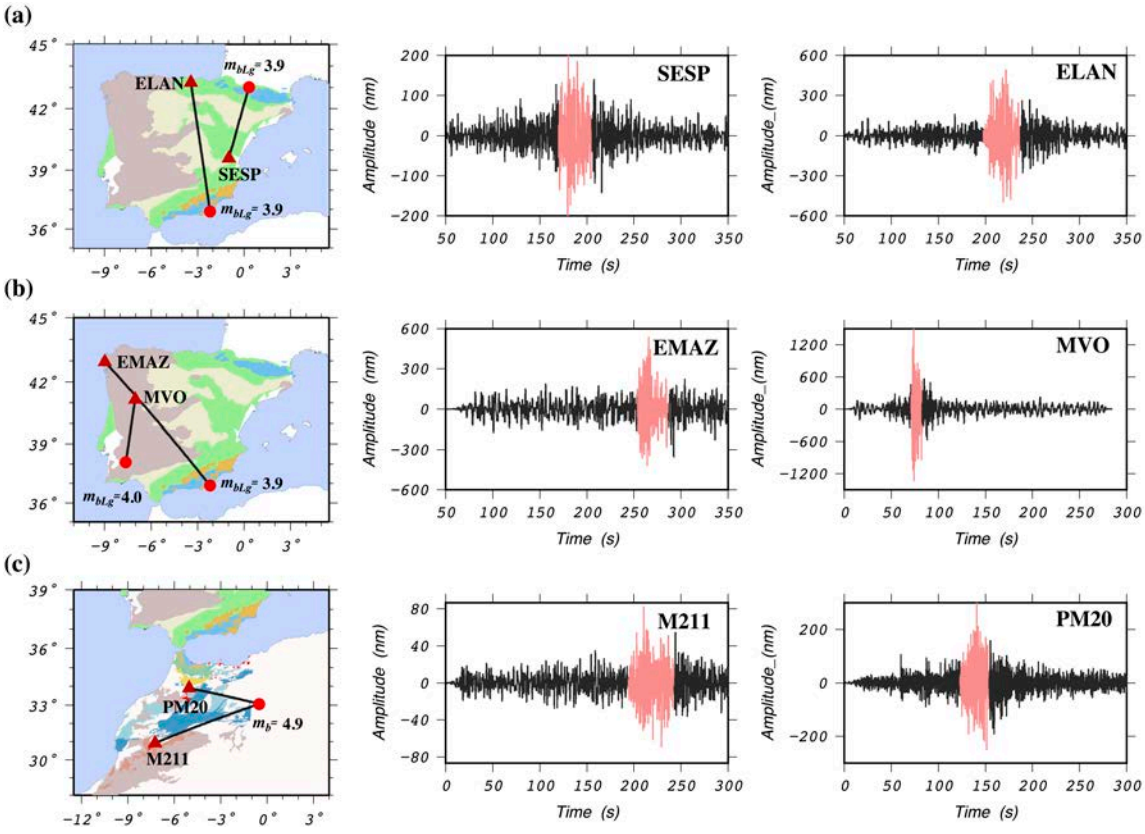

Figure 3.11: Major tectonic features of the IMR and events and stations location maps used in this study. Examples of waveforms bandpass filtered (0.5-5 Hz) along different propagation paths: (a) SESP and ELAN, (b) EMAZ and MVO, and (c) M211 and PM20. The *Lg* energy in a velocity window 3.5-2.9 km/s is highlighted in pink. The vertical scale is fixed to the peak amplitude for each seismogram.

Figure 3.12 shows band-pass filtered waveforms (0.5-5 Hz) for paths crossing the continental-oceanic transition zones of the IMR. Weak *Lg* phase is recorded in these seismograms. Evidence of inefficient or blockage *Lg* propagation is observed for paths crossing the Strait of Gibraltar (Figure 3.12a) and the Alborán sea (Figure 3.12b). Such *Lg* characteristics for paths crossing the Alborán basin were already noticed by *Calvert et al.* [2000] and *McNamara and Walter* [2001]. *Calvert et al.* [2000] carried out a study of regional seismic phases (*Lg* and *Sn*) propagation along the African–Iberian plate boundary and demonstrated that *Lg* propagation is usually inefficient (*Lg* amplitude on the order of the *Pg* arrival) or even blocked (*Lg/Pg* ratio <1.0) for paths crossing the western Alborán basin and eastern Iberia beneath the Mediterranean Sea. Moreover, sharp changes in crustal thickness or paths across oceanic crust result in inefficient the *Lg* wave propagation [e.g. *Sandoval et al*., 2001].

Also inefficient *Lg* is observed in Figure 3.12c for the raypath travelling along the Mediterranean Sea.

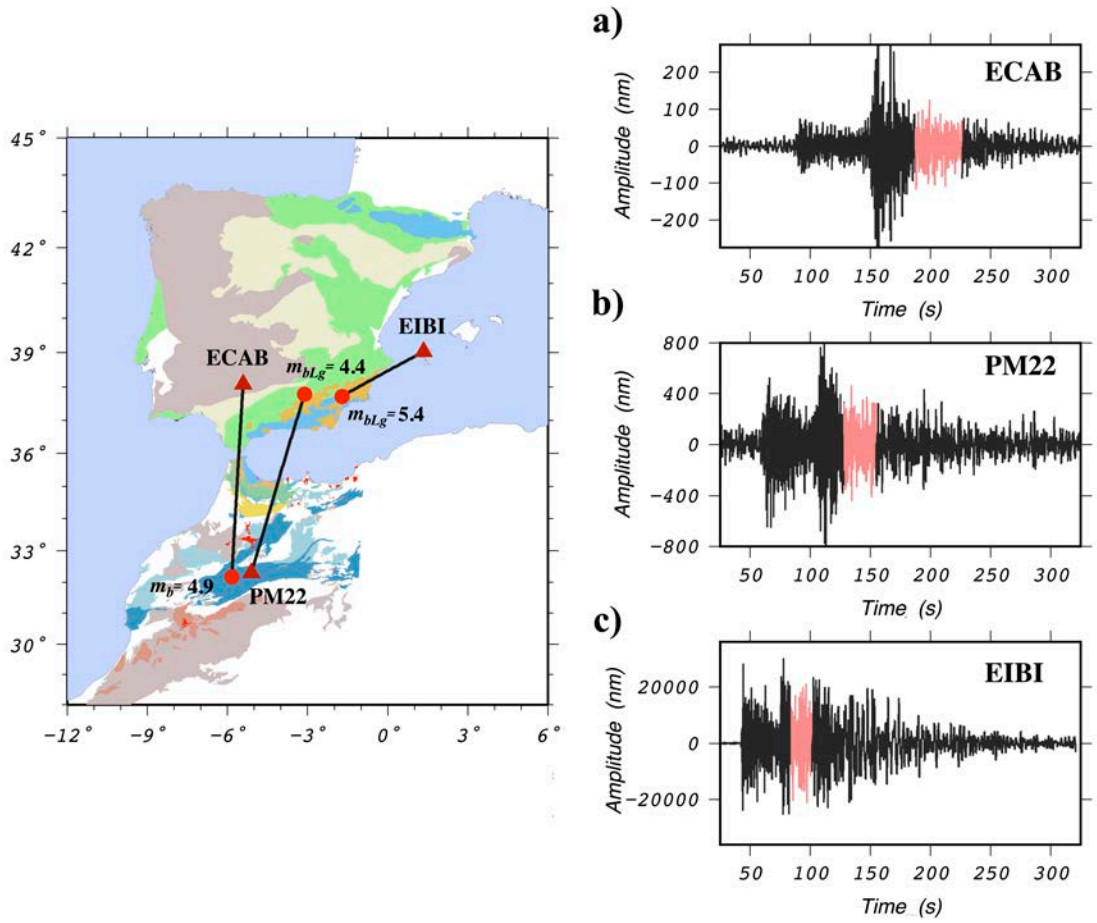

Figure 3.12: Major tectonic features of the IMR and examples of event and station locations maps. Examples of waveforms bandpass filtered (0.5-5 Hz) along different propagation paths: (a) ECAB, (b) PM22, and (c) EIBI. *Lg* energy in a velocity window 3.5-2.9 km/s is highlighted in pink.

Summarizing, Figure 3.11 presents paths for which a strong *Lg* phase is observed whereas Figure 3.12 shows raypaths for which *Lg* phase is inefficient or blocked. We have found that most of the *Lg* paths from earthquakes that occurred in northern Africa, and were recorded by stations in the Iberian Peninsula, became blocked or inefficient. In the same way, paths from events in Iberia that were recorded by seismic stations in northern Africa did not show efficient *Lg* recordings. For these reasons, the *Lg* attenuation of the Iberia and Morocco has been studied separately. In addition, we have observed the blockage of *Lg* phases in recordings at stations located in the Balearic Islands.

3.1.2. Errors Associated with *Lg* Q_0 Measurements

The Q_0 model of Iberia obtained from direct *Lg* waves is subject to different sources of errors. Errors related to the inversion were evaluated by means of the standard deviation of Q_0. This standard deviation was less than 21% throughout the entire region (see Figure 3.6).

As has been explained in the methodology, the TS method allows removing azimuthal effect of the source radiation pattern by measuring amplitudes at two stations aligned with a common source. To check the accuracy of the ±15° source-to-station azimuth constraint, we have repeated the analysis for a $\delta\theta_{max}$ value of ±8°. The number of TS paths was reduced by 46% as it can be noticed in Figure 3.13a. The inversion process was still possible and similar results (Figure 3.13b) as those showed in Figure 3.5 were obtained for the *Lg* Q_0 model of the Iberian Peninsula. The spatial variations of *Lg* Q_0 for $\delta\theta_{max}$= ±8° are mapped in Figure 3.13.

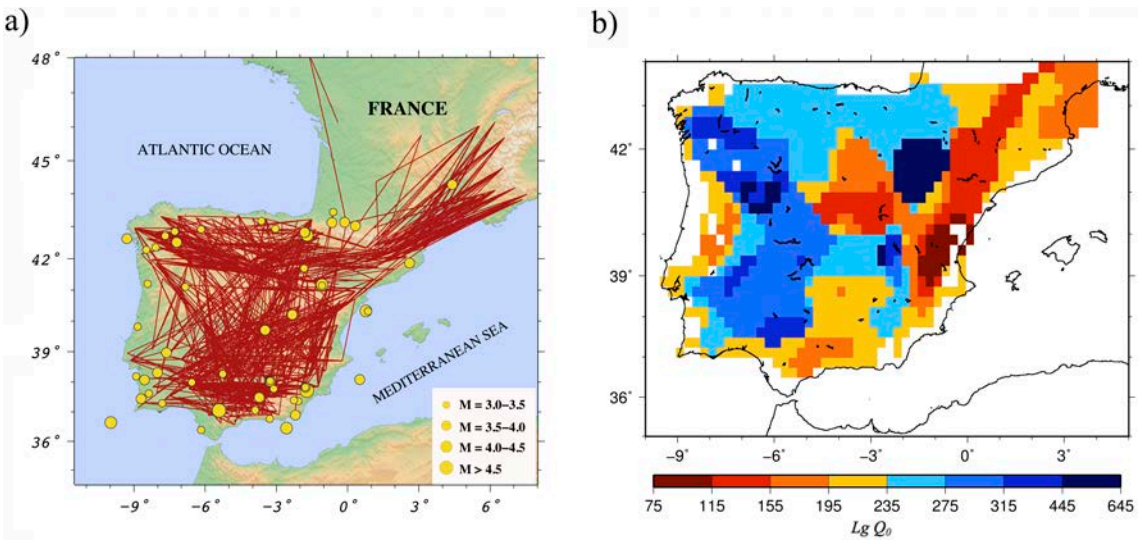

Figure 3.13: (a) TS paths and epicenters used and (b) lateral variations of *Lg* Q_0 in the Iberian Peninsula for $\delta\theta_{max}$ = ± 8°.

Nevertheless, the TS method could be still affected by other biases caused by site responses and focusing/defocusing effects. *Xie et al.* [2004] quantified such error contributions by introducing a factor of $1 \pm \delta x$. According to equation 2.4, we assumed the minimum interstation distance of 225 km to keep the error lower than 35% in this work.

To investigate possible sources of systematic errors contained in the *Lg* Q_0 estimates we have examined TS paths that correspond to an event used in this work. Figure 3.14 shows the *Lg* Q_0 values estimated from 74 TS paths for a $\delta\theta_{max}$ value of ±15° that correspond to the *Mw* 5.1 Lorca earthquake occurred on 11 May 2011. The *Lg* Q_0 values estimated for these paths are generally coherent. However, two paths located in the north-central region that have a common point at station E101, are lower than the overall trend.

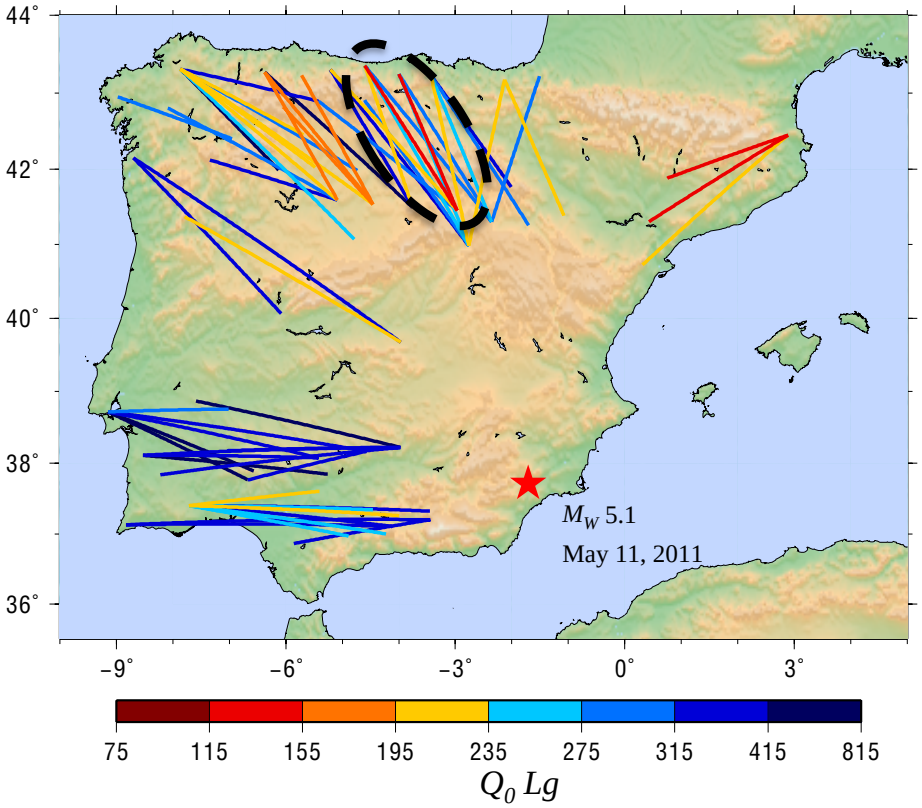

Figure 3.14: Examples of the TS paths corresponding to the M_w 5.1 Lorca Earthquake (red star). The two paths of *Lg* Q_0 values anomalously lower are indicated with a dashed black ellipse. The color palette indicates the estimated *Lg* Q_0 values for each path.

To analyze these results, we investigated the anomalous path E101-E155. We performed a comparison of the linear regression fits to calculate *Lg* Q_0 for the almost overlapping paths E101–E155 and E093–155 (shown in figure 3.15b). The spectral ratios have a similar shape, but the *Lg* amplitudes measured at station E101 are greater than those obtained for station E093 at

all frequencies. Interstation *Lg* Q_0 values estimated from the linear regression fit were Q_0=154 for E101–E155 and Q_0=337 for E093–155. In addition to the different amplitudes measured at E101 and E093, we have observed amplitude differences for other stations surrounding E101. Figure 3.15c shows site amplification at E101, which is located in Cameros Basin, with respect to other stations surrounding E101.

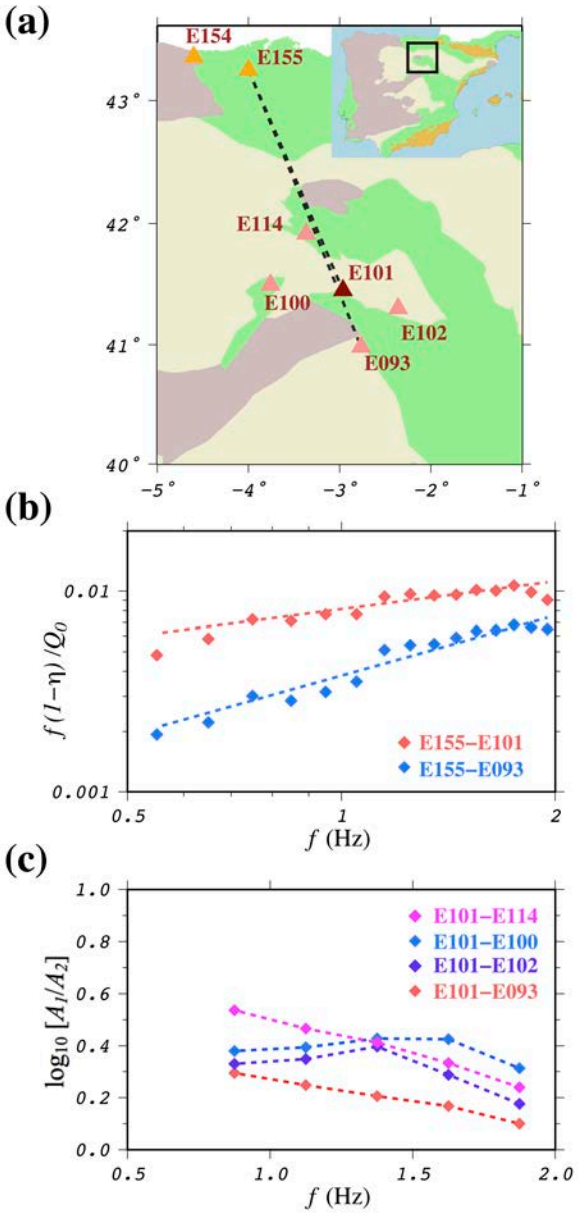

Figure 3.15: (a) Locations of the TS paths yielding different *Lg* Q_0 values (E093-E154, E101-E154, E093-E155, E101-E155) and surrounding stations (E100, E102, and E114). (b) Examples of linear regression fit performed to determine *Lg* Q_0 for paths E101-155 and E093-E155. (c) Site amplification in $\log_{10}$ (amplitude) units observed at E101 with respect to several surrounding stations.

To check for azimuthal variations in site amplification, the amplitude residuals of E101 relative to station E093 for different events plotted versus back azimuth are presented in Figure 3.16. Since no clear azimuthal dependence is observed in Figure 3.16, the possibility that the observed amplification is mainly caused by lateral focusing or defocusing effects is lower [e.g., *Barker et al.*, 1981]. These observations illustrate a possible source of systematic errors contained in the *Lg* Q_0 estimations. In this case, the geological structures under station E101 (Cameros Basin according to Figure 3.15a) are thought to be responsible for the observed site amplifications, which are not accounted for in the TS method. The station and event coverages did not allow performing the reversed TS method [*Chun et al.*, 1987] that would cancel the site response.

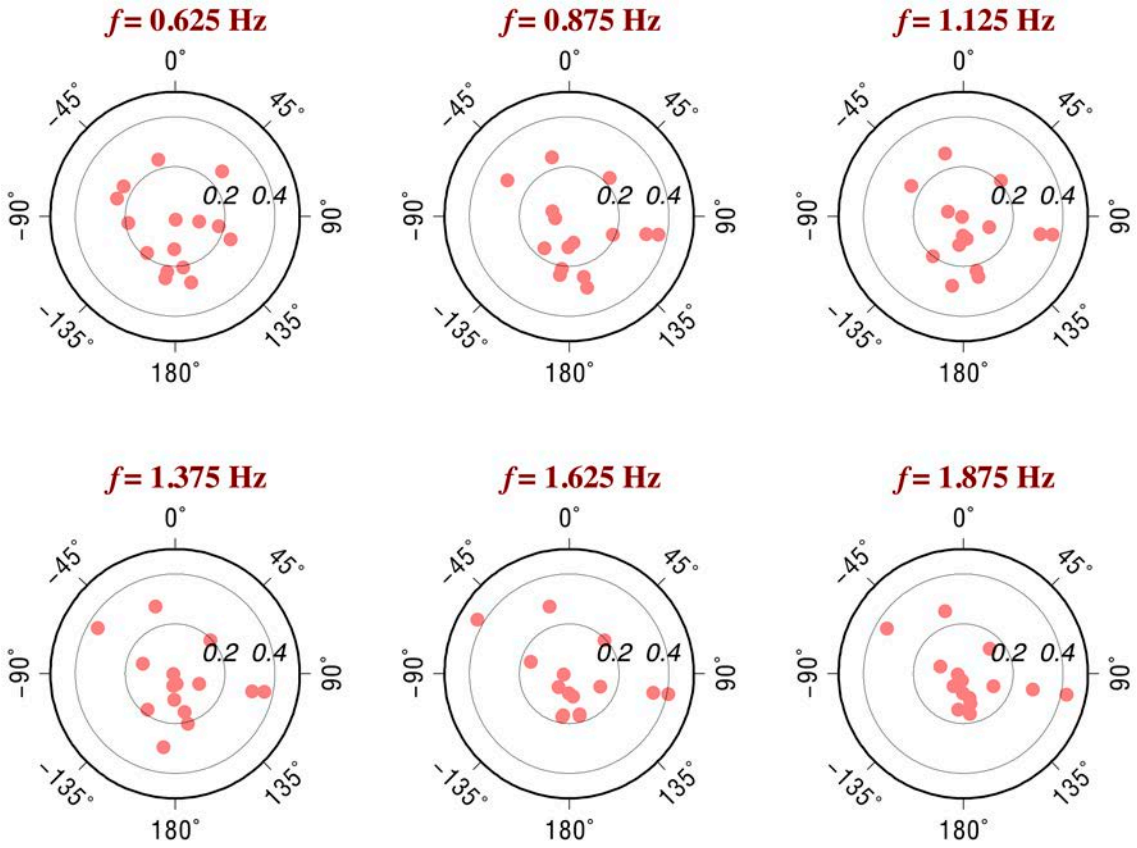

Figure 3.16: Site amplification in $\log_{10}$ (amplitude) units versus back azimuth for different frequencies observed at E101 with respect to station E093 ($\log_{10}$ [A_{101}/A_{093}]).

Although the TS method is a reliable approach, site effects may affect the *Lg* amplitudes and must be addressed in the future to improve the interpretations carried out in this thesis.

3.1.3. Source and Site Terms Estimated from SAD Method

In addition to the Q^{-1} term, site and source terms were also obtained from the inversion of Equation 2.10. The site term is related to the seismic velocity and the density of the near surface formations at the recording stations and describes possible amplification effects. Usually, site responses are strongly frequency dependent. The source term is related to earthquake magnitude. Both terms are shown in Figure 3.17.

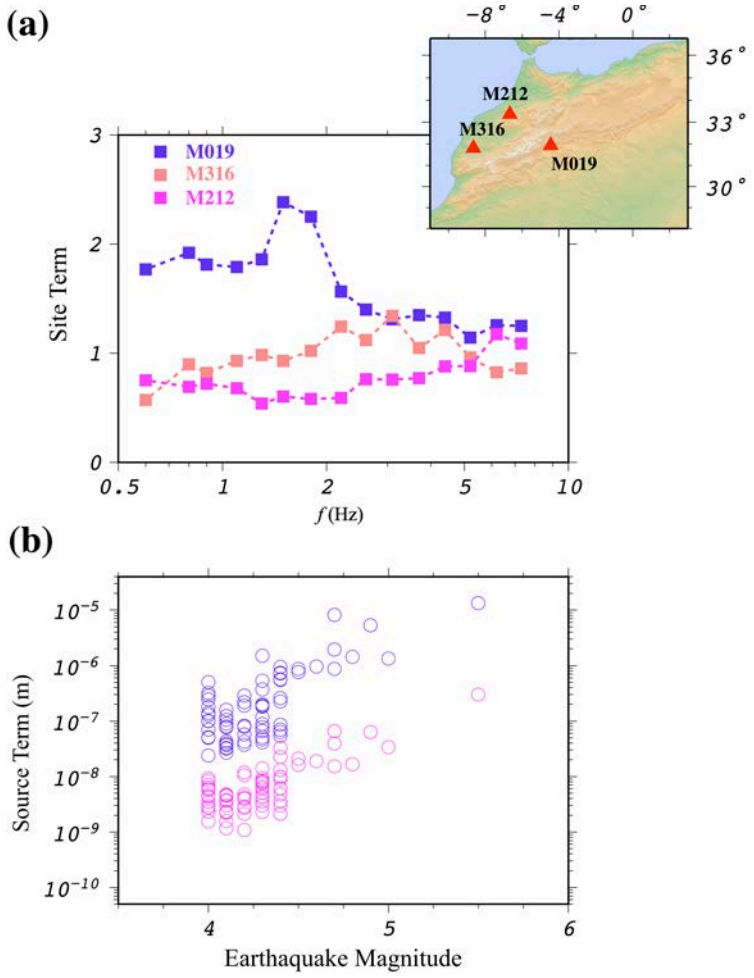

Figure 3.17: (a) Site term estimated form the *Q* inversion versus frequency for the M019, M316 and M212 seismic stations and their geographic locations; and (b) source term calculated form the *Q* inversion versus earthquake magnitude at 1.5 Hz (violet dots) and 7.3 Hz (pink dots).

Figure 3.17a shows examples of the inverted site terms for the stations M019, M212 and M316. A smooth variation with frequency is observed at most of the sites in the frequency range of 0.8–8 Hz. Stations M212 and M316 show little amplification. M212 is sited on the Zaër Hercynian granite of the western Moroccan Meseta and M316 is located at the western Palaeozoic Jebilet Massif (southwestern Moroccan Meseta). The site response corresponding to

station M019 that is located at the Errachidia Cretaceous sedimentary basin appears to be stronger [*Saadi*, 1975]. On the other hand, Figure 3.17b plots examples of the source terms obtained from the inversion at 1.5 and 7.3 Hz center frequencies versus the earthquake magnitude. Figure 3.17 shows an increase of the source terms with increasing magnitudes supporting that the source terms computed from the inversion are appropriate. Therefore, results presented in Figure 3.17 pointed out that source and site terms values seem reasonable and indicate that no serious trade-off with *Q* has occurred in the inversion process.

3.2. Rayleigh Wave Attenuation Using Ambient Noise Data

We have utilized seismic noise to analyze the attenuation structure of the IMR. We investigated the azimuthal distribution of the ambient noise in the IMR and surrounding areas to better estimate the accuracy of noise attenuation results. It must be taken into account that we can only estimate the azimuthal distribution of relative noise strength from EGF amplitudes due to the non-linear operations performed during the noise processing [e.g. *Yang and Rizwoller*, 2008]. In this work, we were not interested in describing the azimuthal variation of the seismic noise over the year (e.g. between winter and summer). Therefore, to avoid strong seasonal azimuthal dependence of the primary microseism [e.g. *Stehly et al*., 2006], we calculated the directivity of the noise over the entire recording time (~ 2 years of data). The procedure to determinate directivity of seismic noise was similar to the approach performed by *Stehly et al*. [2006].

As described in section 2.3, we applied a time-series length normalization by dividing the causal and acausal parts of the cross-correlations by the squared RMS amplitude of a noise window selected at correlation lags times between 1500 and 2500 s (Figure 3.18). Causal and acausal amplitudes of the cross-correlations corrected by time-series length were then measured between 5 and 25 s period using FTAN. Estimated amplitudes were finally corrected for the Rayleigh wave geometrical spreading by multiplying the amplitude by $r^{-1/2}$ (r being the interstation distance). To simplify, I refer the time series length and geometrical corrected amplitude simply as amplitude. Notice that for each cross-correlation, two measurements of normalized amplitude indicating the directivity of the incoming ambient noise were estimated, one for the causal and another for the acausal components of the EGF.

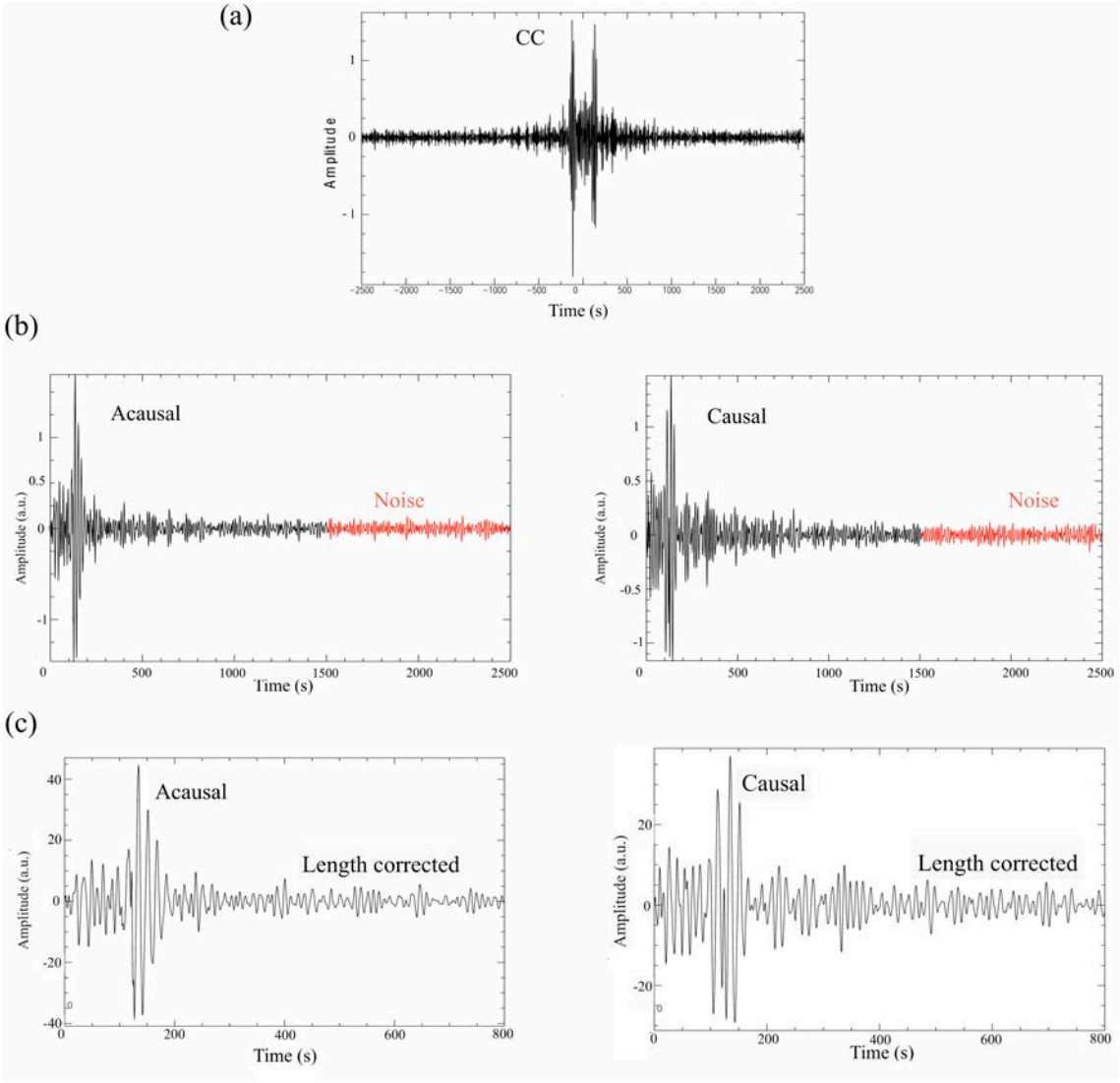

Figure 3.18: (a) An example of vertical cross-correlations band-pass filtered between 10-20 s period. (b) The acausal and causal components of the EGF. The noise at correlation lags times between 1500 and 2500 is colored in red. (c) The acausal and causal EGF corrected by the RMS of the trailing noise indicated as length corrected following *Lin et al.* [2011] terminology.

Examples of azimuthal distribution of the normalized amplitudes for several center stations covering the IMR with respect to azimuth are presented in Figure 3.19. To make comparison easier, amplitudes plotted in Figure 3.19 are normalized between 0 and 1. Rayleigh wave normalized amplitudes were estimated in the microseism band at period of 8, 12, 18 and 20 s. This figure shows higher normalized amplitude values at those periods that correspond to the primary microseism band (T=10-20 s) than at shorter periods (T=8 s) for all the center station analyzed, except for the PS01 (Cádiz) center station (Figure 3.19e). This figure highlights the poor azimuthal distribution of receivers (stations) around the PS01 station.

Near the center of the secondary microseism band (T=8 s), most results of the Iberian Peninsula center stations reflect a dominance of noise sources towards the southeast with an azimuth distribution ranging from ~90º to ~125º. Moroccan center stations (Figure 3.19f, 3.19g and 3.19h) together with PS01 center station (Figure 3.19e) showed a more variable pattern. These center stations did not show strong noise coming from the Mediterranean coastline as preferential direction.

In the primary microseism, the seismic noise directionality was distributed over a wider azimuth range than the observed for short period noise. Nevertheless, ELOB (Ourense) (Figure 3.19j) and EARI (Asturias) (Figure 3.19k) center stations did not present significant differences in the azimuthal distribution of the incoming energy in the entire microseismic band. Moreover, larger periods analyzed in this study (T=18 and 20 s) displayed normalized amplitudes with similar azimuthal pattern.

Figures presented in this study have shown the different azimuthal dependence of the primary and secondary microseism. Such observations have been related to different physical mechanisms of generation for the two microseism peaks and/or different source generation locations [e.g. *Tian and Ritzwoller*, 2015]. However, to implement methods that allow locating noise sources such as beamforming [e.g. *Schulte-Pelkum et al*., 2004; *Gerstoft and Tanimoto*, 2007] are beyond the scope of this thesis.

Once the azimuthal distribution of Rayleigh wave normalized amplitudes has been examined, we study the effects of heterogeneous noise sources on noise attenuation measurements. To do so, we calculated the EGF amplitude decays of the center stations shown in Figure 3.19 at the same four periods. Numerical simulations have proved that the EGF amplitude decay extracted from positive and negative correlation lags is not equal due to differences between outgoing and incoming noise intensities [*Weaver*, 2011]. *Zhang and Yang* [2013] illustrated the difference of the EGF amplitude decay between positive and symmetric components using a linear array. In our study, we measured amplitude decays from the symmetric EGF component. To reduce scattering because of the azimuthal dependence of the incoming noise, we also averaged EGF amplitudes over the azimuth following the procedure described in section 2.3.

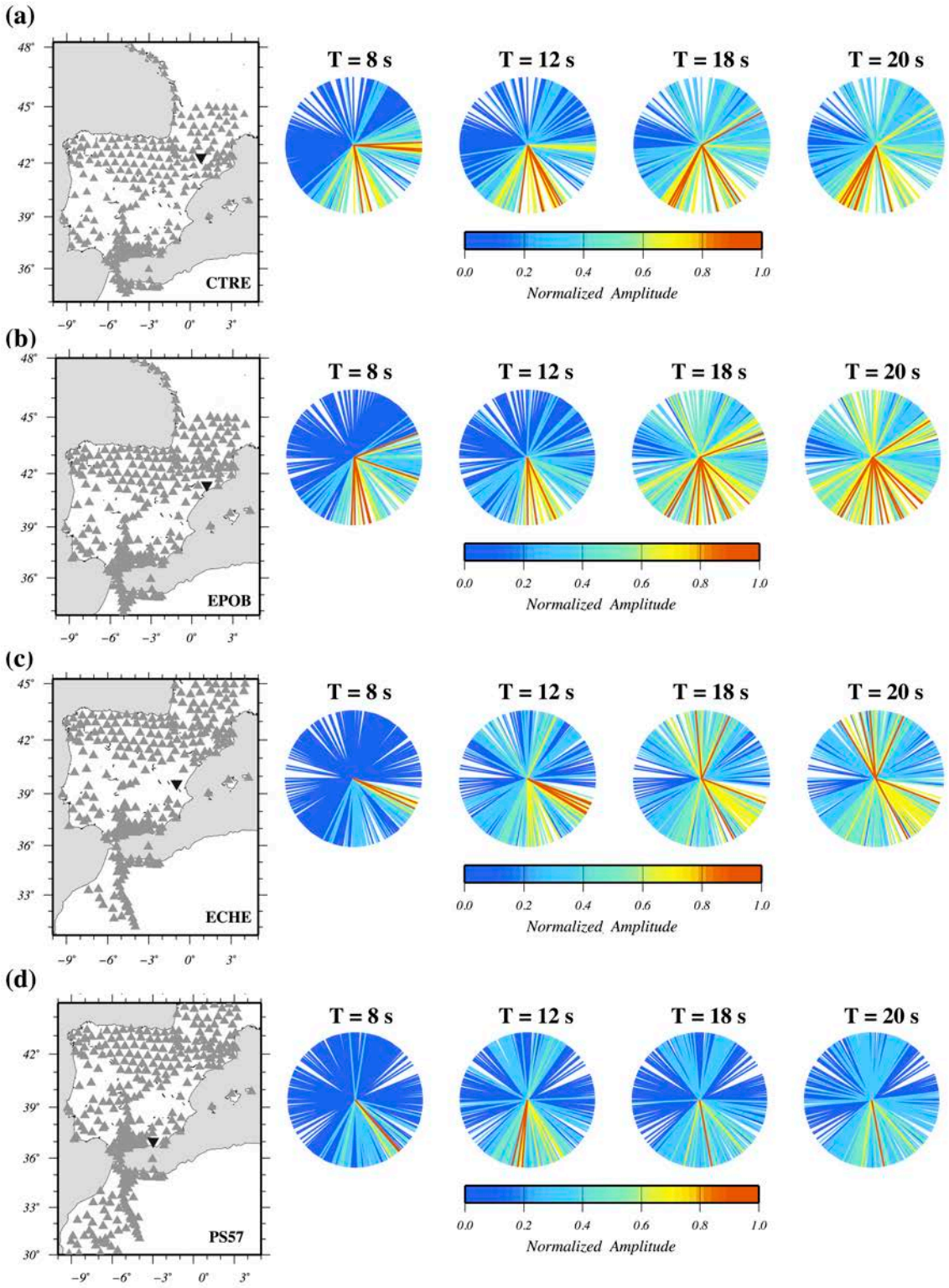

Figure 3.19: Normalized amplitude of the cross-correlations averaged during about 2 years versus azimuth at periods of 8, 12, 18 and 20 s and the corresponding location maps for: (a) CTRE station, (b) EPOB station, (c) ECHE station and (d) PS57 station.

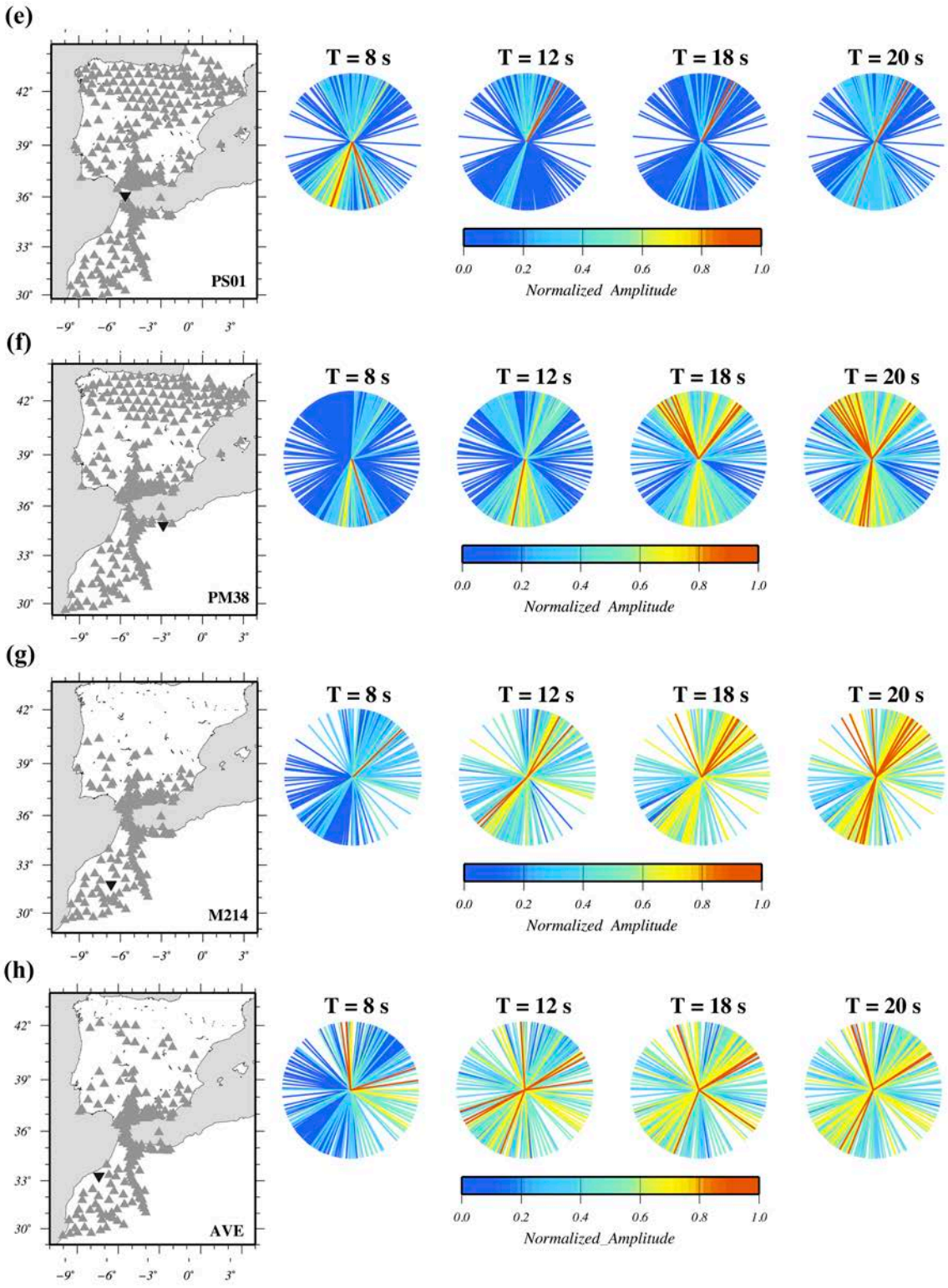

Figure 3.19 continued: for the center stations (e) PS01, (f) PM38, (g) M214 and, (h) AVE station.

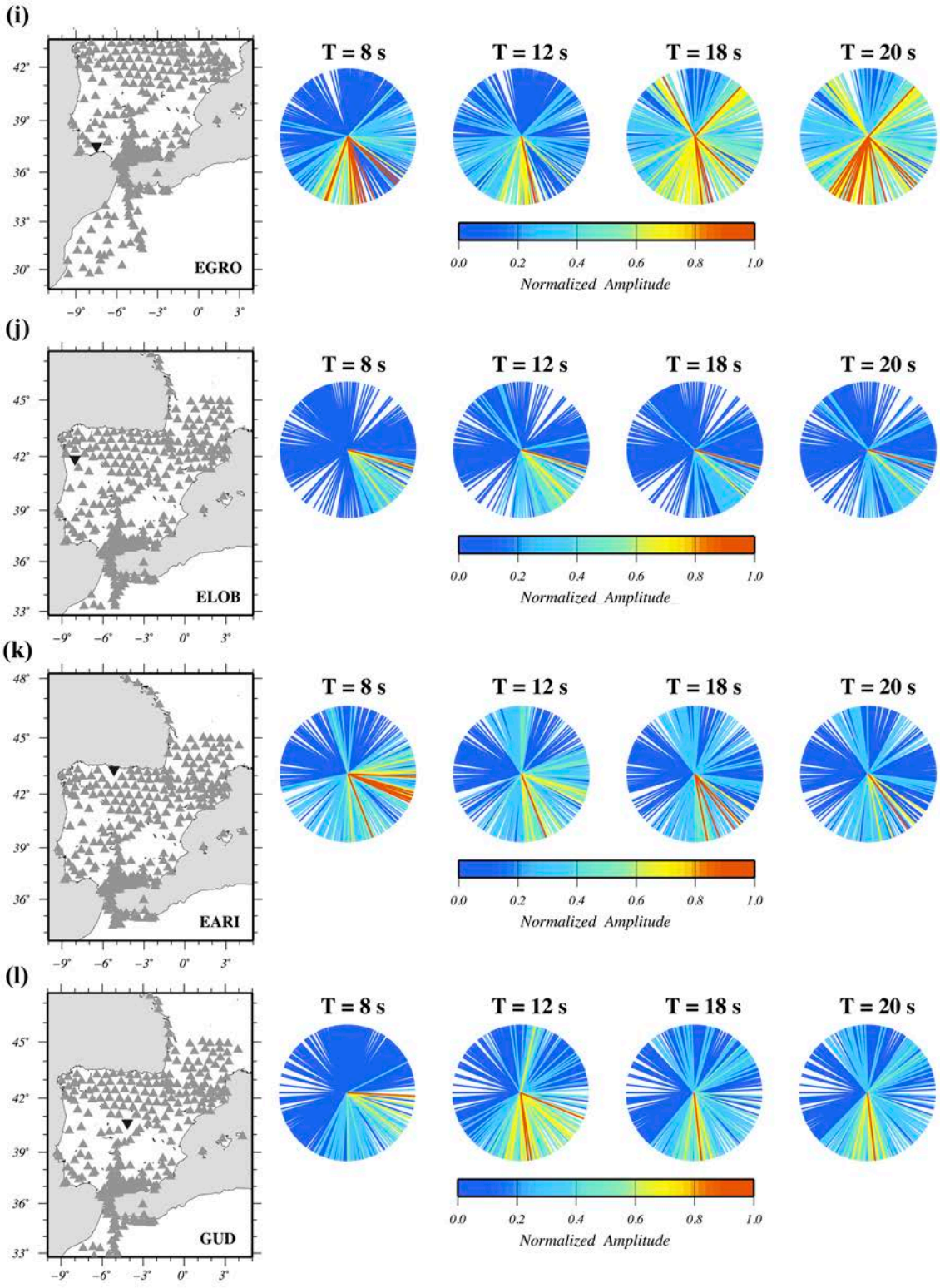

Figure 3.19 continued: for the center stations (i) EGRO, (j) ELOB, (k) EARI and, (l) GUD.

Figure 3.20 shows estimated EGF amplitudes corrected by length duration and geometrical spreading at periods of 8, 12, 18 and 20 s together with the EGF amplitudes also corrected for azimuthal variations (black dots) versus interstation distance. The straight line represents the best fit for a distance range up to 1000 km. The slope obtained from linear regression analysis is related to the Rayleigh wave attenuation coefficient a by,

$$\ln(Ar^{1/2}) = \alpha r \tag{3.1}$$

where A is the amplitude of the symmetric component of the cross-correlation measured using FTAN and r is the interstation distance. Rayleigh wave attenuation coefficients obtained fitting Equation 3.1 are indicated in Figure 3.20.

Rayleigh wave attenuation coefficients estimated by linear regression fitting can be related to quality factors by,

$$Q = \pi / \alpha T \beta \tag{3.2}$$

where β is the Rayleigh wave group velocity at the period T (see Equation 1.3). The group velocity of the Rayleigh waves at each period was estimated averaging the group velocity dispersion curves of the Iberian Peninsula and Morocco [*Silveira et al.*, 2013]. Values used are listed in Table 3.2.

Spatially and azimuthally averaged α values estimated from Figure 3.20 and their associated standard deviations are listed in Table 3.3. Red values of Table 3.3 indicated either very large values results or negative α values. Q values estimated from equation 3.2 are also listed. Positive amplitude decays such as those observed for the PS57 center station are associated with negative quality factors. Center stations located in the Betic-Rif range (PS01 and PM38) and southeastern Iberia (ECHE) show surprisingly large Q estimates at 8 s period in comparison with the others station.

Then, taking into account the effects of heterogeneous noise source distribution and poor seismic network coverage on our attenuation results, average Q estimates for each center station covering the IMR together with their associated standard deviations are plotted in Figure 3.21.

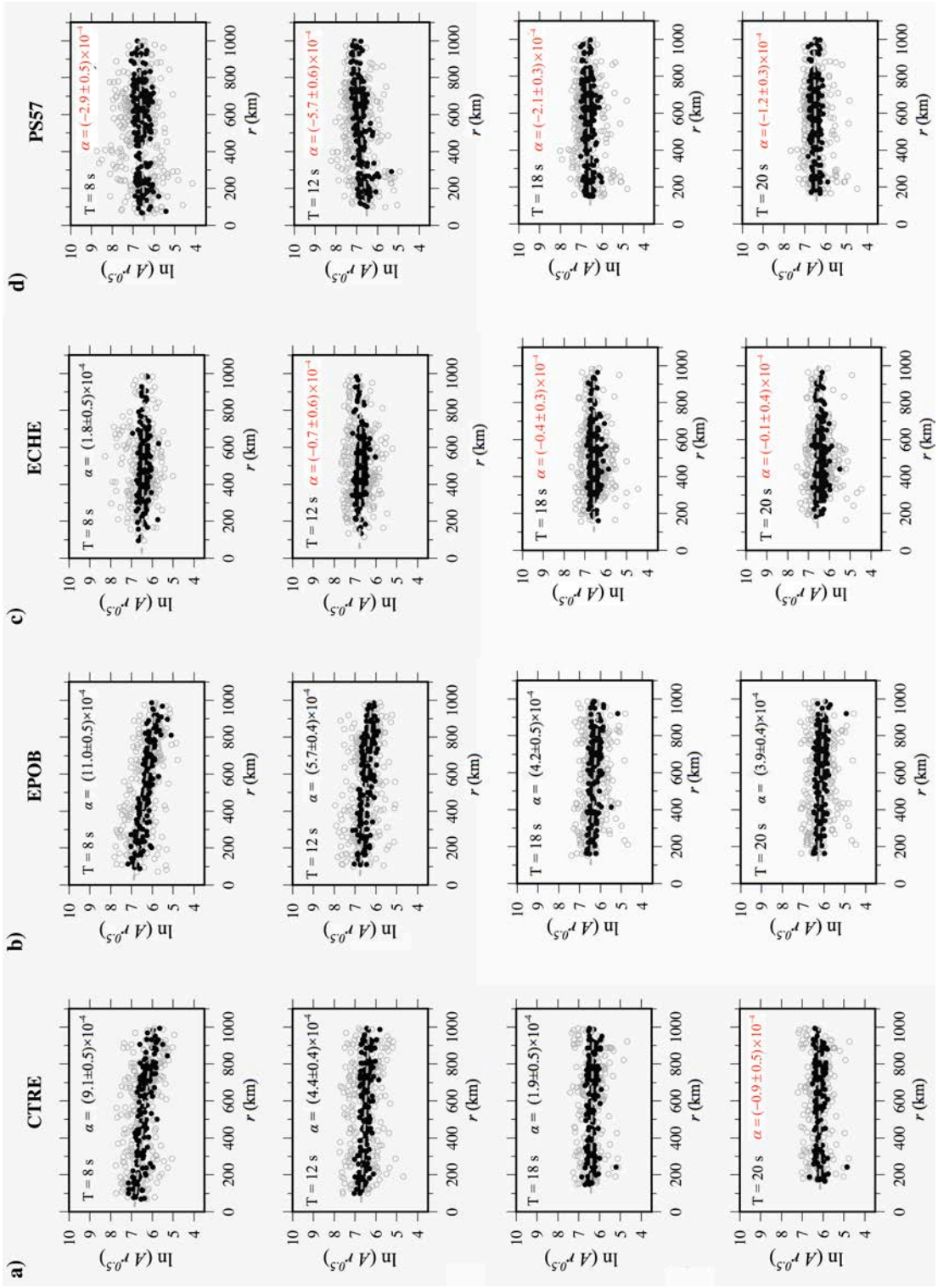

Figure 3.20: Amplitudes corrected for geometrical spreading and time duration (gray dots) together with amplitudes corrected also for azimuthal variation (black dots) versus interstation distance at periods of 8, 12, 18 and 20 s. The straight line represents the best fit for a distance up to 1000 km. The attenuation coefficients values obtained are indicated. For the station center: (a) CTRE, (b) EPOB, (c) ECHE and (d) PS57.

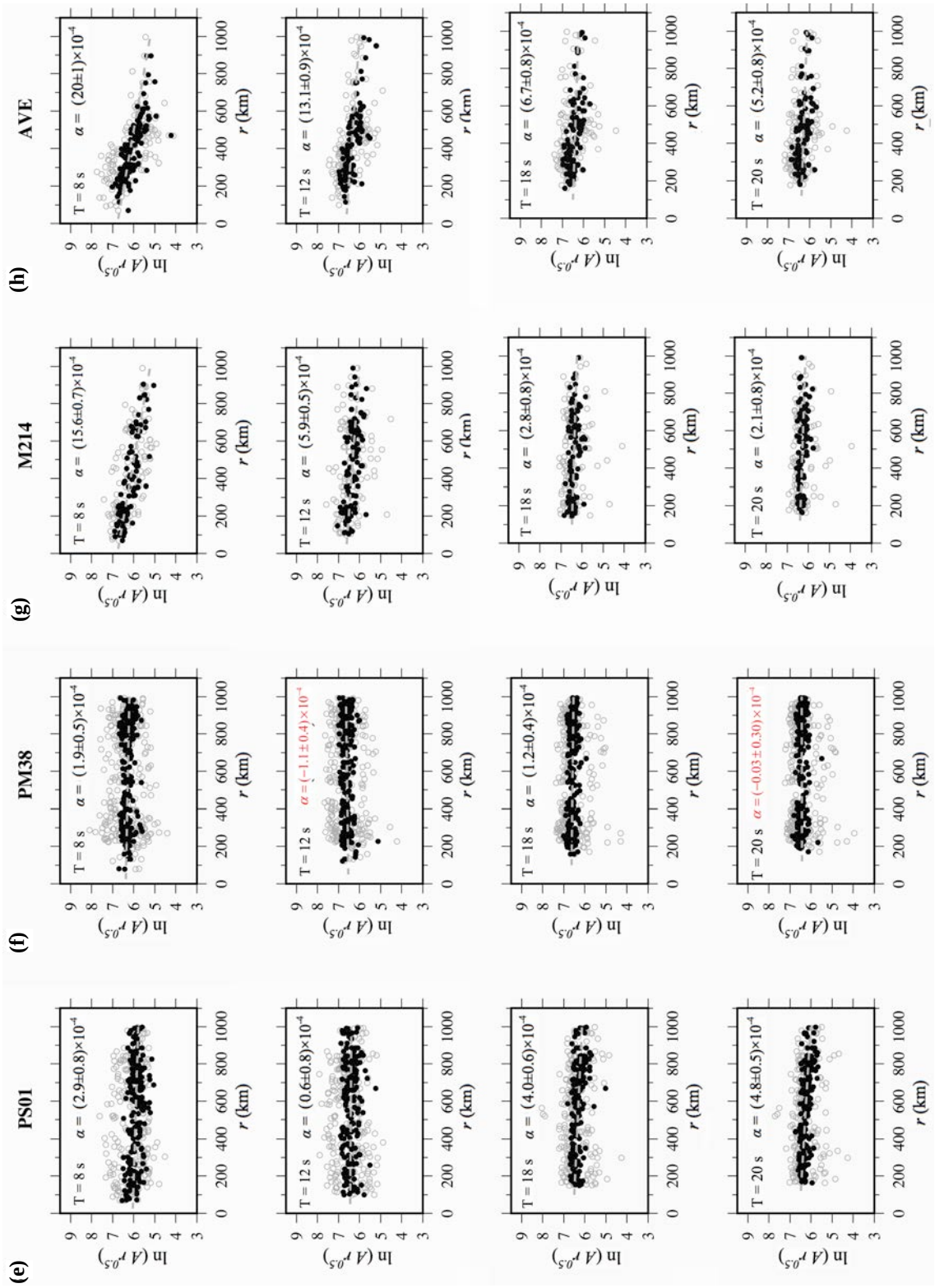

Figure 3.20 continued: for the station center (e) PS01, (f) PM38, (g) M214 and (h) AVE.

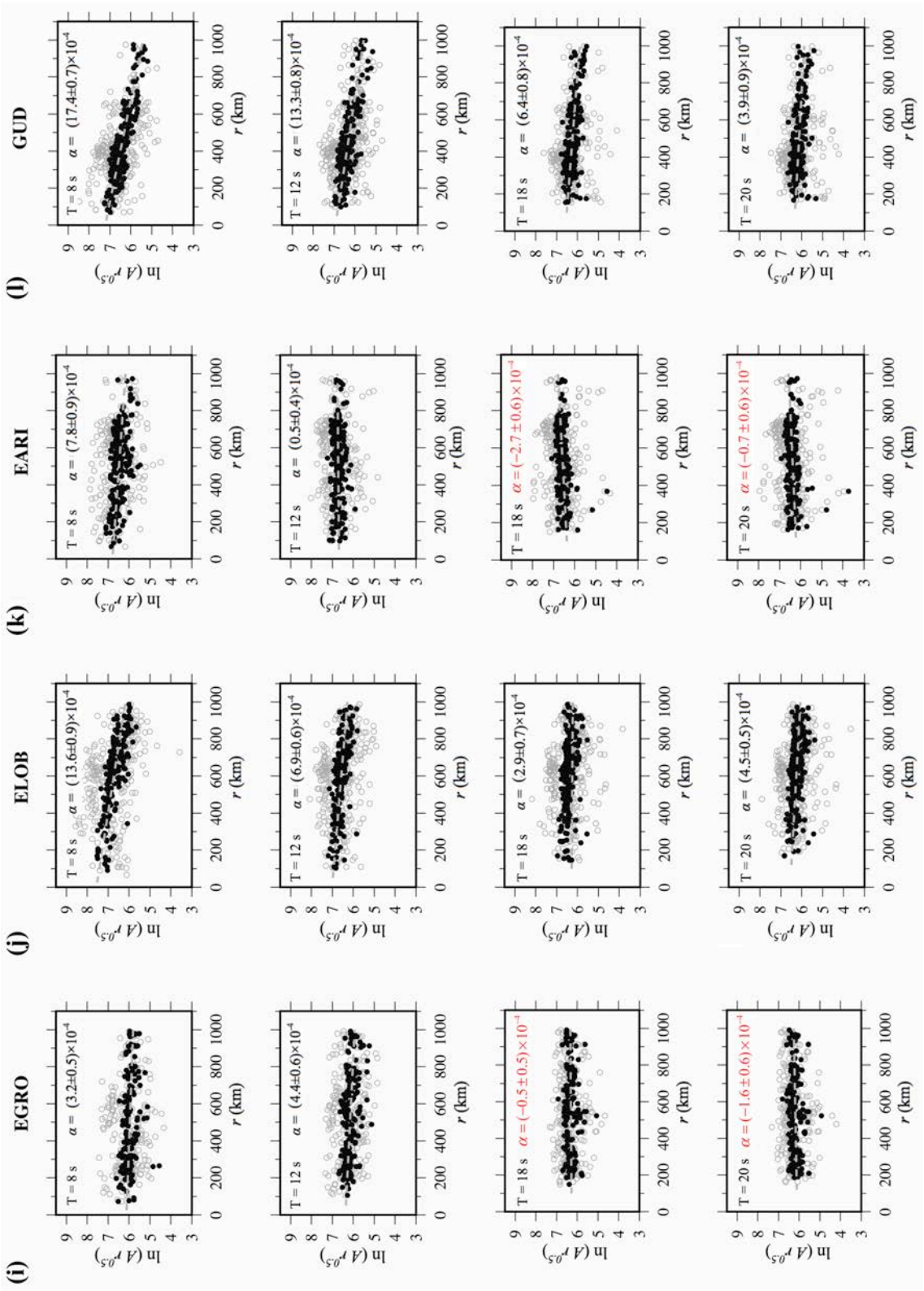

Figure 3.20 continued: for the station center (i) EGRO, (j) ELOB, (k) EARI and (l) GUD.

T / s	B_{Iberia} / km/s	$B_{Morocco}$ / km/s
8	2.69	2.71
12	2.76	2.75
18	2.92	2.85
20	3.00	2.93

Table 3.2: Rayleigh wave group velocity values at different periods for the IMR.

Station	**T = 8 s**			**T = 12 s**			**T = 18 s**			**T = 20 s**		
	$\alpha\times10^{-4}$	$\sigma\times10^{-4}$	Q	$\alpha\times10^{-4}$	$\sigma\times10^{-4}$	Q	$\alpha\times10^{-4}$	$\sigma\times10^{-4}$	Q	$\alpha\times10^{-4}$	$\sigma\times10^{-4}$	Q
CTRE	9.1	±0.5	160	4.4	±0.4	216	1.9	±0.5	315	-0.9	±0.5	-582
EPOB	11.0	±0.5	133	5.7	±0.4	166	4.2	±0.5	142	3.9	±0.4	134
ECHE	1.8	±0.5	811	-0.7	±0.6	-1355	-0.4	±0.3	-1494	-0.1	±0.4	5236
PS57	-2.9	±0.5	-503	-5.7	±0.6	-166	-2.1	±0.3	-285	-1.2	±0.3	-4363
PS01	2.9	±0.8	503	0.6	±0.8	1581	4.0	±0.6	149	4.8	±0.5	109
EGRO	3.2	±0.5	456	4.4	±0.6	216	-0.5	±0.5	-1195	-1.6	±0.6	-327
ELOB	13.6	±0.9	107	6.9	±0.6	137	2.9	±0.7	206	4.5	±0.5	116
EARI	7.8	±0.9	187	0.5	±0.4	1897	-2.7	±0.6	-221	-0.7	±0.6	-308
GUD	17.4	±0.7	84	13.3	±0.8	71	6.4	±0.8	93	3.9	±0.9	134
PM38	1.9	±0.5	768	-1.1	±0.4	-862	1.2	±0.4	498	-0.03	± 0.30	-17453
M214	15.6	±0.7	94	5.9	±0.5	161	2.8	±0.8	213	2.1	±0.8	249
AVE	20	±1	73	13.1	±0.9	72	6.7	±0.8	89	15.2	±0.8	101

Table 3.3: Attenuation values α and their corresponding standard deviation estimated from the symmetric EGF amplitude decay measurements for stations plotted in Figure 3.20. Rayleigh Q values were derived from equation 3.2. Red values are either negative α values or α estimates with large standard deviation values. Dotted line separates Iberian (upper) and Moroccan (down) stations.

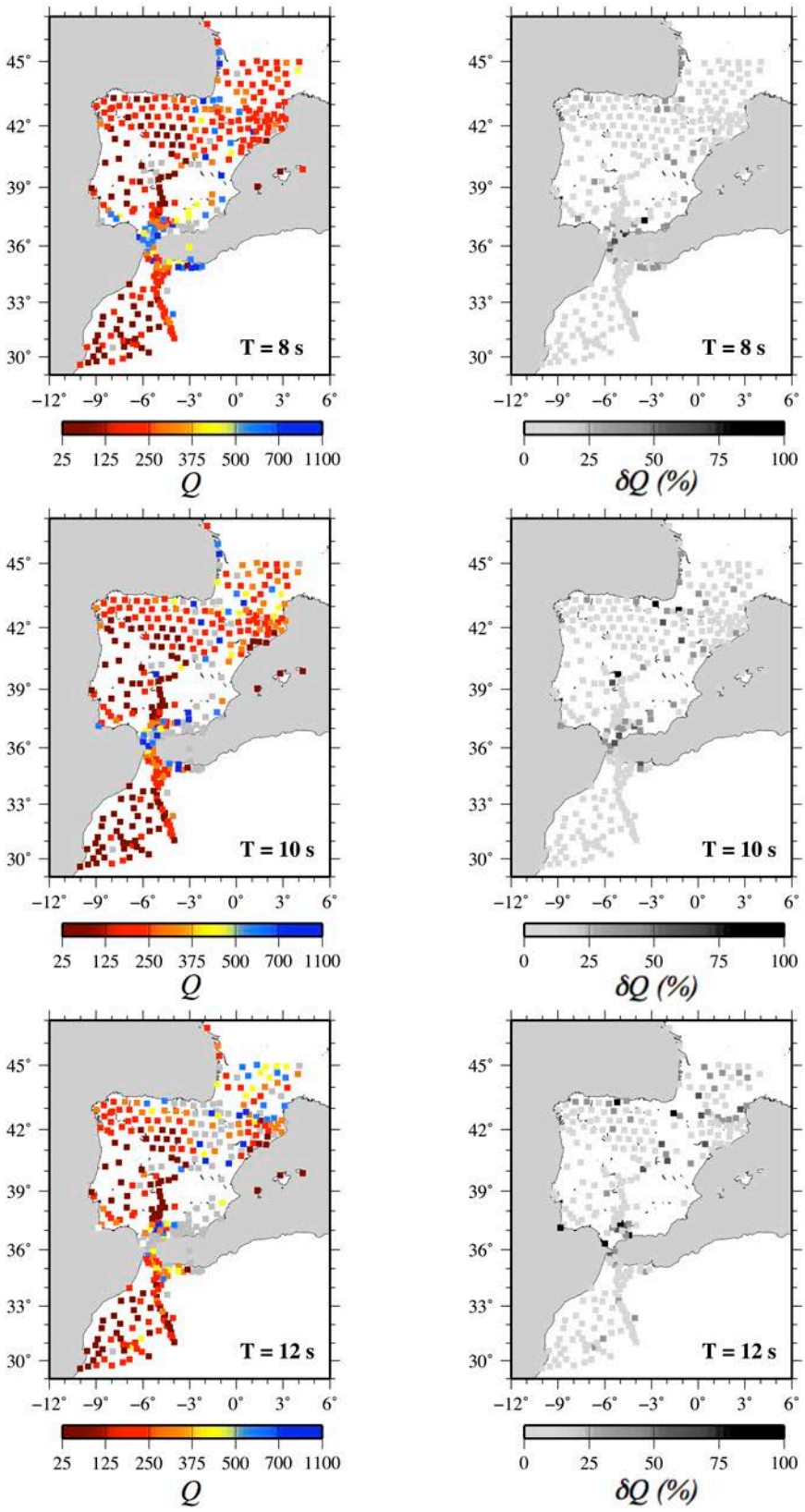

Figure 3.21: Left panels show azimuthally and spatially averaged Rayleigh *Q* values at each center station for 8, 10 and 12 s period. Grey squares are *Q* values either negative or with spatial variations larger than 100%. Right panels plot the standard deviation of every center stations at the same periods.

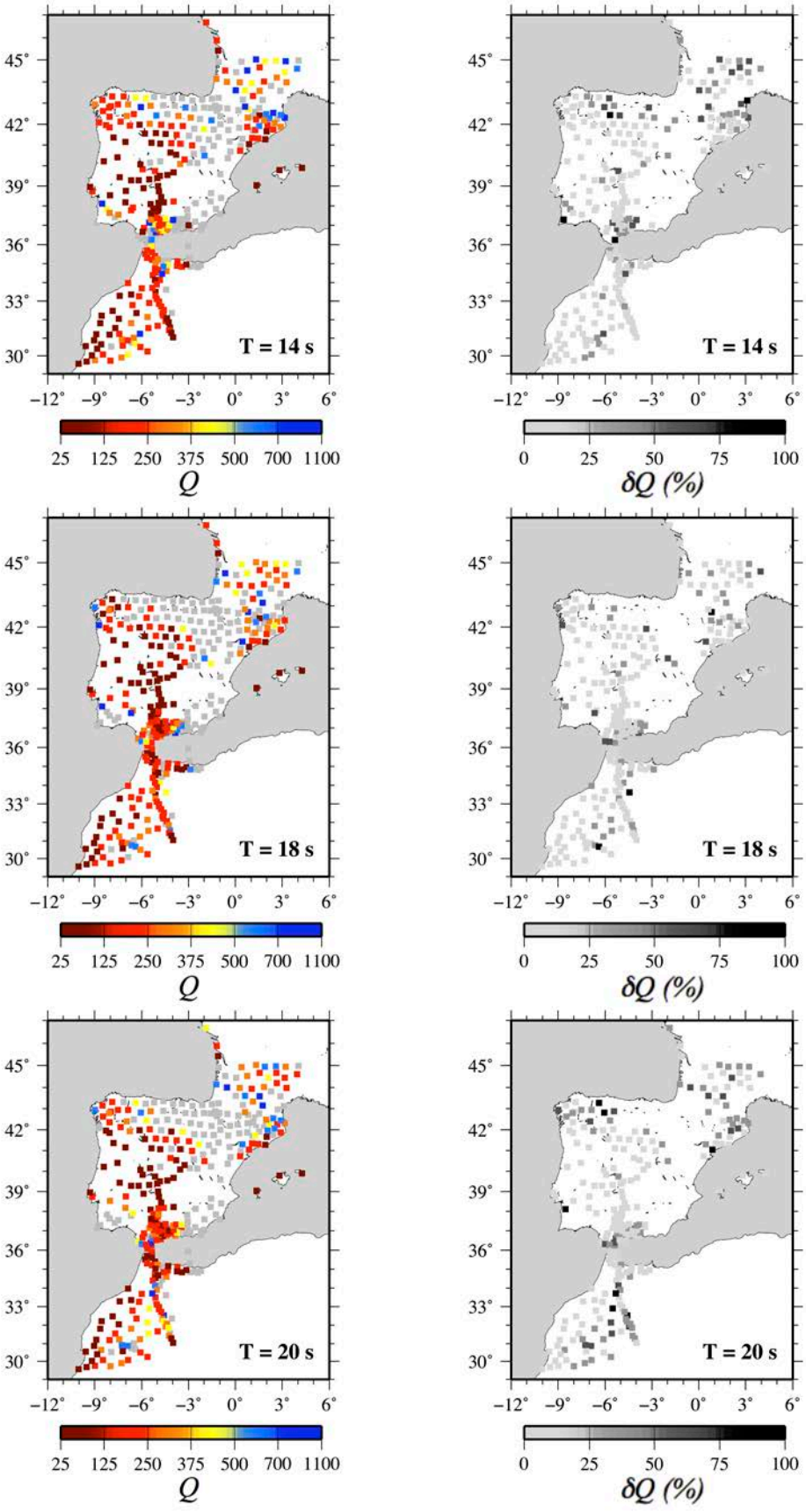

Figure 3.21 (continued): For 14, 18 and 20 s period

4. DISCUSION

I will discuss if both earthquakes and noise measurements provide reasonable *Q* values. In this regard, *Q* estimates will be related to the seismic activity and the geotectonic context of the IMR. In particular for the Iberian Peninsula, the *Lg* Q_0 model obtained allows correlating attenuation results with regional structures such as sedimentary basins and stable regions.

Further analyses such as the effect of the noise source distribution have been conducted to examine the reliability of the *Q* values estimated from ambient noise measurements. The accuracy of *Q* estimates will also be checked by comparing earthquake and noise-derived measurements.

Finally, our results will be compared with previous studies carried out in the region as well as with attenuation parameters estimated in other regions of the world.

4.1. *Lg* and Rayleigh *Q* Estimates

A large set of seismic data that includes seismic noise and earthquakes has been processed in this work to infer the crustal attenuation properties of the IMR. As a result of this variety of data, different approaches were implemented for the analysis of the anelastic structure of the IMR crust.

In this thesis, traditional methods (based on earthquakes) were first applied to estimate the lateral variations of the *Lg Q* and its frequency dependence in the IMR. Taking advantage of the dense quantity of *Lg* waveforms in the Iberian Peninsula, we resolved the spatial variation of *Lg* Q_0 using the TS method. The resulting map plotted in Figure 3.5 reflects large variations in Q_0 values across the Iberian Peninsula (*Lg* Q_0 ranging from approximately 75 to 800). The most striking feature observed is the contrast between the higher *Q* values in the western Iberian Peninsula that are related to the stable crust of the Iberian Massif and the lower estimates in the Pyrenean range and eastern Iberia. Low Q_0 values displayed in the eastern part of the Iberian Peninsula may be related to abrupt changes in the crustal thickness from the Valencia Trough toward the Mediterranean Sea that block the *Lg* waves. Other regions that exhibits high *Lg* attenuation are the southwestern border of the Iberian Massif, which could be associated with the presence of the Algarve sedimentary basin, the southern part of the Iberian Massif bounded by the Guadalquivir basin, the central zones of the Iberian Peninsula (the Tagus basin) and, the Betic range. In addition to relating estimated *Lg* Q_0 values to geology, the *Lg* Q_0 model can be correlated with the heat flow map of the Iberian Peninsula of *Fernández et al.*, [1998] (Figure 4.1) and the surface heat flow density map at European scale included in the Atlas of Geothermal Resources in Europe [*Hurter and Haenel*, 2002]. According to these maps high heat flow measurements (> 70 mW/m^2) agree with high attenuation in the central and western Pyrenees, the Tagus basin, and the eastern Iberian Peninsula. These results are consistent with studies which associated low *Lg* Q_0 values with high heat flow measurements [e.g., *Mitchell*, 1995*; Gallegos et al.*, 2014], and suggest that *Lg* attenuation may be affected by high crustal temperatures in these regions.

Figure 3.7 shows broad regions with maximum η values between 0.6 and 0.9 whereas few zones correspond to lower η measurements. In this work, we are not able to observe a consistent pattern of η with high or low Q_0 measurements. The Q_0 values obtained for the Iberian Peninsula are, in general, greater than those found in eastern Eurasia [*Xie et al.*, 2006] and the Turkish

Plateau [*Zor et al*., 2007] using the TS method. *De Miguel et al*. [1992], at a local scale, found a frequency dependence of η =0.93 in the Granada Basin (southern Spain), which is in agreement with the values obtained in this study.

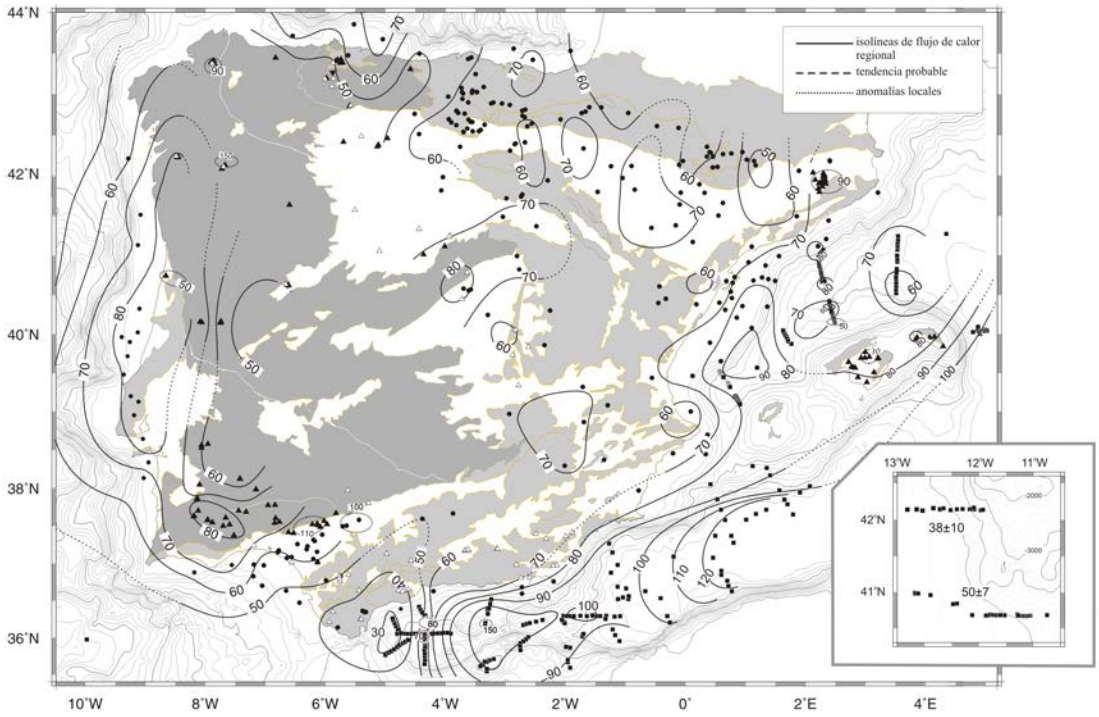

Figure 4.1: Heat flow map of the Iberian Peninsula extracted from *Fernández et al.*, [1998].

Once the laterally varying *Lg* Q_0 model was obtained for the Iberian Peninsula, the TS method was used to image the spatial variations of the *Lg* wave attenuation in northern Morocco. Limited source-station configuration reduced significantly the number of TS paths. Figure 4.2a reflects the poor data coverage for imaging the spatial variations of the *Lg* Q_0 in Morocco. The reliability of the inverted *Lg* Q_0 values (Figure 4.2b) is affected by poor sampling for the defined grid. However, the low Q_0 values observed in the Rif Mountains, the Middle Atlas and the Central High Atlas correlate well with areas of seismic activity. The stable Moroccan Meseta located to the west of the High Atlas displays high Q_0 values.

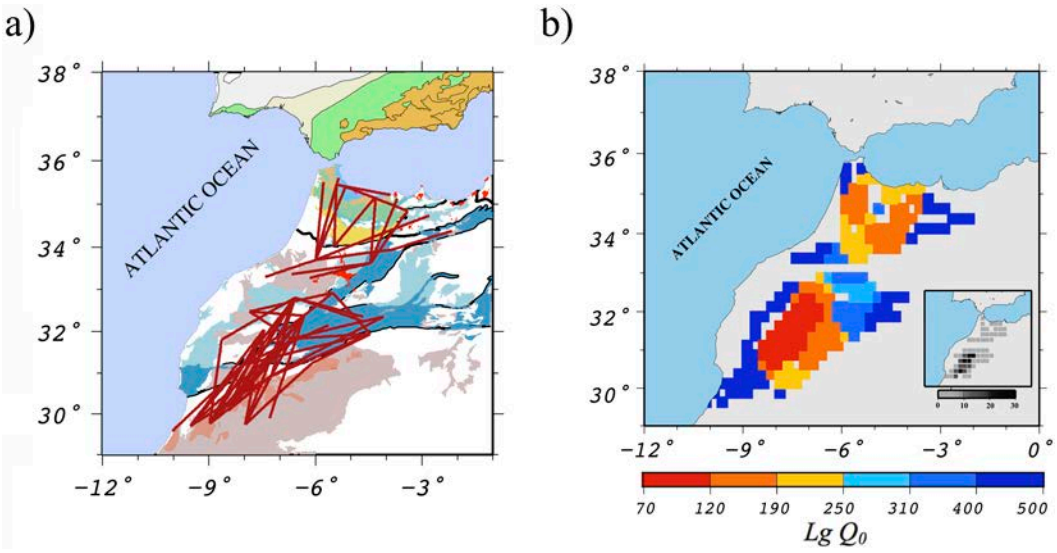

Figure 4.2: (a) TS paths and (b) Spatial variation of *Lg* Q_0 in northern Morocco together with the hit counts map where darker areas are the more sampled zones.

Two different approaches were then applied to estimate average *Lg* attenuation and its frequency dependence in Morocco. Figure 3.10 plots the *Lg Q* estimates as a function of frequency using the CN and the SAD methods for Morocco. For both methods, larger uncertainties were observed for the *Q* estimate at f_c= 0.9 Hz than for the other *Q* estimates at higher frequencies. Furthermore, weak frequency dependence is observed below 1.5 Hz (Figure 3.10). The relatively large errors observed at lower frequencies found in other works [e.g. *Benz et al.*, 1997*; Ottemöller et al.*, 2002; *Mousavi et al.*, 2014] may be associated with a stronger influence of the radiation pattern that has not been included in the formulation [*Erickson et al.*, 2004*; Singh et al.*, 2004]. Figure 3.10 also displays a minimum *Lg Q* value around 1.5 Hz. *Benz et al.* [1997] and *Otemöller et al.* [2002] found a minimum between 0.5 and 1 Hz in the western United States and around 1.5 Hz in southern Mexico, respectively. These results are in agreement with *Aki* [1980] and *Sato* [1990] that postulated the existence of a lithospheric attenuation peak near 1 Hz.

In the results sections, I also pointed out a distinct change in the frequency dependence above 4.5 Hz, with exponents ranging from 1.26 to 1.41. *Benz et al.*, [1997] noticed a similar behavior for the North American Basin and Range Province. This is likely to represent contamination of the *Lg* window by *Sn* energy at high frequencies (see Figures 3.2, 3.8 and 3.9), as shown by *Shin and Herrmann* [1987]. The higher frequency contents of the *Sn* phase compared to the *Lg* may introduce an upward bias in the *Lg Q* estimate [*Sereno et al.*, 1988]. Hence, we suggest that the model constrained to the frequency bandwidth below 4.5 Hz may represent the *Q* function in Morocco.

The *Lg Q* values obtained for hypocentral distances up to 400 km using the CN and SAD methods for Morocco are within the error bounds for the studied frequency range as it is shown in Table 3.1, indicating that the results are robust to differences in the methods. Because the distance limit of the homogeneity assumption of the coda energy has not been fully tested [e.g. *Ford et al.*, 2008], this result supports the extension of the coda normalization method to regional distances, at least up to 400 km in the study region. Greater *Q* values at high frequencies are obtained from SAD when larger hypocentral distances are involved in the inversion. Earlier results could be related to *Sn* coda contamination at high frequencies when large distances are involved [*Shin and Herrmann* 1987].

Q estimates obtained from *Lg* spectral measurements give realistic attenuation results that are in good agreement with the seismic activity of the IMR. Regions where seismic activity levels are relatively low such as western Iberia display high Q_0 values, whereas regions such as the Pyrenean range or the eastern Iberia show relatively low Q_0 values. This fact could be related to the effect of scattering attenuation due to the presence of tectonic complexity and small-scale structural heterogeneities. Moreover, areas with moderate seismicity are usually associated with intermediate *Lg* Q_0 observations as those *Lg* Q_0 values at 1.5 Hz observed in Morocco.

The fact that the IMR is an area of low-to-moderate (M_w < 5) seismicity prompted us to implement ambient noise methodologies in order to complement the attenuation results of this region.

Before discussing noise attenuation results presented in Figure 3.21, we will focus on analyzing the azimuthal content of the normalized amplitudes observed in Figure 3.19 and their influence on noise attenuation measurements. Figure 3.19 reflects different azimuthal distribution for the two microseisms. A stronger azimuthal dependence is observed for the secondary microseism. For the primary microseism, noise coming from a wide range of azimuths can be recognized. The secondary microseism has been observed to remain stable over the whole year whereas the primary microseism exhibits seasonal variability [e.g. *Stehly et al.*, 2006]. Since our results were calculated from cross-correlations stacked over ~2 years, the seasonal dependence of the primary microseism has been eliminated. At short periods (T=8s), noise sources are stable in time and coming mostly from the east. These results are in disagreement with previous results [e.g. *Ermert et al.*, 2016]. On the other hand, strong seismic noise emerges from most directions at longer periods (T=18-20 s) because these noise sources change over time [e.g. *Poli et al.*, 2013]. The results of this work suggest that attenuation

estimations could be biased due to prevailing direction of the seismic noise in the secondary microseism.

For all the study periods, the Moroccan center stations M214 (Sakat Azilal) (Figure 3.19g) and AVE (Averroes) (Figure 3.19h) displayed a broad range of noise source distributions with no clear preferential directions that might be related to a reasonably isotropic noise distribution observed in Morocco in the microseism band [*Ermert et al.*, 2016]. In this regard, stations located in Morocco can be considered as being reasonable well illuminated to estimate reliable EGF attenuation coefficients [e.g. *Tsai*, 2011; *Weaver*, 2011].

The ELOB (Ourense) center station (Figure 3.19j), located in the northwest of the Iberian Peninsula, shows normalized amplitudes significantly higher towards the southeast for the entire microseism band. The EARI (Asturias) center station (Figure 3.19k), situated in north central Iberia, also exhibited similar azimuthal pattern in the four periods considered. These azimuthal distributions may be associated with the fact that noise sources are less spatially variable in the Atlantic coast (from North Galicia margin to Bay of Biscay) than in the Mediterranean [*Chevrot et al.*, 2007]. As a result, center stations located in the north of the Iberian Peninsula should be carefully used for noise attenuation studies.

On the other hand, numerical studies carried out by *Lawrence et al.* [2013] demonstrated that reliable noise attenuation measurements could be estimated from heterogeneous noise source distribution if cross-correlated EGFs have been stacked over long time series and uniform seismic network coverage is available. Among all center stations analyzed (Figure 3.19) the CTRE (Lleida) center station (Figure 3.19a) is a good example that satisfies this condition.

In order to empirically verify the previous hypothesis, noise and earthquake amplitude decay measurements were compared. We first selected the nearest avalilable earthquake to CTRE station (Δ~200 km) whose magnitude (m_{bLg}=4.1) allowed us to compare noise and earthquakes results. Figure 4.3 shows the epicenter as well as recording stations.

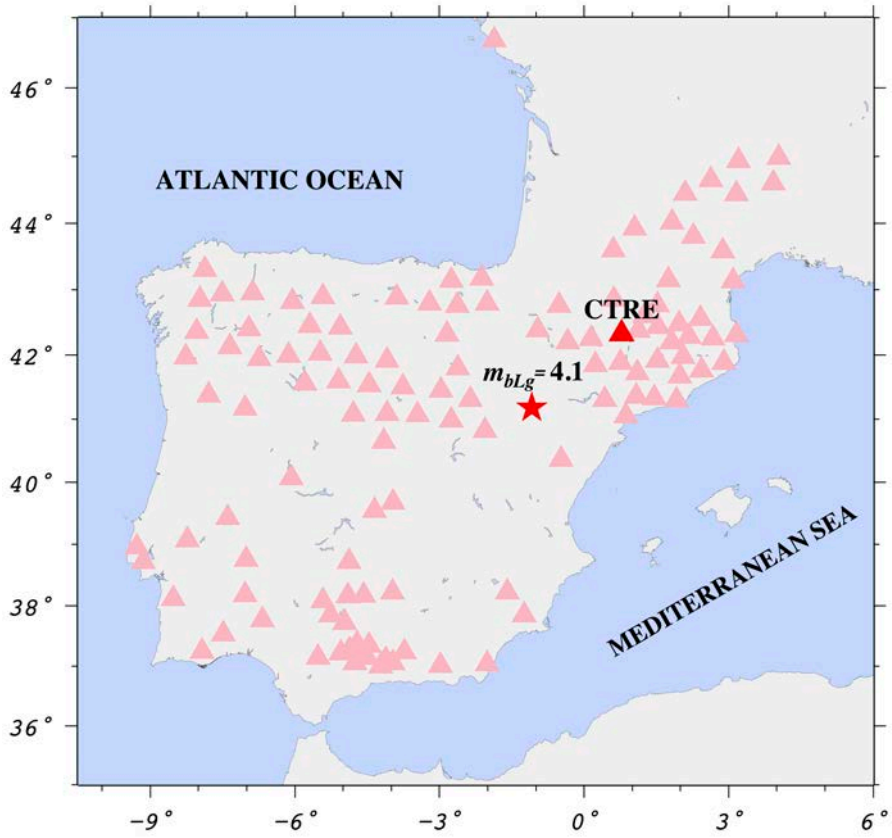

Figure 4.3: Epicenter of the event used. Station locations with valid amplitude measured for the estimation of *Q* and the epicenter of the event used (star). The center station CTRE is shown as a red triangle.

We measured Rayleigh wave amplitudes using FTAN from earthquake waveforms. Then, amplitudes were corrected for geometrical spreading and for azimuthal variations to account for the source radiation pattern [*Lin et al.*, 2011]. We performed the same azimuthal correction as the noise measurements (explained in section 2.3). Figure 4.4 shows estimated earthquake and noise amplitudes versus distance. Notice that distance refers to interstation distance from CTRE (as center station) for noise and epicentral distance for the earthquake. The straight line represents the best fit for distances up to 1000 km. Azimuthally averaged Rayleigh wave attenuation coefficients estimated from earthquakes and noise measurements are similar. Therefore, these observations would confirm our noise results for the center station CTRE.

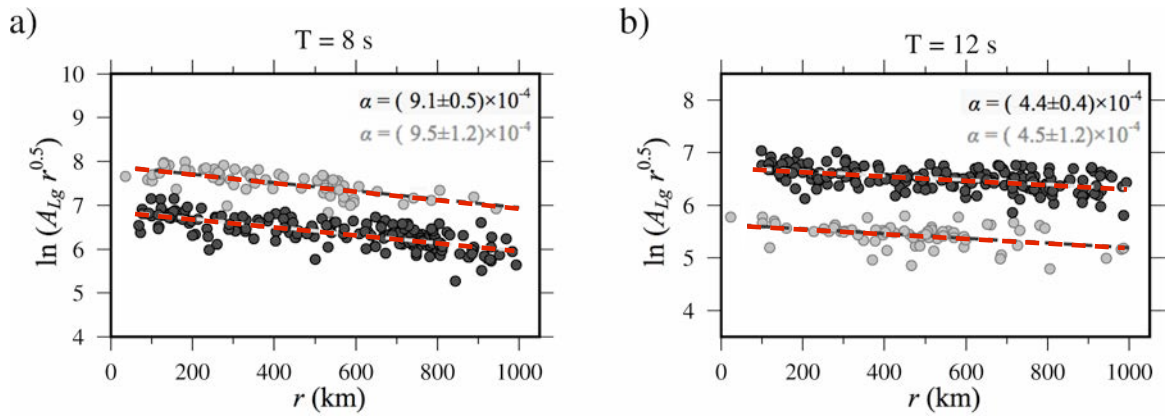

Figure 4.4: Comparison between the symmetric EGF amplitudes corrected for geometrical spreading, time duration and azimuthal variation (black dots) and earthquake (m_{bLg}=4.1) amplitude measurements corrected for geometrical spreading and azimuthal variation (grey dots) against distance at periods of: (a) 8 s and (b) 12. The straight line represents the best fit for a distance up to 1000 km. The attenuation coefficients values obtained are also indicated.

Figure 3.21 shows average Rayleigh *Q* results ranging from 25 to 1100 across the IMR. As would be expected, low *Q* values were obtained at shorter periods over the entire study region except for the Betic-Rif Range. *Q* values of the Betic-Rif area are surprisingly large at short period and have large standard deviations. Such results may indicate that attenuation is not properly retrieved due to poor azimuthal distribution of both noise sources and stations. Figure 3.21 shows a decrease of the station density as the period increases in the northeastern Iberia. Spatially and azimuthally averaged *Q* values tend to be more homogeneous in Morocco where noise source distribution is also more homogenous than in the Iberian Peninsula in the microseismic band [Ermert et al., 2016]. As a result, Moroccan stations may be considered as being well illuminated by noise sources to estimate reliable attenuation values.

To check the reliability of the noise attenuation estimates in Morocco, noise and earthquake measurements were compared. We selected M214 as center station because it has reasonable station coverage (see Figure 3.19g). Earthquake measurements were computed from an earthquake of magnitude 4.4 located at Δ~400 km (Figure 4.5). Amplitudes were measured as we did for Figure 4.4. Figure 4.6 illustrates noise and earthquakes results at period of 8, 12 and 14 s. Azimuthally averaged Rayleigh wave attenuation coefficients extracted from both sources are in good agreement for the three periods analyzed.

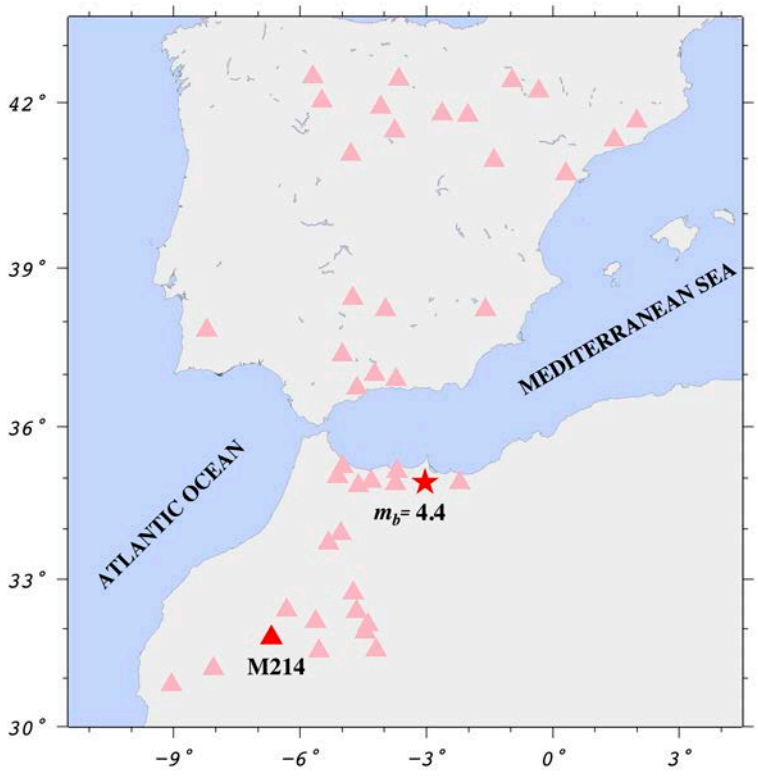

Figure 4.5: Epicenter of the event used. Station locations with valid amplitude measured for the estimation of *Q* and the epicenter of the event used (star). The center station M214 is colored in red.

This work has been the first attempt at measuring Rayleigh wave attenuation from EGF amplitudes in the IMR. However, further analysis has to been made to reduce bias of noise attenuation results and to image lateral variation across the study region.

Table 4.1 list Rayleigh *Q* values estimated from Figures 4.4 and 4.6 using Equation 3.3.

		***T* = 8 s**		***T* = 12 s**		***T* = 14 s**	
		Q	**σ**	**Q**	**σ**	**Q**	**σ**
IBERIA	***CTRE***	*160*	*±9*	*216*	*±20*	-	-
	m_{bLg}=*4.1*	*154*	*±19*	*211*	*±56*	-	-
MOROCCO	***M214***	*94*	*±4*	*161*	*±14*	*353*	*±154*
	m_b=*4.4*	*99*	*±8*	*146*	*±27*	*280*	*±106*

Table 4.1: Rayleigh *Q* values estimated from noise and earthquake amplitude measurements and their corresponding standard deviations.

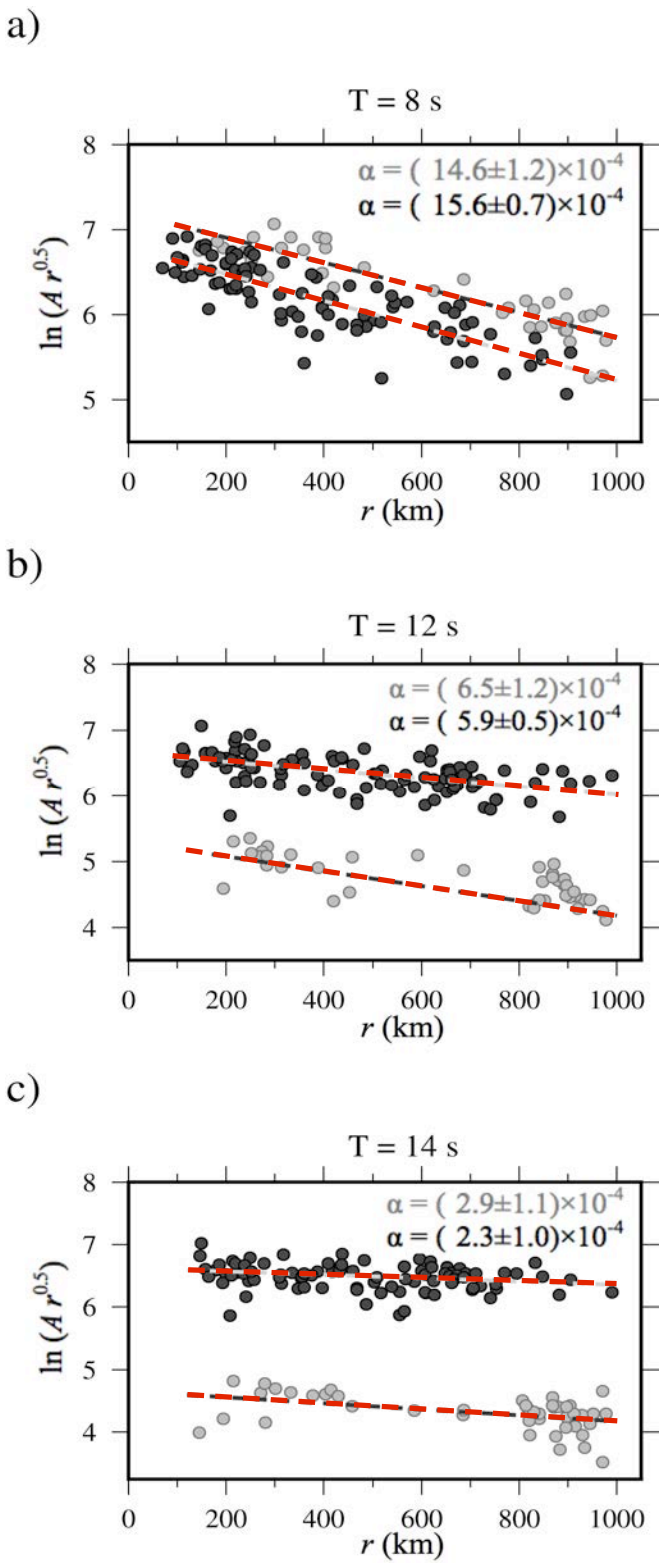

Figure 4.4: Comparison between the symmetric EGF amplitudes corrected for geometrical spreading, time duration and azimuthal variation (black dots) and earthquake amplitude measurements corrected for geometrical spreading and azimuthal variation (grey dots) versus distance at periods of: (a) 8 s, (b) 12 s and (c) 14 s. The straight line represents the best fit for a distance up to 1000 km. The attenuation coefficients values obtained are also indicated.

4.2. IMR Previous Attenuation Studies

Few studies on *Lg* attenuation have been performed in the study region. For southern Iberia, *De Miguel et al*. [1992] applied the reverse TS method and found *Lg* $Q_0 \sim$ 100 for the Granada basin. *Mitchell et al*. [2008] estimated low Q_0 values (200–300) for Spain as part as their *Lg* Q_0 map of Eurasia. This result is in agreement with the average $Q_0 \sim$ 265 estimated for the entire Iberian Peninsula in this thesis. Moreover, *Pujades et al.* [1990] found the lowest Q_0 values in the southeastern part of Iberia and in the Pyrenean domain, whereas the highest Q_0 values were observed in the northwest. These attenuation results were supported by the work of *Payo et al.* [1990], who showed that lower *Q* values were located in the internal–external units of the Betics and in the Pyrenean range, whereas high *Q* observations corresponded to the northwestern region, in the Iberian Massif. Thus, it has been confirmed that the *Lg* Q_0 general patterns found in this study correlate well with previous works on coda *Q* in the Iberian Peninsula.

Earlier works of *Lg* coda Q_0 carried out in continental Africa [*Xie and Mitchell*, 1990b; *Mitchell*, 1995] showed relatively low Q_0 values in the Atlas Mountains and higher values associated with surrounding stable areas such as the West Africa Craton and the East Saharan Craton.

Most Rayleigh attenuation studies in the Iberian Peninsula are based on long-period surface-wave measurements with large *Q* uncertainties below 30 km depth [e.g *Martínez et al*., 2005; *Lana et al*., 1999; *Caselles* et al., 1997]. For all these studies, the observed parameter is α and we derived *Q* values using equation 3.2 and the β values listed in Table 3.2. Among Rayleigh wave attenuation results, *Canas et al*. [1988] estimated average Rayleigh wave attenuation coefficients for periods of 10-30 s using the TS method. They obtained the highest attenuation values *Q* ~ 80 (α =14×10^{-4} km^{-1}) at T=10 s and *Q* ~ 45 (α =12×10^{-4} km^{-1}) at for T=20 s in the southeastern part of Iberia whereas the lowest attenuation values *Q* ~ 145 (α = 8×10^{-4} km^{-1}) at T=10 s and *Q* ~ 105 (α = 5×10^{-4} km^{-1}) at for T=20 s were observed in the West. These attenuation patterns were supported by the work of *Lana et al*. [1999] who showed that higher attenuation coefficients were located in the southeastern of the Iberian Peninsula ranging from *Q* ~ 80-115 (α ~10-12×10^{-4} km^{-1}) at 10 s to *Q* ~ 65 (α ~ 8-10×10^{-4} km^{-1}) at 20 s while lower attenuation observations corresponded to the northwestern region with values *Q* ~ 145-190 (α ~ 6-8×10^{-4} km^{-1}) and *Q* ~ 90-130 (α ~ 4-6×10^{-4} km^{-1}) for period of 10 and 20 s respectively.

Averaging earlier regionalized values, anelastic attenuation coefficients *Q* ~ 60 (α ~ 8.5×10^{-4} km^{-1}) and *Q* ~ 75 (α ~ 7×10^{-4} km^{-1}) at 20 s period were estimated for the entire Iberian

Peninsula. These results are in good agreement with our noise attenuation results obtained for the central western Iberia where Rayleigh *Q* values ranging from about 25 to 125 (Figure 3.21 at T=20s). However, southern Iberia (*Q* ~100-400) and areas surrounding Pyrenees Range (*Q* ~250-700) are not in concordance with early works.

4.3. Comparison with other Regions of the World

A number of studies on *Lg Q* frequency dependence functions published in different regions of the world are shown in Table 4.2. The method applied, together with the distance range and frequencies used is also indicated. By comparing average *Lg* Q_0 values of the entire Iberian Peninsula with results listed in Table 4.2, our results correlate well with those (Q_0 ~250–290) observed in Central France [*Campillo et al*., 1985], Britain [*Sargeant and Ottemöler*, 2009] and Hispaniola region [*McNamara et al*., 2012]. Results estimated from Morocco are between the models obtained by *Erickson et al*. [2004] for the central United States and *Chazalon et al*. [1993] for central Spain. The high Q_0 values of the Iberian Massif in northwestern Iberia are similar to those observed by *McNamara et al*. [2014] in the eastern United States and *Singh et al.* [2004] while the strong *Lg*-wave attenuation surrounding the Valencia Through is in agreement with *Akinci et al*. [1995] results for western Anatolia and Southern Spain and *Ford et al.* [2008] in northern California.

In a more general way, Table 4.2 shows that tectonically active regions are related to low *Lg Q* values [e.g., *Ford et al*., 2008; *Ottemöller*, 2002; *Ottemöller et al*., 2002; *Ojeda and Ottemöller*, 2002; *Ferdinand*, 1998; *Benz et al*., 1997; *Paul et al*., 1996; *Akinci et al*, 1995; *Chávez and Priestley*, 1986] whereas more stable tectonic areas are associated with high *Lg Q* [e.g., *Hasegawa*, 1985; *Chun et al*., 1987; *Shi et al*., 1996; *Chung and Lee*, 2003; *Singh et al*., 2004; *McNamara et al*., 2014; *Mousavi et al*., 2014]. Intermediate values of *Lg Q* correlate well with areas of moderate seismicity such as Xinjiang and adjacent regions [*Zhou et al*., 2011], North Korea [*Chun et al*., 2009] and South Africa [*Frankel et al*., 1990].

f(Hz)	*r* (km)	Q_0	η	Method	Region
0.9-10.75	100-1200	615 ± 25	0.35 ± 0.04	SAD	Continental Margin of Nova Scotia [Mousavi et al., 2014]
0.5-24	250-1100	751 ± 39	0.28 ± 0.05	SAD	Eastern United States [McNamara et al., 2014]
0.5-16	250-700	245 ± 31	0.61 ± 0.08	SAD	Hispaniola region [McNamara et al., 2012]
0.5-5	> 200	372	0.69	SAD	Xinjiang and its adjacent regions [Zhou et al., 2011]
1-4	> 1200	345±3	0.381 ± 0.006	RTS	North Korea [Chun and Henderson, 2009]
1-10	170-600	266	0.53	SAD	Britain [Sargeant and Ottemöller, 2009]
0.5-8	100-400	112 ± 7	0.55 ± 0.06	CN	Northern California [Ford et al., 2008]
0.5-24	110-800	152 ± 37	0.72 ± 0.16	SAD	Southern California [Erickson et al., 2004]
1-12	110-1300	470 ± 127	0.52 ± 0.16	SAD	Central United States [Erickson et al., 2004]
0.5-24	110-900	650 ± 143	0.36 ± 0.14	SAD	Northeast United States [Erickson et al., 2004]
0.5-24	110-800	200 ± 77	0.69 ± 0.16	SAD	Basin and Range Province [Erickson et al., 2004]
0.1-20	240-2400	800	0.42	SAD	Indian Shield [Sing et al., 2004]
1.5-24	155-400	556	0.54	CN	South Korea [Chung and Lee, 2003]
1.6-8	> 200	204 ± 25	0.85 ± 0.09	SAD	Southern Mexico [Ottemöller et al., 2002]
0.5-5	> 200	230	0.6	SAD	Colombia [Ojeda and Ottemöller, 2002]
0.5-5	> 200	128 ± 15	0.84 ± 0.08	SAD	Central America [Ottemöller, 2002]
0.2-3.6	200-500	126 ± 9	0.37 ± 0.02	TS	Eastern Tibetan plateau [Xie, 2002]
0.5-24	100-500	220 ± 30	0.66 ± 0.09	SAD	South-central Alaska [McNamara, 2000]
0.75-5	400-800	186 ± 7	0.78 ± 0.05	TAD	East African Rift [Ferdinand, 1998]
1-5	150-1000	235 ± 11	0.56 ± 0.04	SAD	Basin and Range Province [Benz et al., 1997]
1-7	150-700	187 ± 7	0.55 ± 0.03	SAD	Southern California [Benz et al., 1997]
1-8	150-400	138	0.76	SAD	Southern Sierra Nevada, California [Paul et al., 1996]
0.5-16	150-2000	366 ± 37	0.45 ± 0.06	SAD	Tibetan Plateau [McNamara et al., 1996]
0.5-16	41-1394	561	0.47	SAD	Appalachian Province [Shi et al., 1996]
0.5-16	41-1394	705	0.41	SAD	Northern New England [Shi et al., 1996]
0.5-16	41-1394	905	0.40	SAD	Adirondack Mountain [Shi et al., 1996]

Table 4.2: Frequency dependence *Lg*-wave attenuation functions obtained in different tectonic regions of the world. The frequency band, epicentral distance range, and method used are indicated (CN: coda normalization; SAD: spectral amplitude decay; TAD: temporal amplitude decay; TS: two-station; RTS: reverse two-station)

5. CONCLUSIONS

With this thesis I have performed a study of the crustal attenuation characteristics of the IMR. To develop this research I implemented three different earthquake-derived approaches that produced reasonable *Q* estimates. Additionally, a novel technique based on ambient noise amplitude measurements was introduced. For the ambient noise study, I first examined the behavior of a non-uniform distribution of noise sources on the EGF amplitude decays and then discussed the accuracy of the estimated averaged *Q* values.

In order to conduct this work a large seismic dataset was analyzed. This thesis took advantage of improvements in seismic data quality and broadband seismic station coverage of the IMR provided by the deployment of the IberArray and other temporary and permanent seismic networks. Such a large dataset made possible to estimate for the first time the regional variation of *Lg* Q_0 in the Iberian Peninsula and the frequency-dependent function of *Lg Q* in Morocco using high quality *Lg* waveforms measurements. Furthermore, I investigated the feasibility of the ambient seismic field for retrieving attenuation measurements. That is unprecedented for attenuation studies in the IMR

The main contributions of this thesis have been:

1. The first regional map that images the spatial variations of *Lg* Q_0 in the Iberian Peninsula. The results reached were:

   - Significant lateral Q_0 variations ranging approximately from 75 to 800.
   - Results correlate well with structural features: higher Q_0 values are related to the stable Iberian Massif in western Iberia while the lower Q_0 estimates are associated with the Pyrenean Range, and some areas in western, southern and eastern Iberian Peninsula where sedimentary basins exist and/or seismic activity is relatively important. Another high-attenuation area was also found in the Tagus Basin, in central Iberia.
   - Results correlate well with heat flow map of Iberia: low Q_0 values observed in the central and western Pyrenees, the Tagus basin and the eastern Iberia are related to high heat flow measurements.
   - The *Lg* propagation was found inefficient or blocked through Gibraltar Arc and adjacent areas, and across the deep ocean basin of the Mediterranean Sea.

2. The first frequency dependent estimate of *Lg Q* in the frequency band 1.5 to 4.5 Hz using the CN and SAD methods for Morocco. The results obtained were:

   - Weak frequency dependence is observed below to 1.5 Hz.
   - Relatively larger errors were observed at $f < 0.9$ Hz that may be associated with a stronger influence of the radiation pattern.
   - A change in the frequency dependence was observed above 4.5 Hz. The strong frequency dependence observed above 4.5 Hz is likely related to contamination of the *Lg* window by S_n energy at high frequencies.
   - The estimates using the CN and SAD (up to 400 km) methods are within the error bounds for the frequency band 0.8-8 Hz, supporting the extension of the coda normalization method to regional distances in Morocco.
   - Results reflect intermediate *Lg* Q_0 values at 1.5 Hz that are typically found in regions with moderate seismic activity.

3. The first study that exploited ambient noise records to infer crustal attenuation properties of the IMR. The principal aim of this work was to increase our understanding of the noise attenuation measurements through the knowledge of the different factors that affect EGF amplitude decays. Results revealed the following conclusions:

   - Strong directivity of the ambient noise was observed in the secondary microseism for most stations located in the Iberian Peninsula whereas noise sources tend to be more homogeneously distributed across the entire IMR for the primary microseism.
   - Decay constants estimated from earthquake and ambient noise measurements are consistent.
   - Accurate *Q* estimates could be retrieved from Moroccan stations except for those situated along the Rif Mountains.
   - Iberian stations that exhibit good azimuthal distribution of receivers and noise sources recover reliable noise attenuation results.
   - At a period of 20 s, our spatially averaged Rayleigh wave attenuation coefficients are in agreement with previous long-period surface-wave measured from earthquakes in the central part of the Iberian Peninsula.

In this thesis a significant effort has been made to increase our knowledge of crustal attenuation characteristics of the IMR. Different methods that provide overall consistent attenuation results have been performed. Work carried out in this research includes management

of large volumes of data, seismic signal processing, visual inspections, inversion and modeling and interpretation.

Some questions mainly related to methodology restrictions should be resolved in future studies. Some of this further investigation will be,

- Applying less restrictive tomographic methods to be able to image the lateral variations of *Lg* attenuation in Morocco.
- Calculating the influence of station site responses on the attenuation estimates.
- Investigating other ambient seismic noise approaches to better retrieve attenuation information from noise measurements in the Iberian Peninsula.

6. REFERENCES

Aki, K. and Richards, P.G., (2002). Quantitative Seismology, 2nd edn, University Science Books.

Aki, K. (1980b). Attenuation of shear waves in the lithosphere for frequencies from 0.05 to 25 Hz, *Phys. Earth Planet. Int.*, **21**, 50-60, doi: 10.1016/0031-9201(80)90019-9.

Aki, K., and B. Chouet (1975). Origin of coda waves: Source, attenuation, and scattering effects, *J. Geophys. Res.*, **80**, 3322-3342, doi: 10.1029/JB080i023p03322.

Aki, K. (1969). Analysis of seismic coda of local earthquakes as scattered waves, *J. Geophys. Res.*, **74**, 615-631, doi: 10.1029/JB074i002p00615.

Aki, K. (1957), Space and time spectra of stationary stochastic waves, with special reference to microtremors., *Bull. Earthquake Res. Institute*, University of Tokyo, **35**, 415–457.

Akinci, A., E. Del Pezzo, and J. Ibáñez (1995). Separation of scattering and intrinsic attenuation in southern Spain and Western Anatolia (Turkey), *Geophys. J. Int.*, **121**, 337–353, doi: 10.1111/j.1365-246X.1995.tb05715.x.

Barker, B. W., Z. A. Der, and C. P. Mrazek (1981). The effect of crustal structure on the regional phases *Pg* and *Lg* at the Nevada test site, *J. Geophys. Res.*, **86**, 1686–1700, doi: 10.1029/JB086iB03p01686.

Bensen, G. D., M. H. Ritzwoller, and Y. Yang (2009), A 3-D shear velocity model of the crust and uppermost mantle beneath the United States from ambient seismic noise, *Geophys. J. Int.*, **177**(3), 1177-1196.

Bensen, G.D, Ritzwoller, M.H., Barmin, M.P., Levshin, A.L., Moschetti, M.P., Shapiro, N.M., Yang, Y., (2007). Processing seismic ambient noise data to obtain reliable broad-band surface wave dispersion measurements, *Geophys J. Int.*, **169**, 1239–1260.

Benz, H., A. Frankel, and D. Moore (1997). Regional *Lg* attenuation for the continental United States, *Bull. Seismol. Soc. Am.*, **87**, 606-619.

Calvert A., E. Sandoval, D. Seber, M. Baranzangi, F. Vidal, G. Alguacil and N. Jabour (2000). Propagation of regional seismic phases (Lg and Sn) and Pn velocity structure along the Africa-Iberia plate boundary zone: tectonic implications, *Geophys. J. Int.*, **142**, 384–408.

Campillo, M. (1987). *Lg* wave propagation in a laterally varying crust and the spatial distribution of the quality factor in Central France, *J. Geophys. Res.*, **92**, 12604-12614.

Campillo, M., J. L.Plantet, and M. Bouchon (1985). Frequency-dependent attenuation in the crust beneath central France from *Lg* waves: Data analysis and numerical modeling, *Bull. Seismol. Soc. Am*., **75**, 1395–1411.

Canas, J.A., F. De Miguel, F. Vidal, and G. Alguacil, G., (1988). Anelastic Rayleigh wave attenuation in the Iberian Peninsula, *Geophys. J.*, **95**, 391-396.

Carcolé, E. (2006). Three-dimensional spatial distribution of scatterers in the crust by inversion analysis of *S*-waves coda envelopes. A case study of Gauribidanur seismic array site (southern India) and Galeras volcano (south-western Colombia). *Thesis*. Observatori de l´Ebre, Spain.

Caselles, J. O., J. A. Canas, L. Puajades, X. Lana, J. Badal, V. Corchete, and M. Navarro (1997). Improvements in the knowledge of the anelastic structure of the Iberian Peninsula from seismic data of the ILIHA project, *Geophys. J. Int.,* **129**, 702-714.

Claerbout, J. (1968). Synthesis of a layered medium from its acoustic transmission response, *Geophys.*, **33**, 264–269.

Chazalon, A., Campillo, M., Gibson, R., Carreno, E., (1993). Crustal wave propagation anomaly across the Pyrenean Range: Comparison between observations and numerical simulations. *Geophys. J. Int.,* **115**, 829–838.

Chávez, D.E. and Priestley, K.F. (1986). Measurement of frequency dependent *Lg* attenuation in the Great Basin, *Geophys. Res. Lett.*, **13**, 551-554.

Chevrot, S., M. Sylvander, S. Benahmed, C. Ponsolles, J. M. Lefevre, and D. Paradis, (2007). Source locations of secondary microseisms in western Europe: evidence for both coastal and pelagic sources, *J. Geophy. Res.*, **112**, B11301, doi:10.1029/2007JB005059.

Chun, K.Y., Y. Wu, and G. A. Henderson (2009). *Lg* attenuation near the North Korean border with China, Part I: Model development from regional earthquake sources, *Bull. Seismol. Soc. Am.*, **99**, 3021-3029, doi: 10.1785/0120080316.

Chun, K.Y., G. F. West, R. J. Kokoski, and C. Samson (1987). A novel technique for measuring *Lg* attenuation. Results from Eastern Canada between 1 to 10 Hz, *Bull. Seismol. Soc. Am.*, **77**, 398-419.

Chung, T. W., and K. Lee (2003). A study of high-frequency Q_{Lg}^{-1} in the crust of South Korea, *Bull. Seismol. Soc. Am.*, **93**, 1401–1406, doi: 10.1785/0120020199.

Cupillard, P., and Y. Capdeville (2010), On the amplitude of surface waves obtained by noise correlation and the capability to recover the attenuation: A numerical approach, *Geophys. J. Int.,* **181**, 1687–1700, doi:10.1111/j.1365-246X.2010.04586.x.

De Miguel, F., J. M. Ibáñez, G. Alguacil, J. A. Canas, F. Vidal, J. Morales, J. A. Peña, A. M. Posadas and F. Luzón (1992). 1-18 Hz Lg attenuation in the Granada Basin (southern Spain), *Geophys. J. Int,*. **111**, 270-280.

Der, Z., M. E. Marshall, A. O'Donnell, and T. W. McElfresh (1984). Spatial coherence structure and attenuation of the Lg phase, site effects and the interpretation of the *Lg* coda, *Bull. Seismol. Soc. Am.*, **74**, 1125-1147.

Erickson, D., D. E. McNamara, and H. M. Benz (2004), Frequency-dependent Lg Q within the Continental United States, *Bull. Seismol. Soc. Am.*, **94**, 1630-1643, doi: 10.1785/012003218.

Ermert, L., A. Villaseñor, and A. Fichtner, (2016). Cross-correlation imaging of ambient noise sources, *Geophys. J. Int.*, **204**, 347-364.

Fan, G. W., and T. Lay (2003). Strong *Lg* wave attenuation in the Northern and Eastern Tibetan plateau measured by a two-station/two-event stacking method, *J. Geophys. Res.*, **30**, no. 10, 1530, doi 10.1029/ 2002GL016211.

Fan, G. W., and T. Lay (2002). Characteristics of *Lg* attenuation in the Tibetan plateau, *J. Geophys. Res,*. **107**, no. 10, 2256, doi 10.1029/ 2001JB000804.

Ferdinand R. W. (1998). Average attenuation of 07-50 Hz *Lg* waves and magnitude scale determination for the region bounding the western branch of the East African Rift, *Geophys. J. Int.,* **134**, 818-830, doi: 10.1046/j.1365-246x.1998.00616.x.

Fernández, M., I. Marzán, A. Correia, and E. Ramalho (1998), Heat flow, heat production, and lithospheric thermal regime in the Iberian Peninsula, *Tectonophysics* **291**, 29-53, doi: 10.1016/S0040-1951(98)00029-8.

Ford, S. R., D. S. Dreger, K. Mayeda, W. R. Walter, L. Malagnini, and W. S. Phillips (2008). Regional attenuation in Northern California: A comparison of five 1D Q methods, *Bull. Seismol. Soc. Am.*, **98**, 2033–2046, doi: 10.1785/0120070218.

Frankel, A., A. McGarr, J. Bicknell, J. Mori, L. Seeber and E. Cranswick (1990). Attenuation of high-frequency shear waves in the crust: measurements from New York State, South Africa, and Southern California, *J. Geophys. Res.*, **95**, 17441-17457, doi: 10.1029/JB095iB11p17441.

Gallegos, A., N. Ranasinghe, J. Ni, and E. Sandvol (2014). *Lg* attenuation in the central and eastern United States as revealed by the EarthScope Transportable Array, *Earth Planet. Sci. Lett.*, **402**, 187-196.

Gerstoft, P., and T. Tanimoto (2007). A year of microseisms in southern California, *Geophys. J. Int.*, **34**, L20304, doi:10.1029/2007GL031091.

Hasegawa, H. (1985). Attenuation of *Lg* waves in the Canadian Shield, *Bull. Seismol. Soc. Am.*, **75**, 1569–1582.

Hasselmann, K. (1963). A statistical analysis of the generation of microseisms, *Rev. Geophys.*, **1**, 177–210, doi:10.1029/RG001i002p00177.

Huang, Y. C., H. Yao, B. S. Huang, R. D. van der Hilst, K. L. Wen, W. G. Huang, and C. H. Chen (2010). Phase velocity variation at periods of 0.5-3 seconds in the Taipei Basin of Taiwan from correlation of ambient seismic noise, *Bull. Seismol. Soc. Am.,* **100**, 2250-2263, doi:10.1785/0120090319.

Hurter, S., and R. Haenel Eds. (2002), Atlas of geothermal resources in Europe, Publication No. EUR 17811 of the European Commission, Office for Official Publications of the European Communities, L-2985 Luxembourg.

Kennett, B. L. N. (1986). *Lg* waves and structural boundaries, *Bull. Seismol. Soc. Am.,* **76** 1133-1141.

Lana, X., O. Caselles, J. A. Canas, , J. Badal, L. Puajades, and M. D. Martínez (1999). Anelastic structure of the Iberian Peninsula obtained from an automated regionalization algorith and stochastic inversion, *Tectonophysics.,* **304**, 219-239.

Larose, E., P. Roux, and M. Campillo, (2007). Reconstruction of Rayleigh-Lamb dispersion spectrum based on noise obtained from an air-jet forcing. *J. Acoust. Soc. Am.*, **122**, 3437–3444.

Lawrence, J. F., M. Denolle, K.J.Seats, and G. A. Prieto (2013). A numeric evaluation of attenuation from ambient noise correlation functions, *J. Geophys. Res.,* **118**, 6134-6145, doi:10.1007/2012JB009513.

Lay T. and T. C. Wallace (1995). Modern Global Seismology, *Academic Press, Inc*., United Kindom.

Levshin, A., L. Ratnikova, and J. Berger (1992). Peculiarities of surface-wave propagation across central Eurasia, , Bull. Seismol. Soc. Am., **82**, 2464–2493.

Levshin, A. L., V. F. Pisarenko, and G. A. Pogrebinsky (1972). On a frequency-time analysis of oscillations, *Ann. Geophys.*, **28**, 211-218.

Lin, F. C., V. C. Tsai, B. Schmandt, Z. Duputel, and Z. Zhan (2013). Extracting seismic core phases with array interferometry, *Geophys. Res. Lett.*, **40**, 1049–1053, doi:10.1002/grl.50237.

Lin, F. C., M. P. Moschetti, and M. H. Ritzwoller (2008). Surface wave tomography of the western United States from ambient seismic noise: Rayleigh and Love wave phase velocity maps, *Geophysical J. Int.*, **173**(1), 281-298.

Lin, F. C., M. H. Ritzwoller, and W. Shen (2011). On the reliability of attenuation measurements from ambient noise cross-correlations, *Geophys. Res. Lett.*, **38**(11), L11303.

Lobkis, O. I., and R.L. Weaver, (2001). On the emergence of the Green's function in the correlations of a diffuse field, *J. acoust. Soc. Am.*, **110**, 3011–3017.

Longuet-Higgins, M. S. (1950), A Theory of the Origin of Microseisms, *Philosophical Transactions of the Royal Society of London. Series A, Mathematical and Physical Sciences*, **243**, 1–35, doi:10.1098/rsta.1950.0012.

Martínez, M. D., X. Lana, O. Caselles, J. A. Canas, and L. Pujades (2003). Elastic-anelastic regional structures for the Iberian Peninsula obtained from a Rauleigh wave tomography and a causal uncoupled inversion, *Pure. Appl. Geophys.*, **162**, 2321-2353.

McNamara, D. E., L. Gee, H. M. Benz, and M. Chapman (2014). Frequency-dependent seismic attenuation in the Eastern United States as observed from the 2011 Central Virginia Earthquake and aftershock sequence, *Bull. Seismol. Soc. Am.*, **104**, 55–72, doi: 10.1785/01201130045.

McNamara, D. E, M. Meremonte, J. Z. Maharrey, S-L. Mildore, J. R. Altidore, D. Anglade, S. E. Hough, D. Given, H. Benz, L. Gee, and A. Frankel (2012). Frequency-dependent seismic attenuation within the Hispaniola Island region of the Caribbean Sea. *Bull. Seismol. Soc. Am.*, **102**, 773-782, doi: 10.1785/0120110137.

McNamara, D. E., and W. Walter (2001). Mapping crustal heterogeneity using *Lg* propagation efficiency throughout the Middle East, Mediterranean, Southern Europe and Northern Africa, *Pure appl. Geophys.*, **158**, 1165-1188.

McNamara, D. E. (2000). Frequency dependent *Lg* attenuation in South-Central Alaska, *Geophys. Res Lett*., **278**, 3494-3952, doi: 10.1029/2000GL011732.

McNamara, D. E., T. J. Owens, and W. R. Walter (1996). Propagation characteristics of *Lg* across the Tibetan Plateau, *Bull. Seismol. Soc. Am*., **86**, 457-469.

Menke, W. (1980). Geophysical data analysis: Discrete inverse theory, *Academic Press, Inc.*, San Diego, California.

Mitchell, B. J., L. Cong and G. Elström (2008). A continent-wide map of 1-Hz Lg coda Q variation across Eurasia and its relation to lithospheric evolution, *J. Geophys. Res.*, **113**, B04303, doi:10.1029/2007JB005065.

Mitchell, B. J., B. and Romawicz (1999). *Q* of the Earth: Global, Regional and Laboratory Studies, USA, Springer Basel AG.

Mitchell, B. J., Y. Pan, J. Xie and L. Cong (1997). *Lg* coda *Q* variation across Eurasia and its relation to crustal evolution, *J. Geophys. Res.*, **102**, 22767-22779.

Mitchell, B. J. (1995). Anelastic structure and evolution of the continental crust and upper mantle from seismic surface wave attenuation, *Rev. Geophys*., **33**, 441-462.

Mousavi, S. M., C. H. Cramer, and C. A. Langston (2014). Average Q_{Lg}, Q_{Sn}, and observation of *Lg* blockage in the Continental Margin of Nova Scotia, *J. Geophys. Res*., **119**, 7722–7744, doi:10.1002/2014JB011237.

Noriega, R., A. Ugalde, A. Villaseñor, and M. Harnafi (2015a). Frequecny-dependent *Lg*-wave attenuation in northern Morocco, *Tecthonophysics.*, **663**, 250-260.

Noriega, R., A. Ugalde, A. Villaseñor, and M. J. Jurado (2015b). Spatial Variation of *Lg*-wave attenuation in the Iberian Peninsula, *Bull. Seismol. Soc. Am.,* **105**, 420-430.

Ochoa M, Arribas J, Mas R, Goldstein RH (2007). Destruction of a fluvial reservoir by hydrothermal activity (Cameros Basin, Spain), *Sediment Geol.*, **202**, 158–173.

Ojeda A. and L. Ottemöller (2002). Q_{Lg} tomography in Colombia, *Phys. Earth Planet. Int*., **130**, 253-270, doi: 10.1016/S0031-9201(02)00010-9.

Oliver, J. and M. Ewing (1957). Higher mode surface waves and their bearing on the structure of the Earth´s mantle, *Bull. Seismol. Soc. Am.,* **83**, *1959-1970.*

Ottemöller, L. (2002). *Lg* wave *Q* tomography in Central America, *Geophys. J. Int.,* **150**, 295–303, doi: 10.1046/j.1365-246X.2002.01715.x.

Ottemöller, L., N. M. Shapiro, S. K. Singh, and J. F. Pacheco (2002). Lateral variation of *Lg* wave propagation in southern Mexico, *J. Geophys. Res.*, **107**(B1), ESE 3-1–ESE 3-13, doi: 10.1029/2001JB000206.

Pasyanos, M. E., E. M. Matzel, W. R. Walter and A. J. Rodgers (2009). Broadband *Lg* attenuation modeling in the Middle East, *Geophys. J. Int*., **177**, 1166-1176.

Paul, A., D. Jongmans, M. Campillo, P. Malin, and D. Baumont (1996). Amplitude of regional seismic phases in relation to crustal structure of the Sierra Nevada, *California, J. Geophys. Res*., **101**, 25243-25254, doi: 10.1029/96JB01906.

Payo, G., J. Badal, J. A. Canas, V. Corchete, L. Pujades and F. J. Serón (1990). Seismic attenuation in Iberia using the coda-Q method, *Geophys. J. Int*., **103**, 135-145.

Peterson, J. (1993). Observation and modeling of seismic background noise, *Open-file report, 93-322 Rep*, U.S. Geological Survey, Alburquerque, New Mexico.

Poli, P., H. A. Perdersen, M. Campillo, and the POLENET/LAPNET working Group (2013). Noise directivity and group velocity tomography in a region with small velocity contrasts: the northern Baltic shield, *Geophys. J. Int*., **192**, 413-424.

Press F., and M. Ewing (1952). Two slow surface waves across North America, *Bull. Seismol. Soc. Am.*, **42**, 219-228.

Prieto, G. A., J. F. Lawrence, and G. C. Beroza (2011). Anelastic Earth structure from the coherency of the ambient seismic field, *J. Geophys Res.*, **114**(B7), B07303.

Pujades, L. G., J. A. Canas, J. J. Egozcue, M. A. Puigví, J. Gallart, X. Lana, J. Pous and A. Casas (1990). Coda-Q distribution in the Iberian Peninsula, *Geophys. J. Int.*, **100**, 285-301.

Sabra, K., Gerstoft, P., Roux, P., Kuperman, W.A., Fehler, M.C., (2005a). Extracting time-domain Green's function estimates from ambient seismic noise. *Geophys Res Lett.,* **32** (3), 1–5.

Saadi, M. (1975). Cartes structurales du Moroc (Provinces du Nord). 1:2 000.000. Èditions du service géologique du Maroc.

Sandoval, E., K. Al-Damegh, A. Calvert, D. Seber, M. Barazangi, R. Mohamad, R. Gök, N. Türkelli, and C. Gürbüz, (2001). Tomographic imaging of *Lg* and *Sn* propagation in the Middle East, *Pure. appl. geophys*., **158**, 1121-1163.

Sato, H., and M. Fehler (1998). Seismic Wave Propagation and Scattering in the Heterogeneous Earth, *Springer and Verlag*, New York.

Sato, H. (1990). Unified approach to amplitude attenuation and coda excitation in the randomly inhomogeneous lithosphere, *Pure Appl. Geophys*., **132**, 1-29, doi: 10.1007/BF00874359.

Sato, Y. (1958). Attenuation, dispersion, and the wave guide of the G wave, *Bull. Seism. Soc. Am*., **48**, 231-251.

Schulte-Plkum, V., P. S. Earle, and F. L. Vernon (2004). Strong directivity of ocean-generated seismic noise, *Geochem. Geophys. Geosyst.,* **5**(3), doi:10.1029/2003GC000520.

Sereno, T. J., S. R. Bratt, and T. C. Bache (1988). Simultaneous inversion of regional wave spectra for attenuation and seismic moment in Scandinavia, *J. Geophys. Res.*, **93**, 2019–2035.

Shapiro, N. M., M. Campillo, L. Stehly, and M. H. Ritzwoller (2005). High-resolution surface-wave tomography from ambient seismic noise, *Science*, **307**(5715), 1615-1618.

Shapiro, N. M, and M. Campillo (2004). Emergence of broadband Rayleigh waves from correlations of the ambient seismic nois,. *Geophys Res Lett.,* **31** (7), 1615–1619.

Shi, J., W. Y. Kim, and P. G. Richards (1996). Variability of crustal attenuation in the northeastern United States from *Lg* waves, *J. Geophys. Res.*, **101**, 25231–25242, doi: 10.1029/96JB02580.

Shin, T., and Herrmann, R., (1987). *Lg* attenuation and source studies using 1982 Miramichi data, *Bull. Seismol. Soc. Am*., **77**, 384–397.

Silveira, G., N. A. *Dias, and A. Villaseñor (2017).* Seismic imaging of the western Iberian crust using ambient noise: Boundaries and internal structure of the Iberian Massif, *Tecthonophysics.,* **589**, 186-194.

Singh, C., M. Shekar, A. Singh, and R. K. Chadha (2012). Seismic attenuation characteristics along the Hi-CLIMB profile in Tibet from *Lg Q* inversion, *Bull. Seism. Soc. Am.*, **102**, 783-789, doi: 10.1785/0120110145.

Singh, S. K., D. Garcia, J. F. Pacheco, R. Valenzuela, B. K. Bansal, and R. S. Dattatrayam (2004). *Q* of the Indian shield, *Bull. Seism. Soc. Am.*, **94**, 1564–1570, doi: 10.1785/012003214.

Sonley, E., and G. M. Atkinson (2006). Path-specific attenuation in eastern Canada, *Bull. Seism. Soc. Am.*, **96**, 1375-1382.

Stehly, L., M. Campillo, and N.M. Shapiro, (2006). A study of the seismic noise from its long-range correlation properties, *J. Geophys. Res.*, **111**(B10), B10306, doi:10.1029/2005JB004237.

Stein, S., and M. Wysession (2003). An Introduction to Seismology, Earthquakes and Earth Structure, UK Blackwell Publishing Ltd.

Taylor, S.R., Velasco, A.A., Hartse, H.E., Phillips, W.S., Walter, W.R., Rodgers, A.J., (2002). Amplitude corrections for regional seismic discriminants. *Pure. App. Geophys.*, **159**, 623–650.

Tian Y., and M. H. Ritzwoller (2015). Directionality of ambient noise on the Juan de Fuca plate: implications for source locations of the primary and secondary microseism, *Geophys. J. Int.*, **201**, 429-443.

Tsai, V. C., (2011). Understanding the amplitudes of noise correlation measurements, *J. Geophys. Res.*, **116**, B09311, doi:10.1029/2011JB008483.

Tsujiura, M., (1978). Spectral analysis of the coda waves from local earthquakes, *Bull. Earthquake Res. Inst. Univ. Tokyo*, **53**, 1-48.

Villaseñor, A., Y. Yang, M. H. Ritzwoller, and J. Gallart, (2007). Ambient noise surface wave tomography of the Iberian Peninsula: Implications for shallow seismic structure, *Geophys. Res. Lett.*, **34**, L11304, doi:10.1029/2007GL030164.

Wapenaar, K., and J. Fokkema (2006), Green's function representations for seismic interferometry, *Geophys,*, **71**(4), SI33–SI46, doi:10.1190/1.2213955.

Wapenaar, K., (2004). Retrieving the elastodynamic Green's function of an arbitrary homogeneous medium by cross correlation, *Physical Review E* **69**, 046610.

Wéber, Z. (2000). Seismic traveltime tomography: A simulated annealing approach, *Phys. Earth Planet In.*, **119**, 149-159.

Weaver, R. L., (2011). On the amplitudes of correlations and the inference, *C.R. Geosci.*, **343**, 615-622.

Weemstra, C., L. Boschi, A. Goertz,, and B. Artman, (2013). Seismic attenuation from recordings of ambient noise, *Geophysics*, **78**(1), Q1–Q14.

Wu, R. S. (1985). Multiple scattering and energy transfer of seismic waves – separation of scattering effect from intrinsic attenuation- I. Theoretical modeling, *Geophys. J. R. Astr. Soc.*, **82**, 57-80.

Xie, J., Z. Wu, R. Liu, D. Schaff, Y. Liu and J. Liang (2006). Tomographic regionalization of crustal Lg Q in eastern Eurasia, *J. Geophys. Res*., **33**, L03315, doi:10.1029/2005GL024410.

Xie, J., R. Gok, J. Ni, and Y. Aoki (2004). Lateral variation of crustal seismic attenuation along the INDEPTH profiles in Tibet from *Lg Q* inversion, *J. Geophys. Res.*, **109**, B10308, doi:10.1029/2004JB002988.

Xie, J., and B. J. Mitchell (1990a). Attenuation of multiphase surface waves in the Basin and Range Province. I. *Lg* and *Lg* coda, *Geophys. J. Int.*, **102**, 121-137.

Xie, J., and Mitchell, B.J., (1990b). A back projection method for imaging large-scale lateral varia- tion in *Lg* coda *Q* with application to continental Africa. *Geophys. J. Int.*, **100**, 161–181.

Xie, J., and O. W. Nuttli (1988). Interpretation of high-frequency coda at large distances: stochastic modeling and method of inversion, *Geophys. J.*, **95**, 579-595.

Yang, Y., and M.H. Ritzwoller (2008). Characteristics of ambient seismic noise as a source for surface wave tomography, *Geochem. Geophys. Geosyst.*, **9**, doi:10.1029/2007GC001814.

Yao, H., R. D. van der Hilst, and M. V. de Hoop, (2006), Surface-wave array tomography in SE Tibet from ambient seismic noise and two-station analysis - I. Phase velocity maps, *Geophys. J. Int.*, **166**(2), 732-744.

Zhang, J., and X. Yang, (2013). Extracting surface wave attenuation from seismic noise using correlation of the coda of correlation, *J. Geophys. Res. Solid Earth*, **118**, 2191–2205, doi:10.1002/jgrb.50186.

Zhou, L., C. Zhao, Z. Chen, and S. Zheng (2011). Amplitude tomography of *Lg* waves in Xinjiang and its adjacent regions, *Bull. Seismol. Soc. Am.*, **101**, 1302–1314, doi: 10.1785/0120100267.

Zor, E., E. Sandoval, J. Xie, N. Türkelli, B. Mitchell, A. H. Gasanov and G. Yetirmishli (2007). Crustal Attenuation within the Turkish Plateau and Surrounding Region, *Bull. Seismol. Soc. Am.*, **97**, 151-161.

7. ANNEXES

A. Noriega, R. A. Ugalde, A. Villaseñor, and M. J. Jurado (2015). Spatial Variation of *Lg*-wave attenuation in the Iberian Peninsula, *Bull. Seismol. Soc. Am.*, **105**, 420-430.

Bulletin of the Seismological Society of America, Vol. 105, No. 1, pp. 420–430, February 2015, doi: 10.1785/0120140045

Ⓔ

Spatial Variation of *Lg*-Wave Attenuation in the Iberian Peninsula

by Raquel Noriega, Arantza Ugalde, Antonio Villaseñor, and M. José Jurado

Abstract Lateral variations of crustal seismic attenuation across the Iberian Peninsula were estimated by means of an inversion technique applied to 1 Hz $Lg\ Q(Q_0)$ measurements obtained using the two-station method. Seismic data for this study consisted of 59 events with magnitudes $3 \le m_{bLg} \le 5.4$, focal depths less than 30 km, and epicentral distances from 100 to 1000 km, which were recorded by 343 seismic stations between January 2008 and October 2013. *Lg*-wave propagation was found to be inefficient or blocked for most of the paths crossing the Mediterranean Sea, the western Alborán Sea, and the Strait of Gibraltar. Spectral ratios collected over 2480 high-quality interstation paths were used to determine $Lg\ Q_0$ and its frequency dependence (η). $Lg\ Q_0$ estimates range from ~75 to ~800. The lateral variations of $Lg\ Q_0$ correlate well with the major tectonic features of the region and heat flow measurements. The lowest values are found in the Pyrenean range and in eastern and southern Iberia, whereas high $Lg\ Q_0$ values (i.e., lower attenuation) characterize the more stable western part of the Iberian Peninsula. The obtained results are also in agreement with previous studies in the area.

Online Material: Tables of seismic station locations, earthquake parameters, and velocity model, and figures of two-station paths, parameter regression, site amplification analysis at E101, and lateral variation of $Lg\ Q_0$.

Introduction

Lg waves are often the most prominent seismic phases observed over continental paths at regional distances, although they can be observed at distances of ~6000 km in stable continental regions (McNamara and Walter, 2001). They can be modeled as interference phenomena, either between higher-mode surface waves or between multiply reflected, crustal-guided *S* waves (Kennett, 1986). *Lg* phases are generally observed in a group velocity window between 3.6 and 2.8 km/s in a relatively wide frequency band of 0.2–10 Hz (Pasyanos *et al.*, 2009; Singh *et al.*, 2012); they have been used extensively in a variety of studies, such as the determination of earthquake-source parameters (e.g., Nuttli, 1973; Hartse *et al.*, 1997) and variations of crustal attenuative properties (e.g., Benz *et al.*, 1997; Xie *et al.*, 2004; Zor *et al.*, 2007; Mitchell *et al.*, 2008; Phillips and Stead, 2008; Pasyanos *et al.*, 2009; McNamara *et al.*, 2012). *Lg* amplitude is strongly affected by changes in the crustal structure, and apparent attenuation along its path is sensitive to varying tectonic environments (Kennett, 1986; Mitchell, 1995; McNamara and Walter, 2001). The *Lg* phase may be absent on regional seismograms that traverse ocean basins (Zhang and Lay, 1995) because of the quick loss of *Lg* energy in the thin waveguide of the oceanic crust. *Lg* waves are also strongly attenuated across thick sedimentary basins due to the intrinsic absorption effect. Sharp variations in crustal thickness, scattering along tectonic faults and fractures, and variations of the crustal properties (such as partial melting, temperature, or fluid content) are some factors that affect the *Lg*-wave propagation (e.g., Xie *et al.*, 2006).

Lg quality factor *Q*, which is inversely proportional to the *Lg*-wave attenuation rate, is an important parameter for characterizing the Earth's crust. *Lg Q* frequency dependence is often modeled using a power law of the form

$$Q_{Lg}(f) = Q_0 f^{\eta}, \tag{1}$$

in which Q_0 is *Q* at the reference frequency of 1 Hz and η is the frequency dependence exponent, which is assumed constant over the frequencies of interest. It has been generally observed that $Lg\ Q_0$ values are higher in stable continental regions than across active tectonic areas (Xie *et al.*, 2004, 2006).

A number of methods have been proposed to measure Q_{Lg} (Ford *et al.*, 2008). The two-station (TS) method measures *Q* using direct *Lg* waves (Xie and Mitchell, 1990a) by taking the ratio of *Lg* amplitudes recorded at two different stations along the same great circle path from the same event. It is a reliable method that allows removal of the common source term, but it requires strict source–station configuration and dense event and station coverage.

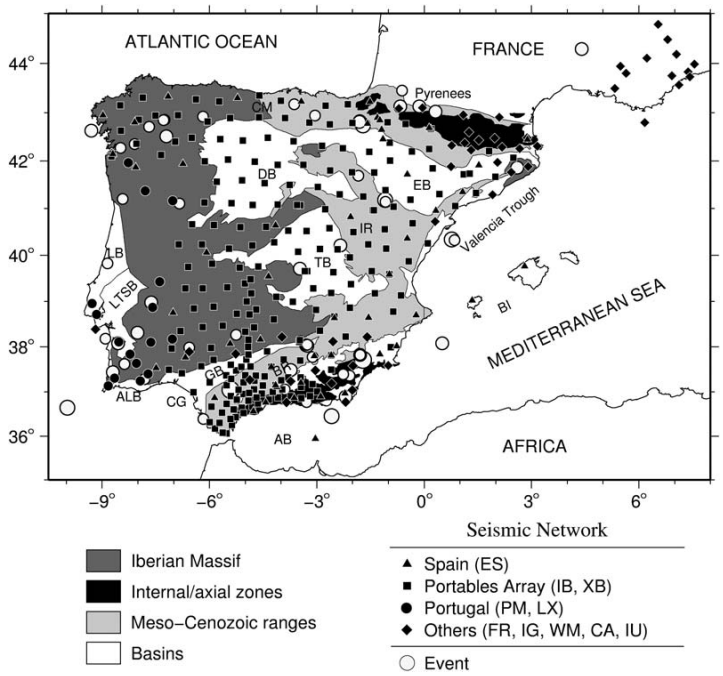

Figure 1. Major tectonic features of the Iberian Peninsula and locations of the seismic stations and earthquakes used in this study. Each network affiliation is plotted with different station symbols, and earthquakes are represented by white dots. AB, Alborán basin; ALB, Algarve basin; BI, Balearic Islands; BR, Betic range; CG, Cádiz Gulf; CM, Cantabrian Mountains; DB, Duero basin; EB, Ebro basin; GB, Guadalquivir basin; IR, Iberian range; LB, Lusitanian basin; LTSB, Lower Tagus-Sado basin; TB, Tagus basin. Modified from Vergés and Fernández (2006).

In recent years, considerable improvements in seismic data quality and geographic coverage have been made by the deployment of new permanent and portable broadband seismic stations in the Iberian Peninsula. This study takes advantage of the dense accumulation of *Lg* waveforms to perform a regionalization of *Lg Q* and its frequency dependence in the Iberian Peninsula using the TS method. *Lg* attenuation was measured in the Granada basin (southern Spain) by De Miguel *et al.* (1992) using the reverse TS method. Calvert *et al.* (2000) mapped the efficiency of *Lg* propagation along the African–Iberian plate boundary zone. Other attenuation studies in the region include the estimation of the anelastic structure of the Iberian Peninsula using Rayleigh waves (e.g., Canas *et al.*, 1988; Lana *et al.*, 1999; Martínez *et al.*, 2005) and coda waves (Payo *et al.*, 1990; Pujades *et al.*, 1990). Because of the limited source–station configuration, these authors presented average results for the peninsula. This article presents the first 2D model for *Lg Q* in the entire region. Results of this study improve the spatial resolution compared with earlier attenuation studies and will help to shed new light on the attenuation properties of the crust of the region. The obtained *Lg* attenuation estimates can be used, for instance, to better quantify the hazard associated with earthquake shaking in the Iberian Peninsula.

Geotectonic Setting

The largest geological feature that extends over most of the western half of the Iberian Peninsula is the Iberian Massif (IM), a stable region that covers one-third of the territory. The IM is bounded to the east and south by the Duero and Tagus Cenozoic basins and to the west and southwest by the lower Tagus-Sado Cenozoic basin and the Lusitanian and Algarve Mesozoic basins (Fig. 1). Meso-Cenozoic ranges, including the Pyrenees, the Iberian range, and the Betic range, are the result of the induced intense crustal deformation that took place from the late Cretaceous to the late Cenozoic at the Iberian margins due to convergence of the European and

African plates. The Alpine chain of the Pyrenees to the northeast of the Iberian Peninsula extends from the Mediterranean Sea to the Atlantic Ocean and is composed of two ranges: the Pyrenees to the east and the Cantabrian Mountains to the west. The Paleozoic core of the Pyrenean range outcrops in the Axial zone. The highest elevations of this area are compensated isostatically by an increased thickness of the continental crust. Its southern foreland Ebro basin was formed by infilling sediments as a result of erosion related to the building of the Pyrenees. Convergence of the African plate formed the Betic range, a Neogene fold belt at the southern margin of Iberia. Mountain ranges in the internal zone of the Betic range are formed predominantly of metamorphic rocks and are surrounded by low-lying sedimentary basins. The flexural response of the lithosphere created the foreland Guadalquivir basin at the northern margin of the Betic range (e.g., Vera, 2004; Vergés and Fernández, 2006).

Within a global context, the Iberian Peninsula is a region of low-to-moderate (M_w <5.5) seismicity. Most of the earthquakes have shallow depths (h < 40 km), although deep events also occur in the southern area. Seismicity concentrates mainly around the southern deformation zone that includes the Betic range, the Alborán basin, and the Cádiz Gulf, where some moderate-to-strong (M_w 6–7) earthquakes have occurred. Seismically active areas also include the Pyrenean range and the northwestern part of the Peninsula.

Data

Waveform data analyzed in this study were collected from 343 broadband seismic stations that belong to a wide variety of sources, such as permanent national and local networks, international seismological organizations, and temporary portable networks. Permanent networks include those operated by the Instituto Geográfico Nacional (IGN, Spain, code ES), Institut Geològic de Catalunya (IGC, Spain, code CA), Instituto Andaluz de Geofísica (IAG, Spain, code IG), Real Instituto y Observatorio de la Armada and Universidad Complutense de Madrid (ROA-UCM, Spain, code WM), RèNaSS and INSU/CNRS (France, code FR), Instituto Português do Mar e da Atmosfera (IPMA, Portugal, code PM), and Instituto Dom Luiz (IDL, Portugal, code LX). Other stations used in this study belong to the Global Seismographic Network (GSN), including Incorporated Research Institutions for Seismology/U.S. Geological Survey stations (code IU). We also used temporary stations of the IberArray (code IB) and Picasso (code XB) passive portable networks. The geographical locations of these seismic stations are listed in Ⓔ Table S1 (available in the electronic supplement to this article) and shown in Figure 1.

The data selection procedure was automated as follows. Using the Spanish Seismic Catalog (IGN), we selected all the shallow events (h < 35 km) with magnitudes m_{bLg} ≥3.1 that occurred within a box defined by longitudes −10° to 4.5° and latitudes 36° to 44° between January 2008 and October 2013. Then, we grouped the events by epicenter into 2.5° × 2.5° cells and selected the three or four best recorded in each cell based on higher magnitude values and larger number of recording stations according to the IGN seismic bulletin. Because of the sparse seismicity distribution in the region, some cells remained empty. The final list included 59 earthquakes with magnitudes $3 \le m_{bLg} \le 5.4$ and epicentral distances from 100 to 1000 km; this list was used to request the vertical-component waveforms and associated instrument responses from the seismic networks considered (Ⓔ Table S2). More than 9800 waveforms were collected in this way.

Method

The TS method (Xie and Mitchell, 1990a) was used in the analysis. It consists of taking the ratio of Lg-amplitude spectra for two different stations aligned with a common source. Denoting the two stations as i and j, the scaled spectral ratio is defined as

$$R(f) = (\Delta_i^{1/2}/\Delta_j^{1/2})[A_i(f)/A_j(f)], \qquad (2)$$

in which Δ_i and Δ_j are the epicentral distances. The square root of their ratio cancels the geometrical spreading effect in 1D (e.g., Xie *et al.*, 2004). $A_i(f)$ and $A_j(f)$ are the Lg-amplitude spectra from the same event at frequency f, so their ratio removes the source term. Assuming the $Lg\,Q$ frequency dependence of equation (1), the following relationship can be derived (Xie and Mitchell, 1990a):

$$\ln\left[\frac{V_{Lg}}{\pi\Delta_{i,j}}\ln(R(f))\right] = (1-\eta)\ln f - \ln Q_0, \qquad (3)$$

in which V_{Lg} is the Lg group velocity, typically 3.5 km/s. Using equation (3), $Lg\,Q_0$ and η over the interstation distance $\Delta_{i,j}$ can be estimated by means of a linear regression.

Because a geometry in which the TS pairs and the source are aligned perfectly is usually not possible, a difference between the azimuths from the source to the two stations $(\delta\theta)_{max}$ is allowed in practical analysis. This value is required to be small to minimize the errors in the estimated $Lg\,Q_0$ and η values resulting from the introduction of effects of Lg attenuation outside the path and nonisotropic source radiation pattern. According to Der *et al.* (1984) and Xie *et al.* (2004), a maximum allowable value of $(\delta\theta)_{max}$ is ±15°.

$Lg\,Q_0$ estimations may be also affected by modeling errors not accounted for in the TS method, such as complex ray deflections, focusing, and defocusing in 3D media and nonunity site responses. Following Xie *et al.* (2004), the total error may be quantified by a factor of $1+\delta x$. For small δx values, the relative error in $Lg\,Q_0$ estimations is related to the interstation distance $\Delta_{i,j}$ by

$$\delta Q_0/Q_0 \approx 1.1(Q_0/\Delta_{i,j})\delta x. \qquad (4)$$

Interstation distances $\Delta_{i,j}$ as large as possible are then required to keep the error in $Lg\,Q_0$ estimates low (Xie *et al.*, 2004).

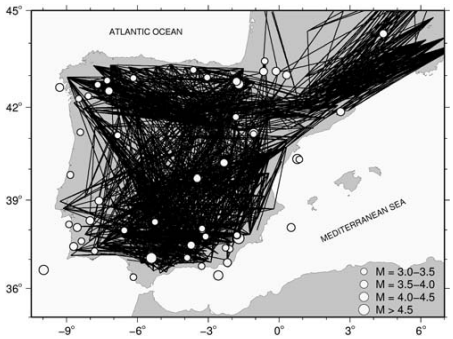

Figure 2. Two-station (TS) paths and epicenters of the earthquakes used to estimate *Lg* attenuation in this study.

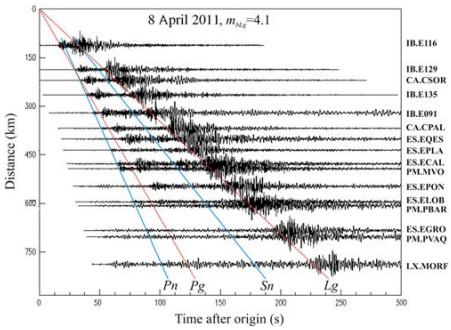

Figure 3. Record section of the 8 April 2011 m_{bLg} 4.1 earthquake (Ⓔ Table S1) recorded at 16 stations of ES, IB, CA, PM, and LX networks (Ⓔ Table S2). The waveforms are filtered in the band of interest (0.5–5 Hz). The Instituto Geográfico Nacional model travel times for the Iberian Peninsula are shown for *Pn*, *Pg*, *Sn*, and *Lg* waves (Ⓔ Table S3). The color version of this figure is available only in the electronic edition.

Interstation $Lg\,Q_0$ and η Determination

We only analyzed vertical-component *Lg* recordings to avoid confusion with fundamental-mode Love-wave energy on the transverse components (Fan and Lay, 2003). First, we removed the instrument response and windowed the *Lg* phase with a 20% cosine taper using group velocities of 3.5–2.9 km/s for all the paths except those crossing the Pyrenean range, for which more accurate values of 3.4–2.8 km/s were recognized after visually inspecting all seismograms. Similarly, we selected a time window after the *Pn* onset, starting at 8.3 km/s and having the same length as the *Lg* window. Then, we applied the fast Fourier transform to the two windows and smoothed the amplitudes by means of a 50% overlapped, 15-point moving window in the frequency domain. As a threshold for assuring the existence of an *Lg* phase, we only kept those *Lg* spectral amplitudes $A(f)$ greater than four times the *Pn* window spectral amplitudes for further analysis.

The TS combinations were chosen so that they were aligned with the source using an angle of $(\delta\theta)_{\max} = \pm 15°$, as explained in the previous section. Then, we calculated the ratios of *Lg* spectra and epicentral distances for every TS path using equation (2) and estimated $Lg\,Q_0$ and η by means of a linear regression using equation (3). Only estimates with correlation coefficients of the fit greater than 0.7 were kept. Thereafter, we considered the criterion of minimum interstation distances $\Delta_{i,j}$ according to equation (4). If we assume the modeling error δx to be 0.2, the ratio between Q_0 and $\Delta_{i,j}$ should be less than 1.6 to keep this error lower than 35% (Xie *et al.*, 2004; Zor *et al.*, 2007). In this work, the minimum interstation distance considered was 225 km. In addition to all the previous selection criteria, the remaining paths after the processing then were manually reviewed to ensure the quality of the measurements. From the initial dataset of 9800 seismograms, we obtained final estimates for 2480 interstation paths (Fig. 2). Figure 3 plots a record section of an earthquake used in our study, showing the synthetic travel times for *Pn*, *Pg*, *Sn*, and *Lg* waves according to the IGN model for the Iberian Peninsula (Ⓔ Table S3).

Figure 4 shows examples of vertical-component waveforms band-pass filtered between 0.5 and 5 Hz for some paths across different geologic regions. The first TS paths are located inside the Iberian Peninsula. They show predominant *Lg* energy in a window defined by group velocities from 3.5 to 2.9 km/s. Station pair XIII–E077 (Fig. 4b) corresponds to an event located in the Pyrenean range, and it crosses the eastern part of the peninsula. The path E031–EMAZ (Fig. 4c) crosses the western part of the IM, which is characterized by a stable crust. The third TS pair corresponds to an earthquake that occurred in Morocco. We observe a decrease of *Lg* energy along the PM19–PS39 interstation path (Fig. 4d). Such *Lg* characteristics for paths crossing the Alborán basin were noticed by Calvert *et al.* (2000) and McNamara and Walter (2001). Calvert *et al.* (2000) carried out a regional seismic phases (*Lg* and *Sn*) propagation study along the African–Iberian plate boundary and demonstrated that *Lg* propagation is usually inefficient (*Lg* amplitude on the order of the *Pg* arrival) or even blocked (*Lg*/*Pg* ratio < 1.0) for paths crossing the western Alborán basin and eastern Iberia beneath the Mediterranean Sea. In this study, we observed that most of the *Lg* paths from earthquakes that occurred in northern Africa, and were recorded by stations in the Iberian Peninsula, became blocked or inefficient. In the same way, paths from events in Iberia that were recorded by seismic stations in northern Africa did not show efficient *Lg* recordings. We also noticed the absence of *Lg* phases in recordings from stations located in the Balearic Islands. For these reasons, we restricted the study region in this article to the Iberian Peninsula.

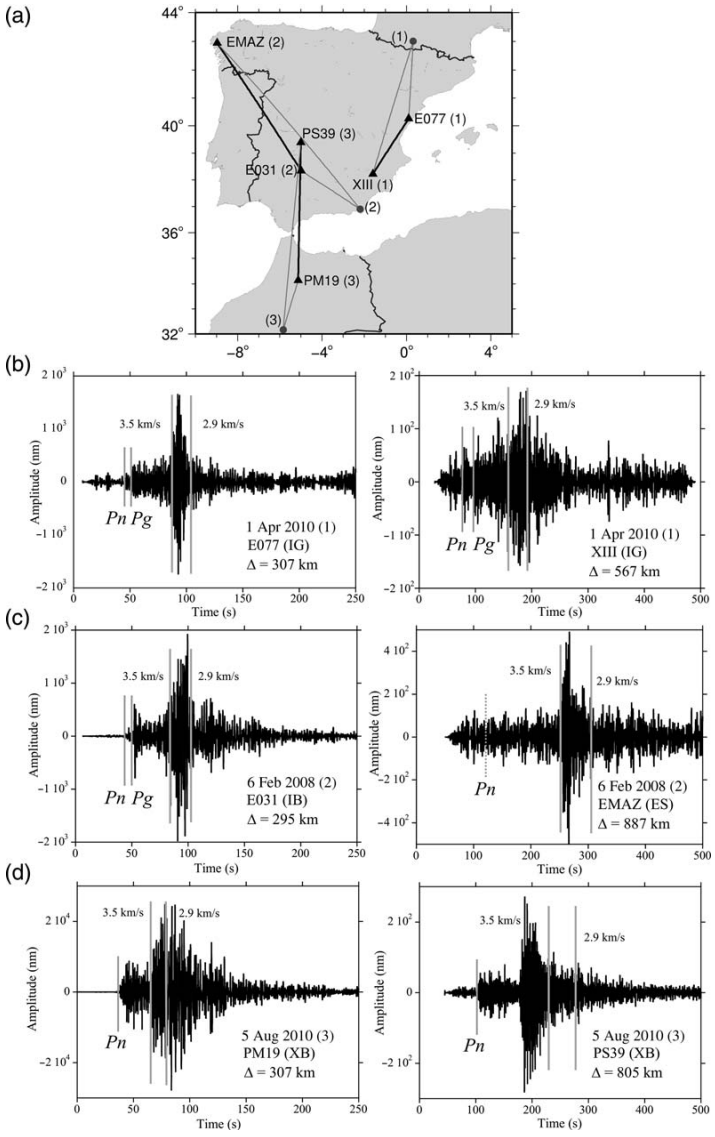

Figure 4. (a) Examples of stations (triangles), epicentral locations (dots), TS paths (black lines), and event-to-station paths (gray lines) used in this study. Events and their related paths are labeled with the same numbers. Some examples of *Lg* band-pass filtered (0.5–5 Hz) waveforms along different propagation paths: (b) E077–XIII, (c) E031–EMAZ, and (d) PM19–PS39. Vertical gray lines mark the observed (solid line) or expected (dotted line) *P*-wave arrivals and the *Lg* group velocity window (3.5–2.9 km/s) used. Corresponding path number, event date, station name, and epicentral distance are also indicated. The vertical scale is fixed to the peak amplitude for each seismogram.

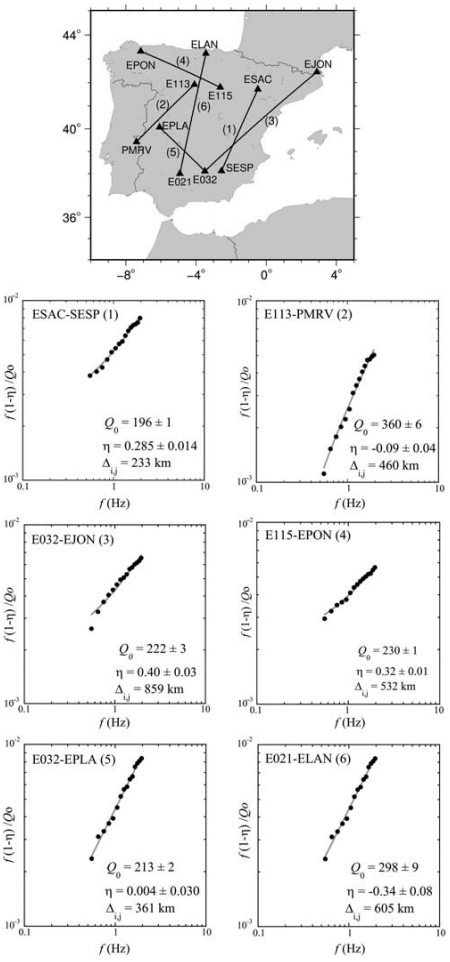

Figure 5. (Top) Location of the paths and (bottom) examples of the linear regression fit performed to determine $Lg\,Q_0$ and η values and their standard errors. The TS names and associated interstation distances are shown.

Figure 5 shows examples of the linear regression fitting using equation (3) for the frequency band 0.5–2 Hz. The high cut-off frequency was chosen because a significant loss of linearity (flattening of the spectra) was observed at large distances above this value. Fan and Lay (2002, 2003) explained a similar observation in the Tibetan Plateau as being caused by high-frequency *Sn* coda appearing in the *Lg* window at large distances.

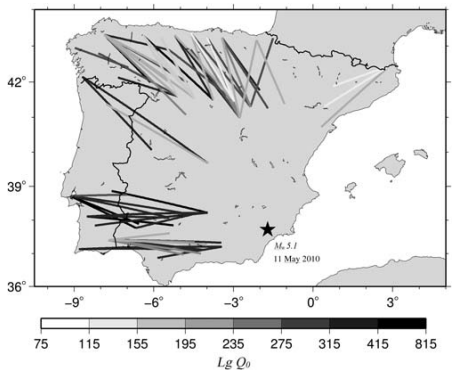

Figure 6. Examples of the TS paths used in this study corresponding to the M_w 5.1 Lorca earthquake on 11 May 2011 (star). The scale indicates the estimated $Lg\,Q_0$ values for each path.

Figure 6 shows one example of TS paths used in this study. They correspond to the M_w 5.1 Lorca earthquake on 11 May 2011. The $Lg\,Q_0$ values estimated for the paths tend to be coherent on a large scale. Nevertheless, two paths of $Lg\,Q_0$ estimations lower than the overall trend are observed in the north-central region, both having a common point at station E101 (Ⓔ Fig. S1a). Ⓔ Figure S1b shows a comparison of the linear regression fits performed to estimate $Lg\,Q_0$ and η for the overlapping paths E101–E155 and E093–155. The spectral ratios have a similar shape, but the *Lg* amplitudes measured at station E101 are greater than the values for station E093 at all frequencies. The amplitude differences are also observed for other stations surrounding E101, as plotted in Ⓔ Figure S1c, and may be related to site effects. To check for azimuthal variations in site amplification, we plotted the amplitude residuals relative to station E093 for different events against back azimuth (Ⓔ Fig. S2). No clear azimuthal dependence is observed in this figure, which reduces the possibility that the observed amplification is mainly caused by lateral focusing or defocusing effects (e.g., Barker *et al.*, 1981). These observations illustrate a possible source of systematic errors contained in the $Lg\,Q_0$ estimations. In this case, the geological structures under station E101 are thought to be responsible for the observed site amplifications, which are not accounted for in the TS method.

Spatial Variations of $Lg\,Q_0$

Once the $Lg\,Q_0$ values were obtained for all the $i = 1, \ldots, M$ paths shown in Figure 2, the lateral variations of the attenuation parameters were mapped using inversion (e.g., Xie and Mitchell, 1990b). If we divide the study region into $j = 1, \ldots, N$ cells, the attenuation measured over the ith path can be expressed as the sum of the attenuation of the

individual cells the path intersects. Moreover, one cell will be crossed by several paths that correspond to different values of $Lg\,Q_0$. The observational equation can be expressed as

$$\Delta_i Q_i^{-1} = \sum_{j=1}^{N} w_{ij} Q_j^{-1}, \qquad i = 1, \ldots, M, \tag{5}$$

in which Δ_i and Q_i^{-1} are the distance and Q_0^{-1} along the ith path, respectively. The length of the ith path into the jth cell is denoted as w_{ij}, and Q_j^{-1} is the Q_0^{-1} value inside the jth cell to be inverted for. Equation (5) is equivalent to a matrix equation of the form

$$\mathbf{p} = \mathbf{W} \times \mathbf{f}, \tag{6}$$

in which $\mathbf{p}$ is the column vector $\Delta_i Q_i^{-1}$, $i = 1, \ldots, M$; $\mathbf{f}$ is the column vector Q_j^{-1}, $j = 1, \ldots, N$; and $\mathbf{W}$ is the matrix w_{ij}, $i = 1, \ldots, M$; $j = 1, \ldots, N$.

To solve systems of equations such as (6), there exist some powerful iterative methods that have been commonly used in seismic tomography, such as the simultaneous iterative reconstruction technique (SIRT) or the conjugate gradient method. In this work, we use the SIRT, which is a sequential algorithm that converges toward a least-squares solution after rescaling the original equation to be solved. To use this method, it is necessary to make an arbitrary initial guess of the solution as $\mathbf{f}^0 = (f_1^0, f_2^0, \ldots, f_N^0)$. Then, the iteration process is described as

$$\Delta f_i^{(k)} = f_i^{(k)} - f_i^{(k-1)} = \frac{1}{\sum_i w_{ij}} \sum_i \left[w_{ij} \frac{p_i - \sum_{l=1}^{N} w_{il} f_l^{(k)}}{\sum_{l=1}^{N} w_{il}} \right], \quad i = 1, \ldots, M \tag{7}$$

(e.g., Andersen and Kak, 1984), in which k is the iteration number and the summation with respect to i is over the rays intersecting the jth cell. The SIRT algorithm computes the correction $\Delta\mathbf{f}^{(k)}$ for each cell. Then, the next solution $\mathbf{f}^{(k)}$ is changed from the preceding one $\mathbf{f}^{(k-1)}$ by the addition of the average $\Delta\mathbf{f}^{(k)}$ correction after one iteration step is completed (when all the equations have been considered once).

We constructed the grid by dividing the regions into $N = 3944$ cells of dimensions $0.25° \times 0.25°$ for $M = 2480$ equations. Then, we calculated the paths by assuming straight trajectories and calculated the w_{ij} coefficients of the system of equation (5). Because the method requires a good starting model (e.g., Wéber, 2000), in our case we assigned a mean initial value of $Q_j^{-1} = 0.005$ to all the $\mathbf{f}^0$. This choice is based on the large-scale estimates for the Iberian Peninsula plotted by Mitchell *et al.* (2008) in their Lg coda Q_0 maps across Eurasia. To increase the general stability of the inversion process, the solution was smoothed by a 3×3 median filter after each iteration step. We also calculated the root mean square error ε between the current and last solution at each iteration step and selected a threshold value of $\varepsilon \leq 10^{-5}$ as the stopping criterion, which in our case was reached at about 34 iterations.

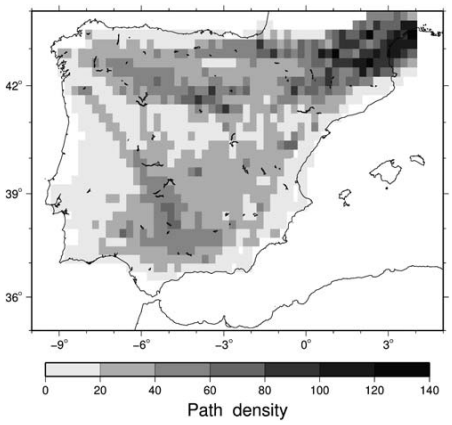

Figure 7. Hit counts or number of times each cell is sampled by the interstation paths. The darker areas are the more sampled zones.

The reliability of the solution may be affected by sampling insufficiencies for the defined grid. Figure 7 shows the hit count that measures the number of times each cell is crossed by the TS paths. The entire region is well sampled. The obtained laterally varying $Lg\,Q_0$ model is plotted in Figure 8.

To check the 15° source-to-station azimuth constraint, we repeated the analysis for a $(\delta\theta)_{\max}$ value of ±8°. The number of paths was dramatically reduced by 46%; however, but the inversion process was still possible, and we obtained similar results for the $Lg\,Q_0$ model (Ⓔ Figs. S3 and S4).

The standard deviation of $Lg\,Q_0$ mapped in Figure 9 was estimated by resampling the original dataset using the delete-j jackknife technique (e.g., Erickson *et al.*, 2004). We removed $\sqrt{n}$ randomly selected observations from the total n number of Q_0 measures to create 1000 jackknife datasets. Then, we inverted each dataset to estimate 1000 new models, from which we calculated the mean and standard deviation of $Lg\,Q_0$. The standard deviation estimated is less than 20% throughout the region.

We also tested the resolution of the inversion method by synthesizing Q^{-1} from the system of equations (5) using a given test distribution of the attenuation parameters and the same event and station configuration used in the analysis. We generated a checkerboard pattern with $2.5° \times 2.5°$ high-attenuation ($Q_0 = 10$) and low-attenuation ($Q_0 = 1000$) cells (Fig. 10a). Then, the synthesized parameters were inverted using SIRT. Figure 10b shows the attenuation structures are reasonably well resolved from the inversion.

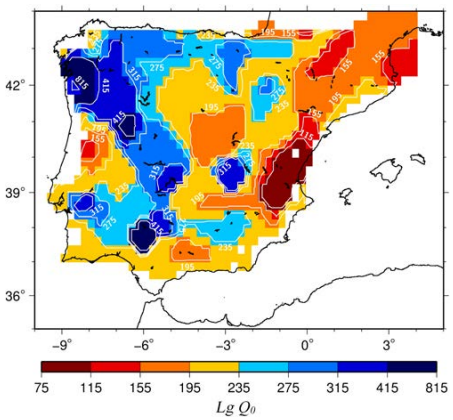

Figure 8. Lateral variation of $Lg\ Q_0$ in the Iberian Peninsula. Lower values of Q represent zones with higher attenuation. The color version of this figure is available only in the electronic edition.

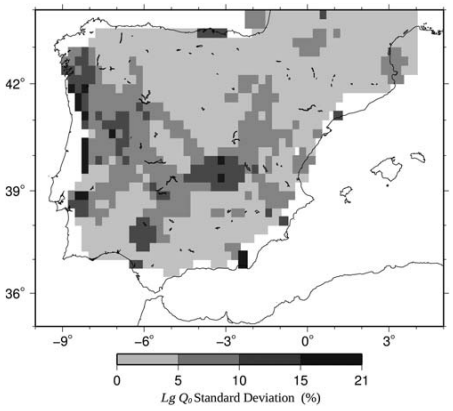

Figure 9. Standard deviation of $Lg\ Q_0$ in the Iberian Peninsula, estimated using a delete-j jackknife resampling technique.

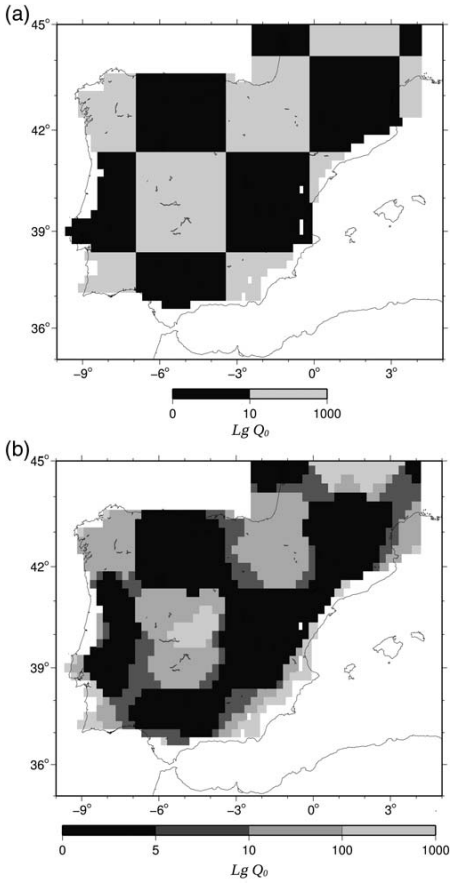

Figure 10. (a) Checkerboard synthetic test model and (b) obtained spatial variation of the synthetic attenuation model using the simultaneous iterative reconstruction technique algorithm.

Discussion

In this study, we processed a large set of new broadband waveform data to obtain the spatial variations of $Lg\ Q_0$ in the Iberian Peninsula. The resulting map plotted in Figure 8 reflects $Lg\ Q_0$ values ranging from ∼75 to ∼800. The large variations in Q_0 values across the Iberian Peninsula are a consequence of the different geologic and tectonic characteristics of the region (Fig. 1). The most striking feature is the contrast between the higher values in the western Iberian Peninsula that are associated with the stable crust of the IM and the lower estimates in the Pyrenean range and eastern Iberia, where seismic activity levels are relatively high. Regions of concentrated seismic activity display low Q_0 values (e.g., Mitchell, 1995; McNamara *et al.*, 2012). This fact could be related to the effect of scattering attenuation due to the presence of tectonic complexity and small-scale structural heterogeneities. Also, stable regions show relatively high Q_0 values, and areas with moderate seismicity are usually associated with intermediate Q_0 observations.

The Pyrenean range shows Q_0 values that are lower in the central part than in the eastern and western sections. These observations may be related to variations of the crustal structure along the Pyrenean axis. However, at the low frequencies analyzed in this work, we do not observe the strongly attenuating area (*Lg* blockage) noticed by Sens-Schönfelder *et al.* (2009) in the western Pyrenees in a higher frequency range (2–4 Hz) over long paths (600–950 km).

The eastern part of the Iberian Peninsula exhibits low Q_0 values as well. In the Valencia trough toward the Mediterranean Sea, the crustal thickness changes abruptly, thus causing the blockage of *Lg* waves. The southwestern border of the IM displays a lower Q_0 value related to the presence of the Algarve sedimentary basin. The southern part of the IM is bounded by the Guadalquivir basin where *Lg* attenuation is also high, as well as in the Betic range and the central zones of the Peninsula, in the Tagus basin.

Low $Lg\ Q_0$ values have been correlated with high heat flow measurements (e.g., Mitchell, 1995; Gallegos *et al.*, 2014). In this work, we also compared our $Lg\ Q_0$ model with the heat flow map of the Iberian Peninsula of Fernández *et al.* (1998) and the surface heat flow density map at European scale included in the *Atlas of Geothermal Resources in Europe* (Hurter and Haenel, 2002). These maps show a correspondence between high heat flow measurements (>70 mW/m^2) and high attenuation in the central and western Pyrenees, the Tagus basin, and the eastern Iberian Peninsula. These results suggest that *Lg* attenuation may be affected by high crustal temperatures in these regions.

The $Lg\ Q_0$ general patterns found in this study correlate well with previous works on coda Q in the Iberian Peninsula. Pujades *et al.* (1990) found the lowest Q_0 values in the southeastern part of Iberia and in the Pyrenean domain, whereas the highest Q_0 values were observed in the northwest. These attenuation results were supported by the work of Payo *et al.* (1990), who showed that lower Q values were located in the internal–external units of the Betics and in the Pyrenean range, whereas high Q observations corresponded to the northwestern region, in the IM. Very few studies on *Lg* attenuation have been performed in the Iberian Peninsula. Applying the reverse TS method (Chun *et al.*, 1987), De Miguel *et al.* (1992) found $Lg\ Q_0 \sim 100$ for the Granada basin. Mitchell *et al.* (2008) obtained an $Lg\ Q_0$ map using a grid of $3° \times 3°$ for Eurasia and estimated low Q_0 values (200–300) for Spain, which is in agreement with the average $Q_0 \sim 265$ estimation for the whole Iberian Peninsula of this work.

By comparing the *Lg* attenuation values of the Iberian Peninsula with those of other regional areas, we found the Q_0 values in this study are higher than those observed by Phillips and Stead (2008) in the western United States. Their Q values ranged between 60 and 550, whereas most of the region was associated with high attenuation ($Q < 150$). Other attenuation models with lower Q_0 values have been obtained in the Tibetan Plateau and adjacent areas by several researchers. Fan and Lay (2002, 2003) observed strong *Lg*-wave attenuation ($Q_0 \sim 80$–90) in northern central Tibet, decreasing to the south to $Q_0 \sim 300$. Their results are in agreement with those of Phillips *et al.* (2000), who obtained $Q_0 \sim 200$ within the Tibetan plateau, whereas relative high Q_0 values were found in the Tarim basin ($Q_0 \sim 500$). The highest values ($Q_0 > 800$) were observed in the stable platform and older crust. This low attenuation is similar to that estimated in this work for the IM. Pasyanos *et al.* (2009) characterized the *Lg* attenuation in the Middle East and obtained a similar range of values to the observations in the present study. As in western Iberia, very low attenuation ($Q_0 > 800$) was obtained in the Arabian and Indian Shields and low attenuation ($Q_0 = 400$–600) was obtained in the Arabian and Kazakh Platforms. These results are consistent with Zor *et al.* (2007), who found $Q_0 = 300$–800 in the Arabian platform and inefficient *Lg* propagation through the southeastern Mediterranean. High attenuation ($Q_0 = 200$–300) was observed along the Zagros Mountains and across areas of the Red Sea and Gulf of Aden rifts with similar values to those obtained across Spain.

As for the frequency-dependence exponent, according to Xie *et al.* (2004) a wide frequency range should be desirable to obtain stable measurements of η. In this study, we used the relatively narrow 0.5–2 Hz frequency range and observed that most of the values are between 0.3 and 0.6, with a maximum of 0.9. In some cases, however, η was very low or even negative. These observations could be caused by the limited frequency range used to compute η (e.g., McNamara and Walter, 2001). In this work, we are not able to observe a consistent pattern of η with high or low Q_0 measurements.

Although it is a reliable approach, the effects of 3D velocity structures may affect the *Lg* amplitudes, thus resulting in errors in $Lg\ Q_0$ estimates by means of the TS method. The reversed TS procedure (Chun *et al.*, 1987) further allows the cancellation of site responses, but it requires even more strict recording geometries. In this work, the station and event coverages did not allow the reversed TS method to be applied. Studying these effects is beyond the scope of this article, but it must be addressed in the future to improve the interpretations made in this work.

Conclusions

In this study, we obtained the first regional map that images the spatial variations of $Lg\ Q_0$ in the Iberian Peninsula. Using the TS method with a large dataset, our results correlated well with the main geotectonic characteristics of the study region and heat flow measurements. Significant lateral Q_0 variations were found in the area, with values between ~75 to ~800. The higher estimates are related to the stable IM in western Iberia, whereas the lower values are associated with the Pyrenean range and some areas in western, southern, and eastern Iberian Peninsula where sedimentary basins exist and/or seismic activity is relatively important. A high-attenuation area was also found in the Tagus basin, in central Iberia. The *Lg* propagation was found inefficient or blocked through the Strait of Gibraltar and adjacent areas and across the deep

ocean basin of the Mediterranean Sea. Future studies are needed to determine the influence of station site responses on the attenuation estimates.

Data and Resources

Seismic data were obtained from the Instituto Geográfico Nacional (IGN, Spain), Institut Geològic de Catalunya (IGC, Spain), Instituto Andaluz de Geofísica (IAG, Spain), Real Instituto y Observatorio de la Armada and Universidad Complutense de Madrid (ROA-UCM, Spain), RèNaSS (Strasbourg, France), National Institute for Earth Sciences and Astronomy (INSU)/Centre National de la Recherche Scientifique (CNRS) (Paris, France), Instituto Português do Mar e da Atmosfera (IPMA, Portugal), Instituto Dom Luiz (IDL, Portugal), Global Seismographic Network (GSN) and the Picasso/Passive portable network. Some figures were made with the Generic Mapping Tools (Wessel and Smith, 1998).

Acknowledgments

We are very grateful to Associate Editor Michel Bouchon, Tom Hearn, and an anonymous reviewer for constructive comments that contributed to improve the paper. R. Noriega was funded by the Spanish government through the Formación de Personal Investigador (FPI) Ph.D. Grant (BES-2011-044291). A. Ugalde was funded by REPSOL CO-DOS project. This is a contribution of Team Consolider-Ingenio 2010 TOPO-IBERIA (CSD2006-00041) and the MICINN Project CGL2010-21568.

References

Andersen, A. H., and A. C. Kak (1984). Simultaneous algebraic reconstruction technique (SART): A superior implementation of the ART algorithm, *Ultrason. Imag.* **6,** 81–94.

Barker, B. W., Z. A. Der, and C. P. Mrazek (1981). The effect of crustal structure on the regional phases *Pg* and *Lg* at the Nevada test site, *J. Geophys. Res.* **86,** 1686–1700, doi: 10.1029/JB086iB03p01686.

Benz, H., A. Frankel, and D. Moore (1997). Regional *Lg* attenuation for the continental United States, *Bull. Seismol. Soc. Am.* **87,** 606–619.

Calvert, A., E. Sandoval, D. Seber, M. Baranzangi, F. Vidal, G. Alguacil, and N. Jabour (2000). Propagation of regional seismic phases (*Lg* and *Sn*) and *Pn* velocity structure along the Africa-Iberia plate boundary zone: Tectonic implications, *Geophys. J. Int.* **142,** 384–408.

Canas, J. A., F. de Miguel, F. Vidal, and G. Alguacil (1988). Anelastic Rayleigh wave attenuation in the Iberian Peninsula, *Geophys. J. Int.* **95,** 391–396.

Chun, K.-Y., G. F. West, R. J. Kokoski, and C. Samson (1987). A novel technique for measuring Lg attenuation. Results from eastern Canada between 1 to 10 Hz, *Bull. Seismol. Soc. Am.* **77,** 398–419.

De Miguel, F., J. M. Ibáñez, G. Alguacil, J. A. Canas, F. Vidal, J. Morales, J. A. Peña, A. M. Posadas, and F. Luzón (1992). 1–18 Hz *Lg* attenuation in the Granada basin (southern Spain), *Geophys. J. Int.* **111,** 270–280.

Der, Z., M. E. Marshall, A. O'Donnell, and T. W. McElfresh (1984). Spatial coherence structure and attenuation of the *Lg* phase, site effects and the interpretation of the *Lg* coda, *Bull. Seismol. Soc. Am.* **74,** 1125–1147.

Erickson, D., D. E. McNamara, and H. M. Benz (2004). Frequency-dependent *Lg Q* within the continental United States, *Bull. Seismol. Soc. Am.* **94,** 1630–1643, doi: 10.1785/012003218.

Fan, G. W., and T. Lay (2002). Characteristics of *Lg* attenuation in the Tibetan plateau, *J. Geophys. Res.* **107,** no. 10, 2256, doi: 10.1029/2001JB000804.

Fan, G. W., and T. Lay (2003). Strong *Lg* wave attenuation in the northern and eastern Tibetan plateau measured by a two-station/two-event stacking method, *J. Geophys. Res.* **30,** no. 10, 1530, doi: 10.1029/2002GL016211.

Fernández, M., I. Marzán, A. Correia, and E. Ramalho (1998). Heat flow, heat production, and lithospheric thermal regime in the Iberian Peninsula, *Tectonophysics* **291,** 29–53, doi: 10.1016/S0040-1951(98)00029-8.

Ford, S. R., D. S. Dreger, K. Mayeda, W. R. Walter, L. Malagnini, and W. S. Phillips (2008). Regional attenuation in northern California: A comparison of five 1D *Q* methods, *Bull. Seismol. Soc. Am.* **98,** 2033–2046, doi: 10.1785/0120070218.

Gallegos, A., N. Ranasinghe, J. Ni, and E. Sandvol (2014). *Lg* attenuation in the central and eastern United States as revealed by the EarthScope Transportable Array, *Earth Planet. Sci. Lett.* **402,** 187–196, doi: 10.1016/j.epsl.2014.01.049.

Hartse, H. E., S. R. Taylor, W. S. Phillips, and G. E. Randall (1997). A preliminary study of regional seismic discrimination in central Asia with emphasis on western China, *Bull. Seismol. Soc. Am.* **87,** 551–568.

Hurter, S. and R. Haenel (Editors) (2002). *Atlas of Geothermal Resources in Europe*, Publication No. EUR 17811 of the European Commission, Office for Official Publications of the European Communities, L-2985 Luxembourg.

Kennett, B. L. N. (1986). *Lg* waves and structural boundaries, *Bull. Seismol. Soc. Am.* **76,** 1133–1141.

Lana, X., O. Caselles, J. A. Canas, J. Badal, L. Pujades, and M. D. Martínez (1999). Anelastic structure of the Iberian Peninsula from an automated regionalization algorithm and stochastic inversion, *Tectonophysics* **304,** 219–239.

Martínez, M. D., X. Lana, O. Caselles, J. A. Canas, and L. Pujades (2005). Elastic-anelastic regional structures for the Iberian Peninsula obtained from Rayleigh wave tomography and causal uncoupled inversion, *Pure Appl. Geophys.* **162,** doi: 10.1007/s00024-005-2778-4.

McNamara, D. E., and W. Walter (2001). Mapping crustal heterogeneity using *Lg* propagation efficiency throughout the Middle East, Mediterranean, southern Europe and northern Africa, *Pure Appl. Geophys.* **158,** 1165–1188.

McNamara, D., M. Meremonte, J. Z. Maharrey, S.-L. Mildore, J. R. Altidore, D. Anglade, S. E. Hough, D. Given, H. Benz, L. Gee, and A. Frankel (2012). Frequency-dependent seismic attenuation within the Hispaniola Island region of the Caribbean Sea, *Bull. Seismol. Soc. Am.* **102,** 773–782, doi: 10.1785/0120110137.

Mitchell, B. J. (1995). Anelastic structure and evolution of the continental crust and upper mantle from seismic surface wave attenuation, *Rev. Geophys.* **33,** 441–462.

Mitchell, B. J., L. Cong, and G. Ekström (2008). A continent-wide map of 1-Hz *Lg* coda *Q* variation across Eurasia and its relation to lithospheric evolution, *J. Geophys. Res.* **113,** no. B04303, doi: 10.1029/2007JB005065.

Nuttli, O. W. (1973). Seismic waves attenuation and magnitude relations for eastern North America, *J. Geophys. Res.* **78,** 876–885.

Pasyanos, M. E., E. M. Matzel, W. R. Walter, and A. J. Rodgers (2009). Broadband *Lg* attenuation modeling in the Middle East, *Geophys. J. Int.* **177,** 1166–1176.

Payo, G., J. Badal, J. A. Canas, V. Corchete, L. Pujades, and F. J. Serón (1990). Seismic attenuation in Iberia using the coda-*Q* method, *Geophys. J. Int.* **103,** 135–145.

Phillips, W., and R. Stead (2008). Attenuation of *Lg* in the western US using the USArray, *Geophys. Res. Lett.* **35,** L07307, 1–5.

Phillips, W., H. E. Hartse, S. R. Taylor, and G. E. Randall (2000). 1 Hz *Lg Q* tomography in central Asia, *Geophys. Res. Lett.* **20,** 3425–3428.

Pujades, L. G., J. A. Canas, J. J. Egozcue, M. A. Puigví, J. Gallart, X. Lana, J. Pous, and A. Casas (1990). Coda-*Q* distribution in the Iberian Peninsula, *Geophys. J. Int.* **100,** 285–301.

Sens-Schönfelder, C., L. Margerin, and M. Campillo (2009). Laterally heterogeneous scattering explains *Lg* blockage in the Pyrenees, *J. Geophys. Res.* **114,** no. B07309, doi: 10.1029/2008JB006107.

Singh, C., M. Shekar, A. Singh, and R. K. Chadha (2012). Seismic attenuation characteristics along the Hi-CLIMB profile in Tibet from *Lg Q*

inversion, *Bull. Seismol. Soc. Am.* **102,** 783–789, doi: 10.1785/0120110145.

Vera, J. A. (Editor) (2004). *Geología de España*, SGE-IGME, Madrid, Spain, 884 pp.

Vergés, J., and M. Fernàndez (2006). Ranges and Basins in the Iberian Peninsula: Their contribution to the present topography, in *European Lithosphere Dynamics*, D. Gee and R. Stephenson (Editors), Geol. Soc. Am. Memoir, Vol. 32, 223–234.

Wéber, Z. (2000). Seismic traveltime tomography: A simulated annealing approach, *Phys. Earth Planet. In.* **119,** 149–159.

Wessel, P., and W. H. F. Smith (1998). New, improved version of generic mapping tools released, *Eos Trans. AGU* **79,** no. 47, 579–579, doi: 10.1029/98EO00426.

Xie, J., and B. J. Mitchell (1990a). Attenuation of multiphase surface waves in the Basin and Range Province. I. *Lg* and *Lg* coda, *Geophys. J. Int.* **102,** 121–137.

Xie, J., and B. J. Mitchell (1990b). A back projection method for imaging large-scale lateral variation in *Lg* coda *Q* with application to continental Africa, *Geophys. J. Int.* **100,** 161–181.

Xie, J., R. Gok, J. Ni, and Y. Aoki (2004). Lateral variation of crustal seismic attenuation along the INDEPTH profiles in Tibet from *Lg Q* inversion, *J. Geophys. Res.* **109,** no. B10308, doi: 10.1029/2004JB002988.

Xie, J., Z. Wu, R. Liu, D. Schaff, Y. Liu, and J. Liang (2006). Tomographic regionalization of crustal *Lg Q* in eastern Eurasia, *J. Geophys. Res.* **33,** L03315, doi: 10.1029/2005GL024410.

Zhang, T., and T. Lay (1995). Why the *Lg* phase does not traverse oceanic crust, *Bull. Seismol. Soc. Am.* **85,** 1665–1678.

Zor, E., E. Sandoval, J. Xie, N. Türkelli, B. Mitchell, A. H. Gasanov, and G. Yetirmishli (2007). Crustal attenuation within the Turkish Plateau and surrounding region, *Bull. Seismol. Soc. Am.* **97,** 151–161.

Instituto de Ciencias de la Tierra Jaume Almera–Consejo
Superior de Investigaciones Científicas
Lluís Solé i Sabarís, s/n
08028 Barcelona, Spain
rnoriega@ictja.csic.es
augalde@ictja.csic.es
antonio@ictja.csic.es
mjjurado@ictja.csic.es

Manuscript received 20 February 2014;
Published Online 2 December 2014

Electronic Supplement to

Spatial Variation of *Lg*-Wave Attenuation in the Iberian Peninsula

by Raquel Noriega, Arantza Ugalde, Antonio Villaseñor, and M. José Jurado

The electronic supplement contains tables of seismic station locations, earthquake parameters, and velocity model and figures of two-station paths, parameter regression, site amplification analysis at E101, and lateral variation of *Lg* Q_0.

Tables

Standard Velocity Model and Geographic Information on the Seismic Stations and Earthquakes

The three supplemental tables contain information on the seismic stations' locations and earthquake parameters used in the analysis, as well as the standard velocity model used for the Iberian Peninsula.
Table S1. Seismic stations and geographic locations used in the analysis. The network codes are indicated.
Table S2. Earthquakes used in the analysis. The geographic locations are from the Spanish National Geographic Institute catalog. The event marked with an asterisk was plotted in Figure 4 but was not used in the analysis.
Table S3. Velocity model used by the Spanish National Geographic Institute (IGN) for routine earthquake locations in the Iberian Peninsula.

Figures

Test of Site Amplification Effects on the *Lg* Q_0 Estimations

In the supplemental figures, *Lg* amplitudes for close paths are analyzed in order to check for a possible site amplification effect at station E101.
Figure S1. (a) Location of the two-station paths yielding different *Lg* Q_0 values (E101–E154, E093–E154, E101–E155, and E093–E155) and surrounding stations; (b) examples of the linear regression fits performed to determine *Lg* Q_0 and frequency dependence η values for the almost overlapping paths E101–E155 and E093–E155; and (c) Site amplification in $\log_{10}$ (amplitude) units observed at E101 with respect to several surrounding stations for the M_w 5.1 Lorca earthquake, which occurred on 11 May 2011.
Figure S2. Site amplification in $\log_{10}$ (amplitude) units versus backazimuth for different frequencies observed at E101 with respect to station E093.

Two-Station Paths and the *Lg* Q_0 Model for the Iberian Peninsula Using a Reduced Source-to-Station Azimuths' Difference Constraint

The remaining two supplemental figures contain the results of the *Lg* Q_0 inversion in the Iberian Peninsula for a reduced constraint of the source-to-station azimuths' difference from the initial 15° value to 8°.

Figure S3. Two-station paths used to estimate *Lg* attenuation for a $(\delta\theta)_{max}$ value of ±8°.

Figure S4. Lateral variation of *Lg* Q_0 in the Iberian Peninsula for a $(\delta\theta)_{max}$ value of ±8°.

B. Noriega, R., A. Ugalde, A. Villaseñor, and M. Harnafi (2015). Frequecny-dependent *Lg*-wave attenuation in northern Morocco, *Tectonophysics.*, **663**, 250-260.

Tectonophysics 663 (2015) 250–260

Contents lists available at ScienceDirect

Tectonophysics

journal homepage: www.elsevier.com/locate/tecto

Frequency-dependent *Lg*-wave attenuation in northern Morocco

Raquel Noriega [a,*], Arantza Ugalde [a,1], Antonio Villaseñor [a,1], Mimoun Harnafi [b]

[a] Institute of Earth Sciences Jaume Almera, CSIC, Lluís Solé i Sabarís, s/n, 08028 Barcelona, Spain
[b] Institut Scientifique, Université Mohammed V-Agdal, Rabat, Morocco

ARTICLE INFO

Article history:
Received 23 December 2014
Received in revised form 20 July 2015
Accepted 11 August 2015
Available online 20 August 2015

Keywords:
Lg attenuation
Coda normalization method
Northern Morocco
Crustal structure
Quality factor

ABSTRACT

Frequency-dependent attenuation (Q^{-1}) in the crust of northern Morocco is estimated from *Lg*-wave spectral amplitude measurements every quarter octave in the frequency band 0.8 to 8 Hz. This study takes advantage of the improved broadband data coverage in the region provided by the deployment of the IberArray seismic network. Earthquake data consist of 71 crustal events with magnitudes $4 \le m_b \le 5.5$ recorded on 110 permanent and temporary seismic stations between January 2008 and December 2013 with hypocentral distances between 100 and 900 km. 1274 high-quality *Lg* waveforms provide dense path coverage of northern Morocco, crossing a region with a complex structure and heterogeneous tectonic setting as a result of continuous interactions between the African and Eurasian plates. We use two different methods: the coda normalization (CN) analysis, that allows removal of the source and site effects from the *Lg* spectra, and the spectral amplitude decay (SAD) method, that simultaneously inverts for source, site, and path attenuation terms. The CN and SAD methods return similar results, indicating that the *Lg Q* models are robust to differences in the methodologies. Larger errors and no significant frequency dependence are observed for frequencies lower than 1.5 Hz. For distances up to 400 km and the frequency band $1.5 \le f$ (Hz) ≤ 4.5, the model functions $Q(f) = (529^{+23}_{22})(f/1.5)^{0.23 \pm 0.06}$ and $Q(f) = (457^{+7}_{-7})(f/1.5)^{0.44 \pm 0.02}$ are obtained using the CN and SAD methods, respectively. A change in the frequency dependence is observed above 4.5 Hz for both methods which may be related to the influence of the *Sn* energy on the *Lg* window. The frequency-dependent Q^{-1} estimates represent an average attenuation beneath a broad region including the Rif and Tell mountains, the Moroccan and Algerian mesetas, the Atlas Mountains and the Sahara Platform structural domains, and correlate well with areas of moderate seismicity where intermediate *Q* values have been obtained.

1. Introduction

Located in the boundary between the African and Eurasian plates, Morocco is in a region where moderate earthquakes generally occur. Due to the shallow character of its seismicity, the region has experienced destructive, but infrequent, earthquakes since historical times (e.g., Mourabit et al., 2014) that have caused thousands of casualties and extensive damage. Some devastating seismic events in Morocco were the Agadir earthquake of February 29, 1960 (M_w 5.7) and the February 24, 2004 Al Hoceima earthquake (M_w 6.4). The observed ground motions form the basis for seismic hazard analysis, which requires the estimation of attenuation relationships that are important to the overall quality of the assessment (e.g., Pasyanos, 2011). Quantifying seismic attenuation allows removal of propagation effects and improves source parameter studies (e.g., Mayeda et al., 1992). *Lg* waves have been used extensively for the determination of earthquake–source parameters and variations of crustal attenuative properties (e.g., Nuttli, 1973; Benz et al., 1997; Xie et al., 2004; Mitchell et al., 2008; Phillips and Stead, 2008; Pasyanos et al., 2009; McNamara et al., 2012; Noriega et al., 2015). Traveling with a group velocity between 3.6 and 2.8 km/s, they appear as the most prominent seismic phases recorded at regional distances in a frequency band of 0.2 to 10 Hz. They are generated either as a superposition of higher modes or as multiple reflected crustal-guided *S*-waves (Kennett, 1986). *Lg* amplitudes are very sensitive to crustal thickness variations and discontinuities within the crust (Oliver and Ewing, 1957; Kennett, 1986; Mitchell, 1995) and their measurements provide a good estimation of path-averaged crustal properties. *Lg* phases lose energy quickly in the thin waveguide of the oceanic crust (Zhang and Lay, 1995) and are also strongly attenuated across thick sedimentary basins due to the intrinsic absorption effect. Sharp variations in crustal thickness, scattering along tectonic faults and fractures, and variations of the crustal properties such as partial melting, temperature or fluid content are some factors that affect the *Lg*-wave propagation (e.g., Xie et al., 2004). *Lg*-wave attenuation is also sensitive to varying tectonic environments, being higher in regions of concentrated seismic activity, volcanically active areas and recently deformed crust, than in stable regions (Kennett, 1986; Mitchell, 1995; McNamara and Walter, 2001; Fan and Lay, 2002). These observations may be explained by the effect of scattering attenuation due to the presence of tectonic

* Corresponding author. Tel.: +34 93 4095410; fax: +34 93 4110012.
E-mail addresses: rnoriega@ictja.csic.es (R. Noriega), augalde@ictja.csic.es (A. Ugalde), antonio@ictja.csic.es (A. Villaseñor), harnafi@israbat.ac.ma (M. Harnafi).
[1] Tel.: +34 93 4095410; fax: +34 93 4110012.

http://dx.doi.org/10.1016/j.tecto.2015.08.010
0040-1951/

complexity and small-scale structural heterogeneities in tectonically active regions.

This paper is a new contribution to seismological research in Morocco, by the estimation of the average frequency-dependent attenuation characteristics of the crust using *Lg* waves. To our knowledge, the only attenuation studies in Morocco were carried out by Xie and Mitchell (1990) at a continental scale and by Boulanouar et al. (2013) in the epicentral area of the Al Hoceima earthquake using seismic coda. In this work, we took advantage of the improved broadband data coverage in northern Morocco provided by the deployment of the IberArray seismic network within the framework of the Topo-Iberia Project (e.g., Díaz et al., 2009, 2010). The results are discussed in terms of the tectonic context within they were obtained. A comparison with the attenuation parameters estimated in other regions of the world is finally performed.

2. Geotectonic setting

The western Maghreb region that includes northern Morocco and western Algeria in northwest Africa, displays a complex and heterogeneous tectonic history that is largely related to the convergence between the African and Eurasian plates. The main structural domains of this region are the Rif and Tell mountains surrounding the Alboran Sea, the Moroccan and Algerian mesetas, the Atlas Mountains and the Sahara Platform (Fig. 1). The Rif and Tell mountains, together with the Betic Range, constitute the westernmost end of the Alpine orogenic belt (Morley, 1987). Various geophysical studies suggest a maximum crustal thickness of 36 km under the Rif Mountains, decreasing to 30 km toward the coast (Torné et al., 2000; Fullea et al., 2007). The Moroccan Meseta is separated from the Rif Moutains by the Rharb foreland basin, where the Neogene and Quaternary sediments reach a maximum depth of 8 km toward the west. The Moroccan and Algerian mesetas, formed by Paleozoic rocks, are stable regions with average crustal thickness between 30 and 35 km (Mancilla et al., 2012) that were formed during the Hercynian orogeny. The Atlas Mountains, formed by Paleozoic, Mesozoic, and Tertiary rocks, are an intracontinental orogenic domain located in the foreland of the Rif and Tell mountains. They are composed of the High Atlas and Middle Atlas ranges in Morocco and the Saharan Atlas in Algeria. In contrast to the general WSW–ENE

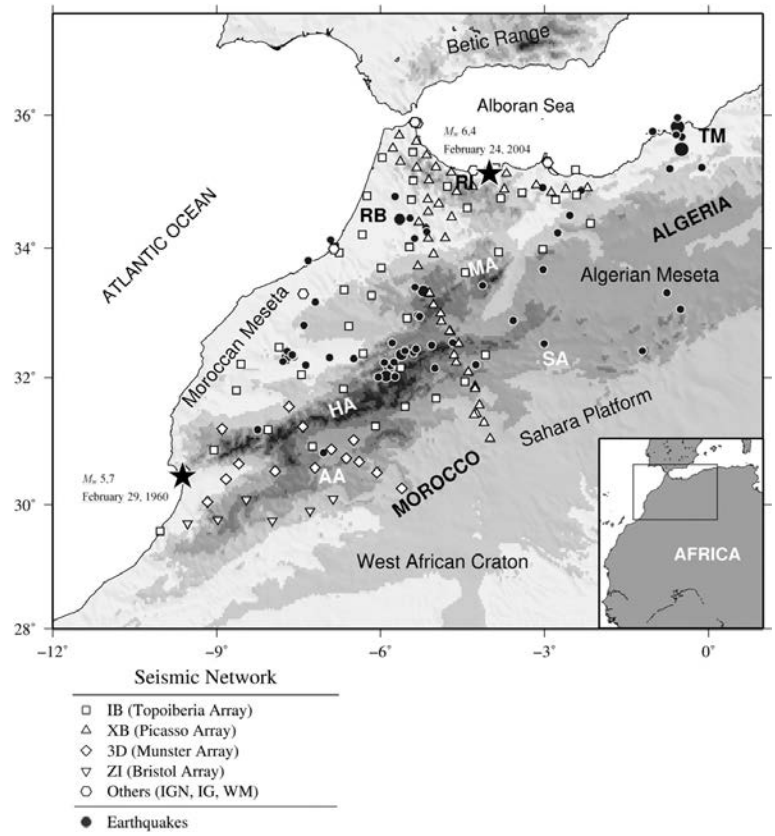

Fig. 1. Topographic map of north-western Maghreb and location of the seismic stations and earthquakes used in this study. Each network affiliation is plotted with different station symbols and earthquakes are represented by black dots. Geographic locations of the M_w 5.7 Agadir and the M_w 6.4 Al Hoceima earthquakes are plotted with stars. AA: Anti Atlas; HA: High Atlas; MA: Middle Atlas; RB: Rharb Basin; RI: Rif Mountains; SA: Saharan Atlas; TM: Tell Mountains.

strike of the High Atlas and Saharan Atlas, the Middle Atlas Range is oriented NE–SW. Although elevations in the High Atlas reach over 4000 m, crustal thickness as revealed by available seismic data is moderate (38–39 km), which does not support crustal isostatic compensation (e.g., Fullea et al., 2007). Asthenosphere upwelling may be contributing to the uplift of the Atlas in this region (Seber et al., 1996). The Atlas Mountains are flanked by comparatively less deformed areas: the Moroccan Meseta located northwest of the High Atlas, the Sahara Platform to the southeast and the Algerian Meseta, located to the northeast. To the southwest of the High Atlas it lays the Anti-Atlas mountain range, formed by a Precambrian basement and a Paleozoic cover. This NE–SW trending foreland fold belt is adjacent to the northern margin of the stable West African Craton.

Tectonic deformation in western Maghreb is related to the oblique NW–SE convergence between the African and Eurasian plates with the Rif and Atlas domains absorbing the shortening. Seismic activity is characterized by mostly shallow ($h < 30$ km), low to moderate magnitude earthquakes which are mainly located in the Rif Mountains in northernmost Morocco and the Tell Atlas mountains in north-western Algeria, decreasing southward. In the Atlas region seismicity is diffuse and is mostly localized over the Middle Atlas and the Central High Atlas (Benouar, 1994; Peláez et al., 2007). In the Sahara region, no seismic activity is observed.

3. Data

We analyzed waveform data from 110 broadband seismic stations operated by different institutions. Most seismic stations belong to the temporary portable networks deployed by the Topo-Iberia (IberArray, code IB) and Picasso (code XB) projects, the University of Münster (code 3D), and Bristol University (code ZI). In addition, we used data from permanent stations that belong to the Instituto Geográfico Nacional (IGN, Spain, code ES), Instituto Andaluz de Geofísica (IAG, Spain, code IG) and the Western Mediterranean Seismic Network (code WM).

Using the Spanish Seismic Catalogue (IGN), we selected all the crustal events ($h < 30$ km) with magnitudes $m_b \geq 4$ that occurred within a box defined by longitudes −12° to 0° and latitudes 27° to 36° between January 2008 and December 2013. The vertical component waveforms and associated instrument responses of a total of 92 earthquakes with magnitudes $4 \leq m_b \leq 5.5$ and epicentral distances from 100 to 1000 km were requested. Then, all seismograms were visually inspected restricting the final dataset to 71 events and 1274 well recorded *Lg* waveforms. The geographical locations of the seismic stations and earthquakes used are plotted in Fig. 1. A record section of an event used is plotted in Fig. 2. The *Lg* phases have been defined in this study by the group velocity window of 3.6 to 3.0 km/s.

4. Methods

The inverse quality factor Q^{-1} characterizes seismic wave attenuation (defined as the fraction of energy loss during a wave cycle). The frequency dependence of the quality factor can be modeled according to a power law of the form

$$Q(f) = Q_0(f/f_0)^{\eta}, \tag{1}$$

where Q_0 is Q at the reference frequency f_0 and η is the frequency dependence exponent, which is assumed constant over the frequencies of interest.

Several studies have noticed great variations of the *Lg Q* estimations in the same region using different methodologies (e.g., Ford et al., 2008). In this study, we apply two different methods to estimate the frequency dependence of *Lg Q* in northern Morocco. One implements the coda normalization method in the time domain (Aki, 1980; Frankel et al., 1990); and the second is based on the *Lg* spectral amplitude decay (Benz et al., 1997; McNamara et al., 2014). Comparison of the *Lg Q* estimates for different frequencies using both methodologies will give insight to the confidence of the models used (Ford et al., 2010) and will contribute

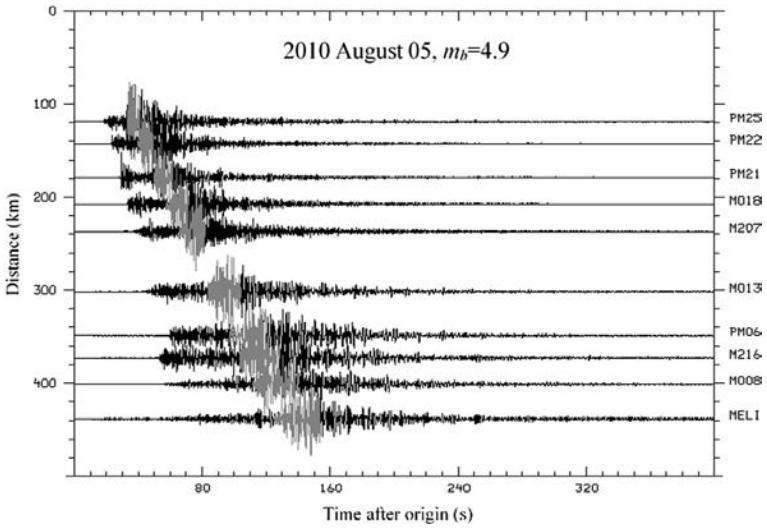

Fig. 2. Record section of the 5 August 2010, $m_b = 4.9$ event, at 10 stations of IB, PM, and WM networks. The waveforms are filtered between 0.5 and 5 Hz. *Lg* phases windowed from 3.6 to 3.0 km/s are enhanced in gray.

to the purpose of obtaining reliable measurements of frequency-dependent *Lg*-wave attenuation in Morocco.

The *Lg* spectral amplitude $A_{Lg}(r, f)$ observed at a given hypocentral distance r and frequency f can be modeled as

$$A_{Lg}(r, f) = R_{\theta,\phi} S(f) I(f) G(f) r^{-\gamma} e^{-\pi f r / Q\beta}, \quad (2)$$

where $R_{\theta,\phi}$ is the radiation pattern, $S(f)$ is the source spectra, $I(f)$ is the instrument gain, $G(f)$ is the site amplification, γ is the geometrical spreading factor, $Q(f)$ is the *Lg* quality factor and β is the average *Lg* group velocity. Here Q is an apparent path attenuation. Both intrinsic and scattering attenuations are folded into the loss parameter Q^{-1}.

4.1. Coda normalization (CN)

From Eq. (2), the *Lg* coda spectral amplitude $A^c_{Lg}(f, t_c)$ at a given lapse time t_c after the earthquake origin time can be written as

$$A^c_{Lg}(f, t_c) = S(f) I(f)\, G(f) C(f, t_c), \quad (3)$$

where $C(f, t_c)$ represents the coda envelope shape that describes how the coda spectral amplitude decays with lapse time. Selecting a t_c greater than about twice the *Lg*-wave travel time, it has been observed that the coda envelopes have a common shape that is independent of the source–receiver distance (Aki, 1969; Aki and Chouet, 1975; Frankel et al., 1990); therefore, the amplitude of the envelope varies with source and recording site amplification factors. Since the site amplification for the coda and direct waves are the same (Tsujiura, 1978), the ratio of the direct *Lg*-wave amplitude and its coda removes the site amplification factor as well as the instrument gain and the source excitation. The coda normalization method does not remove the effect of the radiation pattern, but it can be smoothed by choosing many events in a wide range of source–receiver directions (Frankel et al., 1990).

Dividing Eq. (2) by Eq. (3) and taking natural logarithms yield

$$\ln\left(\frac{A_{Lg}(f, r) r^{\gamma}}{A^c_{Lg}(f, t_c)}\right) = -\frac{\pi f}{Q\beta} r + c(f), \quad (4)$$

where $c(f)$ is a constant derived from the coda excitation factor. Eq. (4) describes a line which slope is related to Q^{-1}.

The coda normalization approach is empirical (Aki, 1980). It relies on the hypothesis that at some lapse time, the seismic energy is uniformly distributed in some volume surrounding the source. The limits of this assumption have been investigated theoretically in the framework of the multiple scattering process based on the radiative transfer theory (Sato and Fehler, 1998; Lacombe et al., 2003). Hoshiba (1994) cautioned about the use of the conventional coda normalization method for estimating the source energy of earthquakes having different focal depths in the case of strong depth dependent attenuation structure, whereas minor errors were expected in the estimation of site amplification factors. Nevertheless, the reliability of the results obtained in different studies helps to confirm the validity of the coda normalization method (Sato and Fehler, 1998).

Lg attenuation measurements using the coda normalization method have been performed by Frankel et al. (1990) in New York state, South Africa, and southern California; Akinci et al. (1995) in western Anatolia (Turkey) and southern Spain; Chung and Lee (2003) in South Korea; Ford et al. (2008) in northern California; and Jemberie (2012) in northern Ethiopian Rift and Afar.

4.2. Lg spectral amplitude decay (SAD)

According to Eq. (2), the instrument-corrected *Lg* amplitude A_{ij} at frequency f for the jth earthquake recorded at the ith station can be written as

$$\ln A_{ij}(f) + \gamma \ln r_{ij} = \ln G_i(f) + \ln S_j(f) - \frac{\pi f r_{ij}}{Q(f)\beta}, \; i = 1, \ldots, \mathrm{n}; \; j = 1, \ldots, \mathrm{m}, \quad (5)$$

where the source radiation pattern is assumed to be averaged out over multiple events and paths (Campillo et al., 1985; McNamara et al., 1996; Benz et al., 1997).

When plotting the left-hand side of Eq. (5) versus distance r, the right-hand side of Eq. (5) describes a line where the receiver (G_i) and source (S_j) terms control the intercept and the Q^{-1} term controls the slope. Therefore, a system of linear equations based on Eq. (5) can be obtained by measuring the instrument-corrected *Lg* amplitude at a single frequency for many source–receiver pairs. The system of equations can be expressed as

$$\mathbf{y} = \mathbf{A}\mathbf{x}, \quad (6)$$

where $\mathbf{y}$ is a vector composed of the left-hand side terms of Eq. (5), $\mathbf{A}$ is the coefficients' matrix made up of the right-hand side parameters of Eq. (5), and $\mathbf{x}$ is the column vector of unknowns: $G_i(f)$ ($i = 1, \ldots, \mathrm{n}$), $S_j(f)$ ($j = 1, \ldots, m$), and Q. $\mathbf{A}$ is mostly composed of ones and zeros, with the last column corresponding to the last term of Eq. (5) $-\pi f r_{ij}/\beta$. Eq. (6) can be solved using a singular value decomposition (SVD) inversion technique (Menke, 1980) to simultaneously invert for the n receiver terms, that account for site amplification; the m source factors; and a regionally averaged Q for each center frequency. The inversion is constrained by requiring that the sum of all station terms equals zero (Ottemöller et al., 2002) which implies consideration for the following additional eq. in Eq. (6):

$$\sum_{i=1}^{n} \ln G_i(f) = 0. \quad (7)$$

This single frequency Q inversion method has been applied extensively in different geotectonic regions of the world including central France (Campillo et al., 1985); the Tibetan Plateau (McNamara et al., 1996); South-Central Alaska (McNamara, 2000); the continental United States (Benz et al., 1997; Erickson et al., 2004); southern Mexico (Ottemöller et al., 2002); Colombia (Ojeda and Ottemöller, 2002); Central America (Ottemöller, 2002; McNamara et al., 2012); Britain (Sargeant and Ottemoller, 2009); Xinjiang region of China (Zhou et al., 2011); the eastern United States (McNamara et al., 2014); and the continental margin of Nova Scotia (Mousavi et al., 2014).

4.3. The geometrical spreading term

Several studies have noticed the existing trade-off between the geometrical spreading term (r^{γ}) and Q (e.g., Frankel et al., 1990; Atkinson and Mereu, 1992; Mayeda et al., 1992). In practice, most studies fix γ for specific wave propagation distances and solve for frequency-dependent Q (e.g., Ford et al., 2008; McNamara et al., 2014). Morozov (2008) proposed an alternative model with a frequency-dependent geometrical spreading and a constant, frequency-independent Q for each region. The trade-off between γ and Q could be resolved by compiling detailed information about the wave propagation medium. However, it is beyond the scope of this work and the available data to evaluate the coefficient of geometrical spreading in this region.

Numerical investigations by several authors have yielded spreading exponents of $\gamma = 0.83$ (e.g., Nuttli, 1973; Campillo et al., 1985; Shin and Herrmann, 1987) and larger values of $\gamma = 1.0$ (Yang,

2002) and $\gamma = 1.21$ (Shi et al., 1996) when using time-domain *Lg* amplitude measurements. Numerical simulations yield more stable estimates around 0.5 for the geometrical spreading exponents when measuring the *Lg* spectral amplitudes at long distance ranges (e.g., Street et al., 1975; Shin and Herrmann, 1987; Yang, 2002). The additional time domain decay is due to the increasing duration of the signal with distance and it contains both geometrical spreading and dispersion effects. In this work we measure the *Lg* spectral amplitudes across the frequency band of the data. Because, to our knowledge, there is no empirical study on the "true" value for the geometrical spreading coefficient in northern Morocco, we assume the commonly used form for the spreading rate in the frequency domain $r^{0.5}$ (e.g, Street et al., 1975; Yang, 2002). This implies that the window length is sufficient to encompass the entire dispersed wave train and that the *Lg* phase consists of higher mode surface waves which are described at long distance ranges by cylindrical spreading (Sereno et al., 1988). Therefore, the attenuation obtained is relative to the assumed spreading rate. This assumption is common and it is supported by several previous studies (e.g., Atkinson and Boore, 2014; McNamara et al., 2014).

5. Data processing and results

5.1. Coda normalization measurements

Lg amplitudes were measured in the frequency domain using earthquakes with hypocentral distances up to 400 km. First, instruments were deconvolved from each velocity seismogram to obtain ground displacement in meters. Then, $A_{Lg}(r, f)$ was calculated as the root mean square (rms) of the *Lg* window spectral amplitude, which was computed over every quarter octave between 0.9 and 7.3 Hz center frequencies. $A^c_{Lg}(f, t_c)$ was determined from the rms spectral amplitude of the coda for the reference time window centered at t_c. We used a 10 s long reference time window centered at 170 s past the origin time of the earthquake which, for an average *Lg*-wave velocity of $\beta = 3.5$ km/s, satisfies the condition $t_c > 2r/\beta$ for most of the data ($t_c > 1.5r/\beta$ for the most distant station). This value was chosen, after some tests on the final results, as a compromise between having enough data measurements and measuring the coda at long lapse times. We confirmed its validity by analyzing some examples of recorded envelopes as a function of lapse time after the earthquake origin time. Fig. 3(a) shows that the coda envelope shapes show a linear relation with m_b magnitudes for a single station that records different events at different azimuths. Moreover, the rms envelopes of bandpass-filtered seismograms at a central frequency of 3 Hz show similar coda envelope shapes for stations recording the same earthquake at different hypocentral distances and azimuths (Fig. 3(b)). Only data with amplitudes greater than twice the maximum rms spectral amplitude of a noise sample of length 10 s prior to the P_n wave onset were considered for the calculations. In the estimation of signal-to-noise ratios, we added a factor of $(1/2)\log T_s/T_n$ to the logarithm of the noise to account for the different lengths of the signal (T_s) and noise (T_n) (Taylor et al., 2002).

We solved Eq. (4) for a combination of data of different stations (e.g., Frankel et al., 1990) where the slope $Q^{-1}(f)$ was estimated by linear regression analysis. Fig. 4 plots the left-hand side of Eq. (4) against hypocentral distances together with the best fit line for three of the analyzed frequency bands. The corresponding fits for all the frequency bands analyzed are shown in Fig. S1 (available in the electronic supplement to this article). The $Q(f)$ values obtained and associated standard deviation (Table 1) represent an average for each frequency band over the region sampled by the epicenter-to-station paths plotted in Fig. 4(a). The asymmetric error bounds on *Lg* Q are derived from back transforming the formal uncertainties in the Q^{-1} estimates.

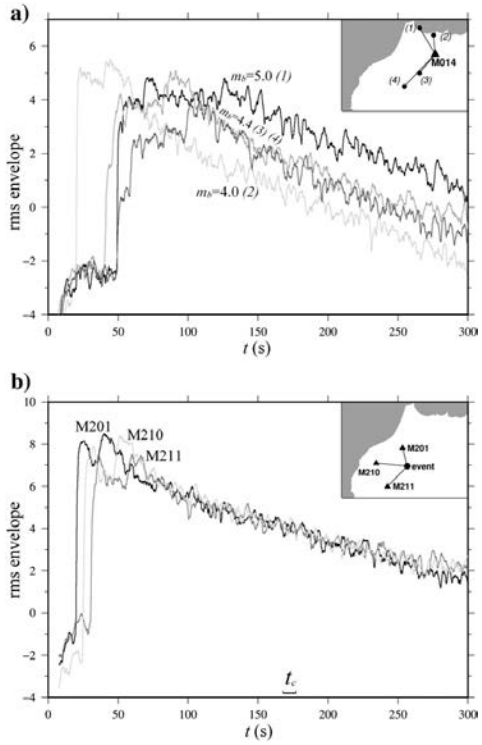

Fig. 3. Examples of root-mean-square (rms) envelopes of bandpass-filtered ($f_c = 3$ Hz) seismograms versus lapse time after the event origin time for: (a) different events recorded at the same station; and (b) different stations recording the same event. The coda reference time window t_c is indicated.

5.2. Lg spectral amplitude decay

We measured the spectral amplitude of the *Lg* waveform following the procedure described above for the coda normalization method. Then, we constructed the system of Eq. (6) and inverted using SVD for each frequency band independently. A frequency-independent average *Lg*-wave velocity of $\beta = 3.5$ km/s and a constant geometric spreading rate of $\gamma = 0.5$ were assumed.

Fig. 5 shows three examples of the original *Lg* spectral amplitudes measured at center frequencies of 1.5, 3.1, and 7.3 Hz, and the amplitudes corrected by the source and receiver terms determined from the inversion. The straight line represents the best fit for a distance range of 100–900 km. The corresponding fits for all the frequency bands analyzed are shown in Fig. S2 (available in the electronic supplement to this article). The $Q(f)$ estimations (Table 1) were obtained using the raypaths plotted in Fig. 5(a). The standard deviation of $Q(f)$ was estimated by resampling the original dataset using the delete-j jackknife technique (e.g., Erickson et al., 2004; McNamara et al., 2014) that leaves out at least $\sqrt{d}$ data points where d is the total number of observations. We randomly removed 20% of the observations from the total number of Q measures to create 1000 jackknife datasets. Then, we inverted each dataset to estimate 1000 new Q values from which we calculated the mean and standard deviation. In the results plotted in Table 1, the

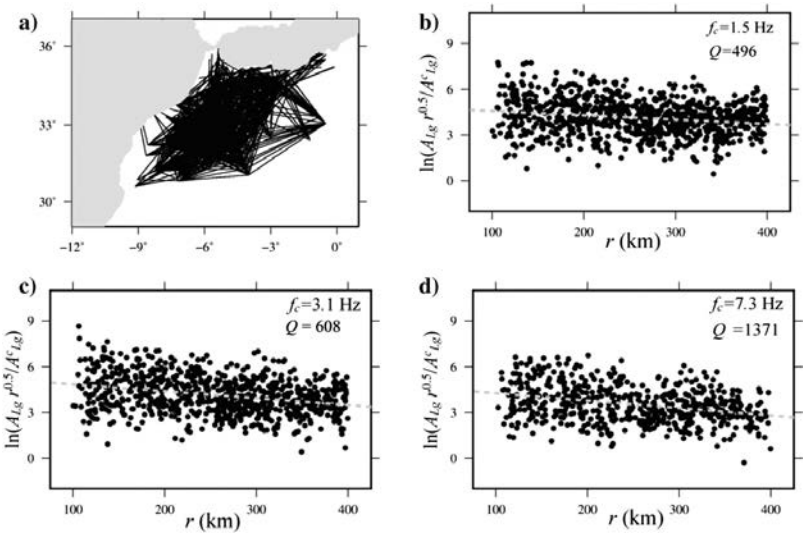

Fig. 4. (a) Epicenter-to-station paths used in the coda normalization method inversion; and *Lg*-wave to coda amplitude ratio corrected for geometrical spreading against hypocentral distance measured at center frequencies: (b) 1.5 Hz, (c) 3.1 Hz, and (d) 7.3 Hz. The *Q* values obtained are indicated.

Q estimates from the inversion at the center frequencies 1.5 and 6.2 Hz using the complete dataset were 462 and 1367, respectively. The average *Q* values after the 20% reduction in the number of data were 461 ± 26 and 1365 ± 93.

Fig. 6(a) shows some examples of the inverted site terms. A smooth variation with frequency is observed at all the sites for the frequency range 0.8–8 Hz. Little amplification is observed at stations M212 and M316. M212 is sited on the Zaër Hercynian granite of the western Moroccan Meseta and M316 is located at the western Palaeozoic Jebilet Massif (southwestern Moroccan Meseta). The site effect at M019, located at the Errachidia Cretaceous sedimentary basin, appears to be stronger (Saadi, 1975). Although the geological information on the

Table 1
Average *Lg Q* values and their standard errors at 13 center frequencies (f_c) between 0.9 and 7.5 Hz estimated using the coda normalization (CN) method for hypocentral distances less than 400 km; and the spectral amplitude decay method (SAD) using the complete data set and for distances up to 400 km. The asymmetric error bounds on *Lg Q* are derived from back transforming the formal uncertainties in the Q^{-1} estimates.

	CN		SAD (400 km)		SAD	
f_c (Hz)	Q	σ	Q	σ	Q	σ
0.9	649	+422 −183	618	+122 −87	479	+174 −107
1.1	547	+208 −118	493	+59 −48	528	+34 −30
1.3	601	+213 −124	533	+53 −45	489	+43 −37
1.5	496	+103 −73	453	+78 −58	461	+35 −30
1.8	617	+136 −94	512	+41 −35	495	+24 −22
2.2	573	+92 −70	546	+28 −26	548	+26 −24
2.6	595	+87 −67	590	+30 −27	592	+53 −45
3.1	608	+76 −61	609	+30 −27	647	+43 −38
3.7	637	+72 −59	678	+26 −24	753	+55 −48
4.4	686	+74 −61	743	+24 −22	851	+47 −43
5.2	791	+84 −69	922	+36 −33	1058	+57 −51
6.2	989	+114 −93	1091	+61 −55	1365	+70 −64
7.3	1371	+186 −146	1455	+88 −78	1767	+97 −87

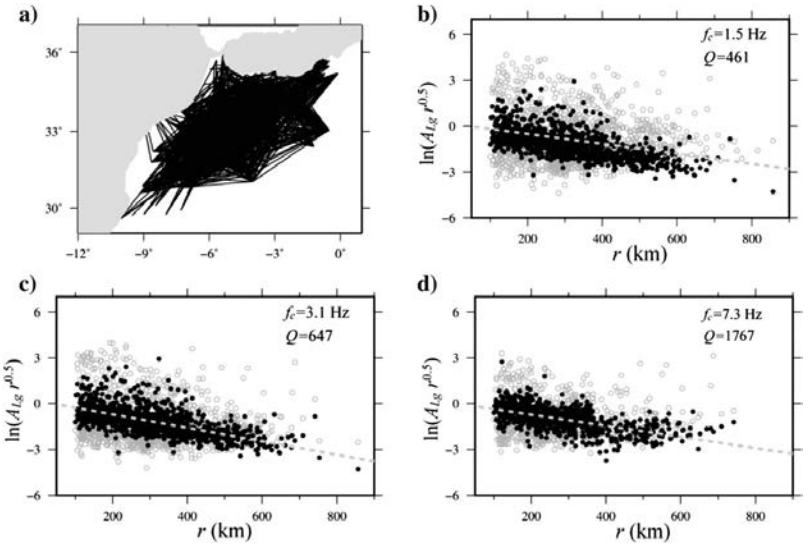

Fig. 5. (a) Epicenter-to-station paths used in the spectral amplitude decay method inversion; and observed *Lg*-wave amplitude corrected for geometrical spreading (gray dots) and corrected for source and site terms (black dots) against hypocentral distance at center frequencies: (b) 1.5 Hz, (c) 3.1 Hz, and (d) 7.3 Hz. The *Q* values obtained are indicated.

temporary stations' foundation is not known, the values seem reasonable and indicate that no serious trade-off with *Q* has occurred in the inversion process. Fig. 6(b) plots the source terms obtained from the inversion at 1.5 and 7.3 Hz center frequencies versus the earthquake magnitude. An increase of the source terms with increasing magnitudes is observed which supports that the source terms computed from the inversion are appropriate. A comparison of the *Lg Q* estimations using both the spectral amplitude decay and the coda normalization methods shown in Table 1 supports this conclusion, as it will be discussed in the next section. In this regard, results from the spectral amplitude decay method have been computed using the complete data set and for data with hypocentral distances up to 400 km, to be comparable with the coda normalization method.

6. Discussion

6.1. Frequency dependence of Lg Q

Fig. 7 plots the *Lg Q* estimates as a function of frequency for northern Morocco using the coda normalization (CN) and the spectral amplitude decay (SAD) methods. In this figure, the values shown in Table 1 were fitted to the frequency dependence function (1). The *Q* estimate at the center frequency 0.9 Hz has larger uncertainties than the other *Q* estimates and unnoticeable frequency dependence is observed up to 1.5 Hz. The relatively large errors observed at lower frequencies have been found in other works (e.g. Benz et al., 1997; Ottemöller et al., 2002; Mousavi et al., 2014) and may be associated with a stronger influence of the radiation pattern that has not been included in the formulation (Erickson et al., 2004; Singh et al., 2004). Moreover, a distinct change in the frequency dependence is observed above 4.5 Hz for both methods. The frequency-dependent functions obtained for the frequency bands 1.5 to 4.5 Hz are:

$$Q(f) = (529^{+23}_{-22})(f/1.5)^{0.23 \pm 0.06},\ 1.5 \le f \le 4.5\ \text{Hz},\ r \le 400\ \text{km (CN)}$$
$$Q(f) = (444^{+8}_{-8})(f/1.5)^{0.59 \pm 0.03},\ 1.5 \le f \le 4.5\ \text{Hz},\ r \le 900\ \text{km (SAD)}$$

$$Q(f) = (529^{+23}_{-22})(f/1.5)^{0.23 \pm 0.06},\ 1.5 \le f \le 4.5\ \text{Hz},\ r \le 400\ \text{km (SAD)}$$

whereas the functions for the frequency band 4.5 to 7.3 Hz result in:

$$Q(f) = (684^{+35}_{-33})(f/4.5)^{1.33 \pm 0.17},\ 4.5 \le f \le 7.3\ \text{Hz},\ r \le 400\ \text{km (CN)}$$
$$Q(f) = (879^{+2}_{-5})(f/4.5)^{1.41 \pm 0.03},\ 4.5 \le f \le 7.3\ \text{Hz},\ r \le 900\ \text{km (SAD)}$$
$$Q(f) = (765^{+22}_{-22})(f/4.5)^{1.26 \pm 0.10},\ 4.5 \le f \le 7.3\ \text{Hz},\ r \le 400\ \text{km (SAD)}.$$

The asymmetric error bounds on Q_0 are derived from transforming back the uncertainties obtained for ln Q_0 through the linearization of (1). Strong frequency dependence is found above 4.5 Hz, with exponents ranging from 1.26 to 1.41. A similar behavior was noticed by Benz et al. (1997) for the North American's Basin and Range Province. This is likely to represent contamination of the *Lg* window by *Sn* energy at high frequencies, as proved by Shin and Herrmann (1987). The higher frequency contents of the *Sn* phase compared to the *Lg* may introduce an upward bias in the *Lg Q* estimate (Sereno et al., 1988). Therefore, we suggest that the model constrained to the frequency bandwidth below 4.5 Hz may represent the *Q* function in northern Morocco.

6.2. Lg Q estimates using the CN and SAD methods

As observed in Table 1 and Fig. 7, the *Lg Q* values obtained for hypocentral distances up to 400 km using the CN and SAD methods are within the error bounds for the studied frequency range. This indicates that the results are robust to differences in the methods. Because the distance limit of the homogeneity assumption of the coda energy has not been fully tested (e.g. Ford et al., 2008), this result supports the extension of the coda normalization method to regional distances, at least up to 400 km in the study region. Greater *Q* values at high frequencies are obtained from SAD when larger hypocentral distances are involved in the inversion. Shin and Herrmann (1987) showed that, at large distances, the *Lg* window is influenced by the *Sn* coda at high frequencies. Fig. S2 (available in the electronic supplement to this article) also

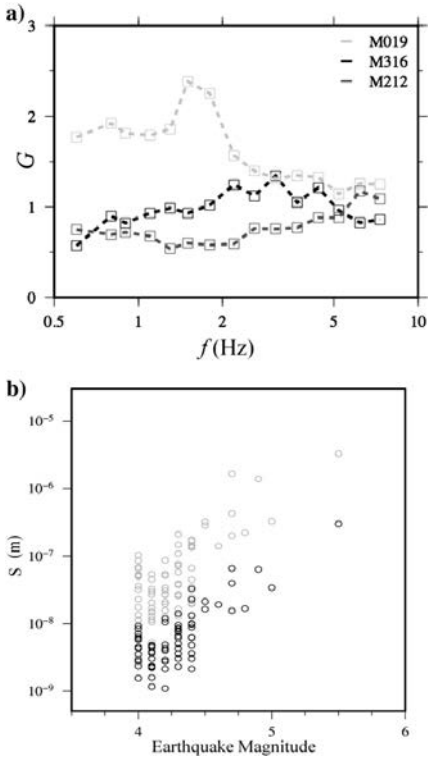

Fig. 6. (a) Site terms estimated from the *Q* inversion versus frequency for the M316, M212 and M019 seismic stations; and (b) source terms calculated from the *Q* inversion against earthquakes' magnitude at 1.5 Hz (gray dots) and 7.3 Hz (black dots).

reflects how the *Lg* spectral amplitude decay trend changes for distances greater than 400 km at high frequencies. The attenuation estimates using both methods are relative to the assumed spreading rate of $r^{0.5}$.

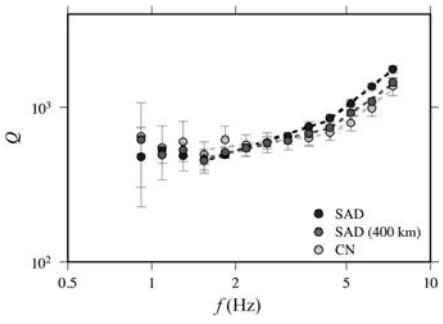

Fig. 7. Average *Lg*-wave quality factor as a function of frequency estimated from coda-normalized *Lg* spectral amplitudes for distances less than 400 km (light gray dots) and amplitude spectral decay using the complete data set (black dots) and up to 400 km distance (gray dots). The frequency-dependent *Lg Q* functions are indicated in the text.

For both methods, Fig. 7 displays a minimum *Lg Q* value around 1.5 Hz. Benz et al. (1997) and Otemöller et al. (2002) also found a minimum between 0.5 and 1 Hz in the western United States and around 1.5 Hz in southern Mexico, respectively. These results are in agreement with Aki (1980) and Sato (1990) that postulated the existence of a lithospheric attenuation peak near 1 Hz.

6.3. Comparison with other regions

Table 2 lists the *Lg Q* frequency dependence functions obtained in different regions of the world. The method applied, together with the distance range and frequencies used is also indicated. Table 2 shows that tectonically active regions are related to low *Lg Q* values (e.g., Ford et al., 2008; Ottemöller, 2002; Ottemöller et al., 2002; Ojeda and Ottemöller, 2002; Ferdinand, 1998; Benz et al., 1997; Paul et al., 1996; Akinci et al, 1995; Chávez and Priestley, 1986) whereas more stable tectonic areas are associated with high *Lg Q* (e.g., Hasegawa, 1985; Chun et al., 1987; Shi et al., 1996; Chung and Lee, 2003; Singh et al., 2004; McNamara et al., 2014; Mousavi et al., 2014). Intermediate values of *Lg Q* and frequency-dependent exponent η correlate well with areas of moderate seismicity such as Xinjiang and adjacent regions (Zhou et al., 2011), North Korea (Chun et al., 2009) and South Africa (Frankel et al., 1990). A comparison between the $Q(f)$ values obtained in this study and some models determined for other regions are shown in Fig. 8. Our estimates are between the models obtained by Erickson et al. (2004) for the central United States and Chazalon et al. (1993) for central Spain. In general, our results correlate well with those obtained in moderate to stable continental regions where intermediate to relative high Q_0 values and moderate to weak frequency dependence are observed.

The inverse methods used in this work utilize many source–receiver paths and solve for an average regional *Lg Q* estimate. However, the dispersion of the measurements that can be observed in Figs. 4 and 5 could be associated with lateral variations of *Lg* attenuation. Early works of *Lg* coda *Q* performed in continental Africa (Xie and Mitchell, 1990; Mitchell, 1995) showed relatively low Q_0 values in the Atlas Mountains and higher values associated with surrounding stable areas such as the West African Craton and the East Saharan Craton. In this work, the scarce seismicity in some areas and the location of the temporary stations, that were shifted during successive stages, did not allow us to consider regionalized sets of paths or to apply source–path corrected methods such as the two station and the reverse two station methods (Chun et al., 1987; Noriega et al., 2015) for potentially correlating *Lg Q* with regional structures across northern Morocco. Future work will consider less restrictive tomographic methods to be able to image the lateral variations of *Lg* attenuation in northern Morocco.

7. Conclusions

The frequency dependence of *Lg Q* was estimated for the first time in northern Morocco. It was possible due to the improved broadband data coverage provided by the deployment of the IberArray and other temporary seismic networks. The estimates using the coda normalization and spectral amplitude decay methods are within the error bounds for the frequency band 0.8–8 Hz. This result indicates that the estimates are robust to the different assumptions of the methodologies used and it supports the extension of the coda normalization method to regional distances (up to 400 km) in this region. Relatively larger errors were observed at the lower analyzed center frequencies that may be associated with a stronger influence of the radiation pattern that has not been included in the formulations. Strong frequency dependence was observed above 4.5 Hz, which may be caused by the influence of *Sn* energy on the *Lg* window. We conclude that the $Q(f)$ function in the frequency band 1.5 to 4.5 Hz may be used to model the frequency dependent *Lg* attenuation in northern Morocco. Results reflect intermediate *Lg* Q_0 values at 1.5 Hz which are typically observed in regions with moderate seismic activity and they represent an average apparent attenuation, having

Table 2
Frequency dependence *Lg*-wave attenuation functions obtained in different tectonic regions of the world. The frequency band, epicentral distance range, and method used are indicated (CN: coda normalization; SAD: spectral amplitude decay; TAD: temporal amplitude decay; TS: two-station; RTS: reverse two-station).

f (Hz)	r (km)	Q_o	η	Method	Region
0.9–10.75	100–1200	615 ± 25	0.35 ± 0.04	SAD	Continental margin of Nova Scotia (Mousavi et al., 2014)
0.5–24	250–1100	751 ± 39	0.28 ± 0.05	SAD	Eastern United States (McNamara et al., 2014)
0.5–16	250–700	245 ± 31	0.61 ± 0.08	SAD	Hispaniola región (McNamara et al., 2012)
0.5–5	>200	372	0.69	SAD	Xinjiang and its adjacent regions (Zhou et al., 2011)
1–4	>1200	345 ± 3	0.381 ± 0.006	RTS	North Korea (Chun et al., 2009)
1–10	170–600	266	0.53	SAD	Britain (Sargeant and Ottemoller, 2009)
0.5–8	100–400	112 ± 7	0.55 ± 0.06	CN	Northern California (Ford et al., 2008)
0.5–24	110–800	152 ± 37	0.72 ± 0.16	SAD	Southern California (Erickson et al., 2004)
1–12	110–1300	470 ± 127	0.52 ± 0.16	SAD	Central United States (Erickson et al., 2004)
0.5–24	110–900	650 ± 143	0.36 ± 0.14	SAD	Northeast United States (Erickson et al., 2004)
0.5–24	110–800	200 ± 77	0.69 ± 0.16	SAD	Basin and Range Province (Erickson et al., 2004)
0.1–20	240–2400	800	0.42	SAD	Indian Shield (Singh et al., 2004)
1.5–24	155–400	556	0.54	CN	South Korea (Chung and Lee, 2003)
1.6–8	>200	204 ± 25	0.85 ± 0.09	SAD	Southern Mexico (Ottemöller et al., 2002)
0.5–5	>200	230	0.6	SAD	Colombia (Ojeda and Ottemöller, 2002)
0.5–5	>200	128 ± 15	0.84 ± 0.08	SAD	Central America (Ottemöller, 2002)
0.2–3.6	200–500	126 ± 9	0.37 ± 0.02	TS	Eastern Tibetan plateau (Xie et al., 2004)
0.5–24	100–500	220 ± 30	0.66 ± 0.09	SAD	South-Central Alaska (McNamara, 2000)
0.75–5	400–800	186 ± 7	0.78 ± 0.05	TAD	East African Rift (Ferdinand, 1998)
1–5	150–1000	235 ± 11	0.56 ± 0.04	SAD	Basin and Range Province (Benz et al., 1997)
1–7	150–700	187 ± 7	0.55 ± 0.03	SAD	Southern California (Benz et al., 1997)
1–8	150–400	138	0.76	SAD	Southern Sierra Nevada, California (Paul et al., 1996)
0.5–16	150–2000	366 ± 37	0.45 ± 0.06	SAD	Tibetan Plateau (McNamara et al., 1996)
0.5–16	41–1394	561	0.47	SAD	Appalachian Province (Shi et al., 1996)
0.5–16	41–1394	705	0.41	SAD	Northern New England (Shi et al., 1996)
0.5–16	41–1394	905	0.40	SAD	Adirondack Mountains (Shi et al., 1996)
1.5–10	80–400	82	1.0	CN	Western Anatolia (Akinci et al., 1995)
1.5–12	80–400	83	0.88	CN	Southern Spain (Akinci et al., 1995)
0.5–2.5	200–1300	560–650	0.19	CN	Eastern Kazakhtan (Sereno, 1990)
3	80–360	360	–	CN	South Africa (Frankel et al., 1990)
2–20	80–400	1600	–	CN	New York State (Frankel et al., 1990)
1–3	200–1400	580	0.18	SAD	Norway (Sereno et al., 1988)
0.6–10	90–867	1100	0.19	RTS	Eastern Canada (Chun et al., 1987)
0.3–10	200–500	214	0.54	SAD	Great Basin (Chávez and Priestley, 1986)
0.5–10	289–576	290	0.52	SAD	Central France (Campillo et al., 1985)
0.6–20	70–900	900	0.20	SAD	Canadian Shield (Hasegawa, 1985)

components of both scattering and intrinsic attenuations, beneath a broad region including the Rif and Tell mountains, the Moroccan and Algerian mesetas, the Atlas Mountains and the Sahara Platform structural domains. The frequency dependence *Lg*-wave attenuation functions obtained in this work can be useful to better quantify the earthquake hazard assessment in northern Morocco.

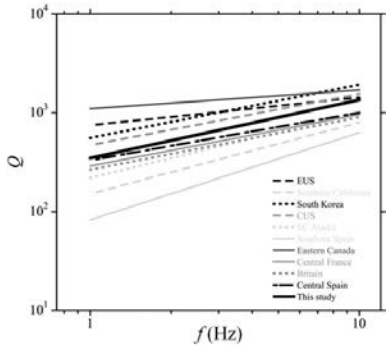

Fig. 8. Frequency dependent *Lg Q* obtained in this study compared to the results from other regions in the world: Eastern United States (EUS; McNamara et al., 2014), Britain (Sargeant and Ottemoller, 2009); Central United States (CUS; Erickson et al., 2004); Southern California (Erickson et al., 2004); South Korea (Chung and Lee, 2003); South-Central Alaska (McNamara, 2000); Southern Spain (Akinci et al., 1995); Eastern Canada (Chun et al., 1987) and Central France (Campillo et al., 1985).

Supplementary data to this article can be found online at http://dx.doi.org/10.1016/j.tecto.2015.08.010.

Acknowledgments

The authors would like to thank I. Morozov and the anonymous reviewer for their constructive comments and suggested references that improved the manuscript. Funds provided by the Spanish government through the FPI PhD grant (BES-2011-044291) are supporting R. Noriega. Funds provided by REPSOL CO-DOS project are supporting A. Ugalde. This is a contribution of the Team Consolider-Ingenio 2010 TOPO-IBERIA (CSD2006-00041).

References

Aki, K., 1969. Analysis of seismic coda of local earthquakes as scattered waves. J. Geophys. Res. 74, 615–631. http://dx.doi.org/10.1029/JB074i002p00615.
Aki, K., 1980. Attenuation of shear waves in the lithosphere for frequencies from 0.05 to 25 Hz. Phys. Earth Planet. Inter. 21, 50–60. http://dx.doi.org/10.1016/0031-9201(80)90019-9.
Aki, K., Chouet, B., 1975. Origin of coda waves: source, attenuation, and scattering effects. J. Geophys. Res. 80, 3322–3342. http://dx.doi.org/10.1029/JB080i023p03322.
Akinci, A., Del Pezzo, E., Ibáñez, J., 1995. Separation of scattering and intrinsic attenuation in southern Spain and western Anatolia (Turkey). Geophys. J. Int. 121, 337–353. http://dx.doi.org/10.1111/j.1365-246X.1995.tb05715.x.
Atkinson, G.M., Boore, D.M., 2014. The attenuation of Fourier amplitudes for rock sites in eastern North America. Bull. Seismol. Soc. Am. 104, 513–528. http://dx.doi.org/10.1785/0120130136.
Atkinson, G.M., Mereu, R.F., 1992. The shape of ground motion attenuation curves in southeastern Canada. Bull. Seismol. Soc. Am. 82, 2014–2031.
Benouar, D., 1994. An earthquake catalogue for the Maghreb region 20° − 38°N, 10° − 12°E for the period 1900–1990. Ann. Geophys. 37, 511–528.
Benz, H., Frankel, A., Moore, D., 1997. Regional *Lg* attenuation for the continental United States. Bull. Seismol. Soc. Am. 87, 606–619.

Boulanouar, A., El Moudnib, L., Harnafi, M., Cherkaui, T.E., Rahmouni, A., Baukalouch, M., Sebbani, J., 2013. Spatial variation of coda wave attenuation using aftershocks of the Al Hoceima earthquake of 24 February, 2004, Morocco. Nat. Sci. 5, 72–77. http://dx.doi.org/10.4236/ns.2013.58A1009.
Campillo, M., Plantet, J.L., Bouchon, M., 1985. Frequency-dependent attenuation in the crust beneath central France from *Lg* waves: data analysis and numerical modeling. Bull. Seismol. Soc. Am. 75, 1395–1411.
Chávez, D.E., Priestley, K.F., 1986. Measurement of frequency dependent *Lg* attenuation in the Great Basin. Geophys. Res. Lett. 13, 551–554.
Chazalon, A., Campillo, M., Gibson, R., Carreno, E., 1993. Crustal wave propagation anomaly across the Pyrenean Range: Comparison between observations and numerical simulations. Geophys. J. Int. 115, 829–838. http://dx.doi.org/10.1111/j.1365-246X.1993.tb01495.x.
Chun, K.Y., West, G.F., Kokoski, R.J., Samson, C., 1987. A novel technique for measuring *Lg* attenuation results from eastern Canada between 1 to 10 Hz. Bull. Seismol. Soc. Am. 77, 398–419.
Chun, K.Y., Wu, Y., Henderson, G.A., 2009. *Lg* attenuation near the North Korean border with China, part I: model development from regional earthquake sources. Bull. Seismol. Soc. Am. 99, 3021–3029. http://dx.doi.org/10.1785/0120080316.
Chung, T.W., Lee, K., 2003. A study of high-frequency Q_{Lg}^{-1} in the crust of South Korea. Bull. Seismol. Soc. Am. 93, 1401–1406. http://dx.doi.org/10.1785/0120020199.
Díaz, J., Villaseñor, A., Gallart, J., Morales, J., Pazos, A., Córdoba, D., Pulgar, J., García-Lobón, J.L., Harnafi, M., Topolberia Seismic Working Group, 2009. Orfeus Newsletter 8, 2.
Díaz, J.A., Villaseñor, J., Morales, A., Pazos, D., Córdoba, J., Pulgar, J.L., García-Lobón, M., Harnafi, R., Carbonell, J., Gallart, Seismic Working Group, Topolberia, 2010. Background noise characteristics at the IberArray broadband seismic network. Bull. Seismol. Soc. Am. 100, 618–628. http://dx.doi.org/10.1785/0120090085.
Erickson, D., McNamara, D.E., Benz, H.M., 2004. Frequency-dependent *Lg Q* within the continental United States. Bull. Seismol. Soc. Am. 94, 1630–1643. http://dx.doi.org/10.1785/012003218.
Fan, G., Lay, T., 2002. Characteristics of Lg attenuation in the Tibetan Plateau. J. Geophys. Res. 107 (B10), 2256. http://dx.doi.org/10.1029/2001JB000804.
Ferdinand, R.W., 1998. Average attenuation of 07–50 Hz *Lg* waves and magnitude scale determination for the region bounding the western branch of the East African Rift. Geophys. J. Int. 134, 818–830. http://dx.doi.org/10.1046/j.1365-246x.1998.00616.x.
Ford, S.R., Dreger, D.S., Mayeda, K., Walter, W.R., Malagnini, L., Phillips, W.S., 2008. Regional attenuation in northern California: a comparison of five 1D *Q* methods. Bull. Seismol. Soc. Am. 98, 2033–2046. http://dx.doi.org/10.1785/0120070218.
Ford, S.R., Phillips, W.S., Walter, W.R., Pasyanos, M.E., Mayeda, K., Dreger, D.S., 2010. Attenuation tomography of the Yellow Sea/Korean Peninsula from coda-source normalized and direct *Lg* amplitudes. Pure Appl. Geophys. 167, 1163–1170. http://dx.doi.org/10.1007/s00024-009-0023-2.
Frankel, A., McGarr, A., Bicknell, J., Mori, J., Seeber, L., Cranswick, E., 1990. Attenuation of high-frequency shear waves in the crust: measurements from New York state, South Africa, and southern California. J. Geophys. Res. 95, 17441–17457. http://dx.doi.org/10.1029/JB095iB11p17441.
Fullea, J., Fernàndez, M., Zeyen, H., Vergés, J., 2007. A rapid method to map the crustal and lithospheric thickness using elevation, geoid anomaly and thermal analysis. Application to the Gibraltar ArcSystem, Atlas Mountains and adjacent zones. Tectonophysics 430, 97–117. http://dx.doi.org/10.1016/j.tecto.2006.11.003.
Hasegawa, H., 1985. Attenuation of *Lg* waves in the Canadian Shield. Bull. Seismol. Soc. Am. 75, 1569–1582.
Hoshiba, M., 1994. Simulation of coda wave envelope in depth dependent scattering and absorption structure. Geophys. Res. Lett. 21, 2853–2856. http://dx.doi.org/10.1029/94GL02718.
Jemberie, L.A., 2012. *Q* from 1-Hz *Lg* wave and its coda in the northern main Ethipian Rift and Afar. Bull. Seismol. Soc. Am. 102, 267–283. http://dx.doi.org/10.1785/0120110120.
Kennett, B.L.N., 1986. *Lg* waves and structural boundaries. Bull. Seismol. Soc. Am. 76, 1133–1141.
Lacombe, C., Campillo, M., Paul, A., Margerin, L., 2003. Separation of intrinsic absorption and scatteing attenution from *Lg* coda decay in central France using acoustic radiative transfer theory. Geophys. J. Int. 154, 417–425. http://dx.doi.org/10.1046/j.1365-246X.2003.01976.x.
Mancilla, F.L., Stich, D., Morales, J., Julià, J., Diaz, J., Pazos, A., Córdoba, D., Pulgar, J.A., Ibarra, P., Harnafi, M., Gonzalez-Lodeiro, F., 2012. Crustal thickness variation in northern Morocco. J. Geophys. Res. 117, B02312. http://dx.doi.org/10.1029/2011JB008608.
Mayeda, K., Koyanagi, S., Hoshiba, M., Aki, K., Zeng, Y., 1992. A comparative study of scattering, intrinsic, and coda Q^{-1} for Hawaii, Long Valley, and central California between 1.5 and 15.0 Hz. J. Geophys. Res. 97, 6643–6659. http://dx.doi.org/10.1029/92JB01406.
McNamara, D.E., 2000. Frequency dependent *Lg* attenuation in South-Central Alaska. Geophys. Res. Lett. 278, 3494–3952. http://dx.doi.org/10.1029/2000GL011732.
McNamara, D., Walter, W., 2001. Mapping crustal heterogeneity using Lg propagation efficiency throughout the Middle East, Mediterranean, southern Europe and northern Africa, Pure appl. Geophys. 158, 1165–1188.
McNamara, D.E., Owens, T.J., Walter, W.R., 1996. Propagation characteristics of *Lg* across the Tibetan Plateau. Bull. Seismol. Soc. Am. 86, 457–469.
McNamara, D., Meremonte, M., Maharrey, J.Z., Mildore, S.-L., Altidore, J.R., Anglade, D., Hough, S.E., Given, D., Benz, H.M., Gee, L., Frankel, A., 2012. Frequency-dependent seismic attenuation within the Hispaniola Island region of the Caribbean Sea. Bull. Seismol. Soc. Am. 102, 773–782. http://dx.doi.org/10.1785/0120110137.
McNamara, D., Gee, L., Benz, H.M., Chapman, M., 2014. Frequency-dependent seismic attenuation in the eastern United States as observed from the 2011 Central Virginia Earthquake and aftershock sequence. Bull. Seismol. Soc. Am. 104, 55–72. http://dx.doi.org/10.1785/01201130045.
Menke, W., 1980. Geophysical Data Analysis: Discrete Inverse Theory. Academic Press, Inc., San Diego, California.
Mitchell, B.J., 1995. Anelastic structure and evolution of the continental crust and upper mantle from seismic surface wave attenuation. Rev. Geophys. 33, 441–462. http://dx.doi.org/10.1029/95RG02074.
Mitchell, B.J., Cong, L., Elström, G., 2008. A continent-wide map of 1-Hz *Lg* coda *Q* variation across Eurasia and its relation to lithospheric evolution. J. Geophys. Res. 113, B04303. http://dx.doi.org/10.1029/2007JB005065.
Morley, K., 1987. Origin of major cross element zone: Morocco Rif. Geology 15, 761–764.
Morozov, I.B., 2008. Geometrical attenuation, frequency dependence and *Q*, and the absorption band problem. Geophys. J. Int. 175, 239–252. http://dx.doi.org/10.1111/j.1365-246X.2008.03888.x.
Mourabit, T., Abou Elenean, K.M., Ayadi, A., Benouar, D., Ben Suleman, A., Bezzeghoud, M., Cheddadi, A., Chourak, M., ElGabry, M.N., Margrin, A., Mouche, S., Meghraoui, M., Ousadou, F., Panza, G.F., Peresan, A., Romdhane, N., Vaccar, F., Zuccolo, E., 2014. Neo-deterministic seismic hazard assessment in North Africa. J. Seismol. 18, 301–318. http://dx.doi.org/10.1007/S10950-013-9375-2.
Mousavi, S.M., Cramer, C.H., Langston, C.A., 2014. Average Q_{Lg}, Q_{Sn}, and observation of *Lg* blockage in the continental margin of Nova Scotia. J. Geophys. Res. 119, 7722–7744. http://dx.doi.org/10.1002/2014JB011237.
Noriega, R., Ugalde, A., Villaseñor, A., Jurado, M.J., 2015. Spatial variation of *Lg*-wave attenuation in the Iberian Peninsula. Bull. Seismol. Soc. Am. 105. http://dx.doi.org/10.1785/0120140045.
Nuttli, O.W., 1973. Seismic waves attenuation and magnitude relations for eastern North America. J. Geophys. Res. 78, 876–885.
Ojeda, A., Ottemöller, L., 2002. Q_{Lg} tomography in Colombia. Phys. Earth Planet. Inter. 130, 253–270. http://dx.doi.org/10.1016/S0031-9201(02)00010-9.
Oliver, J., Ewing, M., 1957. Higher mode surface waves and their bearing on the structure of the Earth's mantle. Bull. Seismol. Soc. Am. 83, 1959–1970.
Ottemöller, L., 2002. *Lg* wave *Q* tomography in Central America. Geophys. J. Int. 150, 295–303. http://dx.doi.org/10.1046/j.1365-246X.2002.01715.x.
Ottemöller, L., Shapiro, N.M., Singh, S.K., Pacheco, J.F., 2002. Lateral variation of *Lg* wave propagation in southern Mexico. J. Geophys. Res. 107 (B1). http://dx.doi.org/10.1029/2001JB000206 (ESE 3-1-ESE 3-13).
Pasyanos, M.E., 2011. A case for the use of 3D attenuation model in ground-motion and seismic-hazards assessment. Bull. Seismol. Soc. Am. 101, 1965–1970. http://dx.doi.org/10.1785/0120110004.
Pasyanos, M.E., Matzel, E.M., Walter, W.R., Rodgers, A.J., 2009. Broadband *Lg* attenuation modeling in the Middle East. Geophys. J. Int. 177, 1166–1176. http://dx.doi.org/10.1111/j.1365-246X.2009.04128.x.
Paul, A., Jongmans, D., Campillo, M., Malin, P., Baumont, D., 1996. Amplitude of regional seismic phases in relation to crustal structure of the Sierra Nevada, California. J. Geophys. Res. 101, 25243–25254. http://dx.doi.org/10.1029/96JB01906.
Peláez, J.A., Chourak, M., Tadili, B.A., AïtBrahim, L., Hamdache, M., López Casado, C., Martínez Solares, J.M., 2007. A catalog of main Moroccan earthquakes from 1045 to 2005. Seismol. Res. Lett. 78, 614–621. http://dx.doi.org/10.1785/gssrl.78.6.614.
Phillips, W., Stead, R., 2008. Attenuation of *Lg* in the western US using the USArray. Geophys. Res. Lett. 35 (L07307), 1–5. http://dx.doi.org/10.1029/2007GL032926.
Saadi, M. (1975). Cartes structurales du Moroc (Provinces du Nord). 1:2 000.000. Èditions du service géologique du Maroc.
Sargeant, S., Ottemoller, L., 2009. *Lg* wave attenuation in Britain. Geophys. J. Int. 179, 1593–1606. http://dx.doi.org/10.1111/j.1365-246X.2009.04325.x.
Sato, H., 1990. Unified approach to amplitude attenuation and coda excitation in the randomly inhomogeneous lithosphere. Pure Appl. Geophys. 132, 1–29. http://dx.doi.org/10.1007/BF00874359.
Sato, H., Fehler, M., 1998. Seismic Wave Propagation and Scattering in the Heterogeneous Earth. Springer and Verlag, New York.
Seber, D., Barazangi, M., Ibenbrahin, A., Demnati, A., 1996. Geophysical evidence for lithospheric delamination beneath the Alboran Sea and the Rif–Betic mountains. Nature 379, 785–790. http://dx.doi.org/10.1038/379785a0.
Sereno, J.S., 1990. Frequency-dependent attenuation in eastern Kazakhstan and implications for seismic detection thresholds in the Soviet Union. Bull. Seismol. Soc. Am. 80 (68), 2089–2105.
Sereno Jr., T.J., Bratt, S.R., Bache, T.C., 1988. Simultaneous inversion of regional wave spectra for attenuation and seismic moment in Scandinavia. J. Geophys. Res. 83, 2019–2035. http://dx.doi.org/10.1029/JB093iB03p02019.
Shi, J., Kim, W.Y., Richards, P.G., 1996. Variability of crustal attenuation in the northeastern United States from *Lg* waves. J. Geophys. Res. 101, 25231–25242. http://dx.doi.org/10.1029/96JB02580.
Shin, T., Herrmann, R., 1987. *Lg* attenuation and source studies using 1982 Miramichi data. Bull. Seismol. Soc. Am. 77, 384–397.
Singh, S.K., Garcia, D., Pacheco, J.F., Valenzuela, R., Bansal, B.K., Dattatrayam, R.S., 2004. *Q* of the Indian shield. Bull. Seismol. Soc. Am. 94, 1564–1570. http://dx.doi.org/10.1785/012003214.
Street, R.L., Herrmann, R.B., Nuttli, O.W., 1975. Spectral characteristics of the *Lg* wave generated by central United States earthquakes. Geophys. J. R. Astron. Soc. 41, 51–63.
Taylor, S.R., Velasco, A.A., Hartse, H.E., Phillips, W.S., Walter, W.R., Rodgers, A.J., 2002. Amplitude corrections for regional seismic discriminants. Pure. App. Geophys. 159, 623–650.
Torné, M., Fernàndez, M., Comas, M.C., Soto, J.I., 2000. Lithospheric structure beneath the Alboran Basin: results from 3D gravity modelling and tectonic relevance. J. Geophys. Res. 105, 3209–3228. http://dx.doi.org/10.1029/1999JB900281.
Tsujiura, M., 1978. Spectral analysis of the coda waves from local earthquakes. Bull. Earthq. Res. Inst., Univ. Tokyo 53, 1–48.